UNIVERSIDADE DE LISBOA
FACULDADE DE CIÊNCIAS
DEPARTAMENTO DE FÍSICA

Metabolic Guided Vascular Analysis of Brain Tumors using MR/PET

Rute Belmira Martins Crespo Paula Lopes

Mestrado Integrado em Engenharia Biomédica e Biofísica

Perfil em Radiações em Diagnóstico e Terapia

Dissertação orientada por:

Prof. Dr. N. Jon Shah, Institute of Neurosciences and Medicine (INM-4), Forschungzentrum Jüllich, Jüllich, Germany

Prof. Dr. Nuno Matela, Instituto de Biofísica e Engenharia Biomédica, Departamento de Física da Universidade de Lisboa, Lisboa, Portugal

2016

Acknowledgements

First of all, my gratitude goes to Professor Jon Shah for giving me the opportunity to work at the Institute of Neurosciences and Medicine of the *Forschungszentrum Jülich* in INM-4. It was a privilege to work there. I am thankful to be part of such important research group and to experience a real research environment. The funding received from the student program for the last three months of internship was essential for this project.

As well, I would like to thank Nuno André Da Silva for giving me the opportunity to work with him on his project. I am grateful for all the advice, patience, time and energy that he focused on my work. I am thankful for the excellent example he is, his enthusiasm was contagious and very motivational for me. I will never forget this experience and his wise words "The computer is always right,"

I also would like to express my thanks to Professor Nuno Matela, who first introduced me this fascinating topic and who boosted my interest. As my supervisor, his regular and prompt feedback, support and optimism were crucial in this work. Without him, this work would never have been successful. I hope to sustain his example in my future pursuits.

I would like to thank the staff of the Institute of Neurosciences and Medicine of the *Forschungszentrum Jülich* for providing me with the conditions to learn more about neurosciences and for all their sympathy and encouragement during my stay. A special thanks to INM-4 and MR/PET physics group (Liliana Caldeira, Philipp Lohman, Ezequiel Farrher Alexandra Fion, Jörg Muller, Johannes Lindeneyer, Nini de Rossi and Elena Lordanishvili) for all your support and interesting discussions.

I would like to express my deepest gratitude to the Professors of the Institute of Biophysics and Biomedical Engineering for all the time, sympathy, encouragement and knowledge during the last five years. Once again, the funding that I received from the Erasmus Programme was essential for this project.

This work was only possible with the support of my family. Thanks Catarina, Carmo and Antònio Lopes for your moral support and encouragement, not only during this work but also throughout my academic path. Without your help, I would not have been able to, not only finish but even to start a new journey abroad.

Because going alone to a different country gives you another meaning of family, I would like to thank, all the amazing people that I meet during my ERASMUS. Thank you all, to be with me, to give me something from you and for all the amazing experiences that we lived together. In special, thank you *Spanish Mafia* and my *Portuguese Group*, we are the best nation in the world.

Finally, I would like to encourage all the students whose are thinking to go abroad, to be involved in such experiences. You should never be afraid to try, just go and do it! I can say from my experience that it is difficult to leave your home country, but after all, it is even harder to come back.

Resumo

As técnicas de imagiologia são uma mais-valia para a compreensão do corpo humano, constituindo uma ferramenta relevante para a medicina moderna. Estas técnicas permitem não só o diagnóstico, como também a monitorização de doenças, sendo especialmente importantes na área neuro-oncológica. A ressonância magnética e a tomografia por emissão de positrões (MR e PET acrónimo inglês de *Magnetic Ressonance* e *Positron Emission Tomography*, respetivamente) são referidas como as técnicas de imagem mais importantes em neuro-oncologia devido à sua capacidade e eficácia na deteção de tumores cerebrais.

Estas duas técnicas permitem obter informação relativa à localização, estado e atividade tumoral. No entanto, em ambas, a diferenciação precisa dos tecidos tumorais assim como o acesso a informação referente à heterogeneidade do tumor, através de alterações não especificas dos tecidos é limitada.

Neste momento, a análise de imagens de MR em 3 dimensões (3D) é o procedimento mais utlizado no diagnóstico de tumores cerebrais, em particular de gliomas. Desta forma, e devido ao crescente interesse na aquisição de informação adicional relativa à biologia do tumor, técnicas mais avançadas de MR, em particular imagem ponderada por perfusão (PWI, acrónimo inglês de *Perfusion-Weighted Imaging*), têm vindo a revelar-se uma mais valia para a prática clínica.

A dinâmica de contraste suscetível (DSC acrónimo inglês de *Dynamic Susceptibility Contras*t) é um dos métodos mais utilizados na medição da perfusão sanguínea em tumores cerebrais. O princípio de aquisição de DSC-MR baseia-se na injeção intravenosa de um agente de contraste paramagnético (ex. *Gadolinium-Diethylenetriamine Penta-acetic acid* (Gd-DTPA)) e na rápida medição das alterações do sinal transmitido durante a passagem do bolus através da circulação cerebral. O volume sanguíneo cerebral (CBV, acrónimo inglês de *Cerebral Blood Volume*) é um dos parâmetros mais relevantes obtidos por esta técnica. Nos tumores cerebrais, o CBV exibe uma elevada correlação com a densidade dos micro-vasos, pelo que o seu volume é tipicamente mais elevado nas regiões tumorais do que quando comparado com os tecidos saudáveis.

Para além de PWI-MR, a introdução de radio-marcadores de aminoácidos na técnica de PET tem demonstrado um bom desempenho no diagnóstico de gliomas. Esta técnica tem por base a medição da magnitude do transporte de aminoácidos e a sua distribuição no tumor.

Na região tumoral, a sua incorporação é aumentada quando comparada com o tecido normal, sendo essas diferenças traduzidas em imagem. De entre os radio-marcadores de aminoácidos disponíveis, *O(2-[^{18}F] FluoroEthyl)-L-Tyrosine* (^{18}F-FET) foi recentemente introduzido e o seu bom desempenho no diagnóstico de gliomas tem vindo a ser comprovado por diversos estudos. Desta forma, esta técnica de imagem permite não só uma delineação precisa da área tumoral como também a subsequente classificação de gliomas.

Os principais problemas que afetam o planeamento do tratamento por terapia usando radiação ou biopsia são a precisa delineação do tecido tumoral vital e a falta de informação relativa à heterogeneidade dos vasos nos tecidos tumorais. Deste modo, foi proposta a combinação da informação proveniente da técnica de ^{18}F-FET com a informação proveniente de PWI.

Diversos estudos têm sido realizados de forma a comprovar as vantagens da combinação das referidas técnicas em gliomas. Uma boa correlação foi encontrada entre CBV medido através de perfusão e diferentes radio-marcadores de aminoácidos em PET. No entanto, um estudo recente realizado com o objetivo de comparar o desempenho de ^{18}F-FET e CBV na delineação da área

tumoral em gliomas, concluiu que a informação proveniente de ^{18}F-FET permite uma delineação tumoral mais precisa. Para além disso, neste estudo foi ainda reportada uma reduzida correlação, fraca congruência espacial e diferentes localizações dos valores máximos na área do tumor entre ^{18}F-FET e CBV. Em consequência destes resultados, bem como do fraco desempenho na delineação tumoral pelos parâmetros de perfusão conhecidos, fluxo sanguíneo cerebral (CBF acrónimo inglês de *Cerebral Blood Flow*) e CBV, nesta dissertação é proposta um melhoramento na computação dos parâmetros de perfusão e a sua subsequente comparação com a informação proveniente de ^{18}F-FET. Para tal, neste trabalho foi adotada a sequência de PWI-MR desenvolvida no *Forschungszentrum Jüllich*. Esta sequência adquire múltiplos contrastes, denominado *Gradient-Echo-Spin-Echo* (GESE), explorando as vantagens da aquisição da técnica de imagem *Echo-planar Imaging with keyhole* (EPIK). Deste modo, e através da combinação de GE e SE, uma nova metodologia de PWI foi introduzida ,denominada imagiologia do tamanho dos vasos (VSI acrónimo inglês de *Vessel Size Imaging*). A técnica de VSI fornece informação acerca da vascularização tumoral, através da estimativa do caliber e densidade dos vasos, e da distribuição dos diferentes tipos de vasos (arteríolas, artérias, capilares, vénulas e veias) na área tumoral, o que não seria de outro modo acessível através dos conhecidos parâmetros de perfusão. Para além disso, sendo os tumores cerebrais caracterizados por uma anormal, desorganizada e heterogénea vascularização, alterações do calibre e densidade dos vasos assim como do volume sanguíneo, revelam ser informações importantes numa análise vascular, com particular interesse no diagnóstico de tumores, na sua monitorização e terapia.

Assim sendo, e tendo em conta a boa performance mencionada pela técnica de ^{18}F-FET na delineação da área tumoral, o principal objetivo deste trabalho é explorar a informação vascular adquirida através da técnica de VSI na região tumoral obtida pela informação proveniente de ^{18}F-FET.

Para este estudo foram recrutados vinte e cinco pacientes com gliomas. Cada paciente foi injetado com uma dose de 0.1 mmol/Kg de Gd-DTPA por peso corporal. As medições foram realizadas no *scanner* híbrido de MR/PET de 3T. As imagens de perfusão foram adquiridas usando a sequência 5-ecos GESE EPIK, simultaneamente com a aquisição das imagens de ^{18}F-FET. Depois da conversão do sinal de MR na curva de concentração versus tempo (CTC acrónimo inglês de *Concentration Time Curve*), foi realizado um ajuste da curva na primeira passagem do bolus. As regiões de interesse foram selecionadas tendo em conta áreas saudáveis e tumorais delineadas com base na informação fornecida por ^{18}F-FET. Desta forma, a área saudavél corresponde à região contra-lateral do tumor, respectivamente nos tecidos cerebrais de substância branca (WM acrónimo inglês de *White Matter*) e substância cinzenta (GM acrónimo inglês de *Gray Matter*) e a área tumoral, à região onde o rácio entre a região tumoral e a região cerebral saudável (TBR acrónimo do inglês *Tumor To Brain Ratio*), foi superior ou igual a 1.6. Para o acesso à informação vascular, os parâmetros de VSI: Índice do tamanho dos vasos (Vsi acrónimo inglês de *Vessel Size Index*), densidade média dos vasos (Q acrónimo inglês de *Mean Vessel Density*) e CBV foram analisados tanto em regiões saudáveis como tumorais. Subsequentemente, a informação de cada parâmetro foi comparada com a informação fornecida por ^{18}F-FET através do cálculo da distância entre o voxel correspondente á máxima intensidade de ^{18}F-FET e o voxel correspondente ao caliber máximo dos vasos, ao máximo volume sanguíneo e á mínima densidade dos vasos sanguíneos. Para Q foi considerado o mínimo, uma vez que ao contrário dos outros paramêtros é esperado a sua diminução na área tumoral. Por fim, e de forma a obter informação adicional relativa à heterogeneidade tumoral o parâmetro imagiologia da arquitetura dos vasos (VAI acrónimo inglês de *Vessel Architecture Imaging*) foi analisado na área tumoral delimitada por ^{18}F-FET.

A análise dos resultados relativos aos parâmetros de PW (Vsi, CBV e Q) revelou, para todos os pacientes, uma heterogénea variação no caliber e densidade dos vasos, assim como no volume cerebral na região do tumor em comparação com os tecidos cerebrais de aparência normal, WM e GM. Através da análise dos parâmetros de PW, vinte e quatro pacientes de um total de vinte e cinco apresentaram um aumento do caliber dos vasos, dezassete apresentaram um aumento do volume sanguíneo e dez uma redução da densidade dos vasos na área do tumor. Em todos os pacientes, foi verificado uma diferente localização dos parametros de PW nos vóxeis correspondestes ao valor máximo na área do tumor delineada por ^{18}F-FET. Desta forma, como a distância entre o vóxeis de maior intensidade de ^{18}F-FET e dos paramêtros de PW foi diferente de zero é possivél verificar que o voxel correspondente á máxima intensidade por ^{18}F-FET não traduz o máximo de CBV e Vsi e o mínimo de Q. Para além disso, diferentes distâncias foram encontradas para cada um dos parâmetros de PW em cada paciente. Através da combinação dos parâmetros de perfusão, diferente informação relativa á vasculatura cerebral pode ser fornecida a cada paciente e uma variação de sinal foi encontrada entre WM e GM. Ainda, da análise do parâmetro VAI foi possível distinguir os diferentes tipos de vasos (ex. artérias, capilares e veias) no tumor.

Em conclusão, a análise metabólica da vasculatura cerebral pela técnica de VSI proporciona novas perspetivas sobre a complexa natureza da vascularização e heterogeneidade tumoral. Adicionalmente, dada a diferente informação encontrada entre a captação de aminoácidos através da técnica de ^{18}F-FET e VSI, a combinação de ambas as informações pode ser bastante importante para os radiologistas, abrindo a possibilidade à obtenção de nova informação, até então disponível apenas aos patologistas e provenientes por biópsia.

Palavras-Chave: MR/PET, ^{18}F-FET, PWI, GESE, Caliber dos Vasos

Abstract

Introduction: Assessment of vascular information using the *Dynamic Susceptibility Contrast Perfusion-Weighted Imaging Magnetic Resonance* technique (DSC PWI-MR) has potential benefits in the diagnosis and treatment monitoring of brain tumors. Beyond MR techniques, amino acid *Positron Emission Tomography* (PET) tracers, particularly *O-(2-[^{18}F] FluoroEthyl)-L-Tyrosine* (^{18}F-FET), have been demonstrating a good performance in brain tumor diagnosis and treatment monitoring. Previous publications have shown a mismatch between the *Cerebral Blood Volume* (CBV) defined in PWI and metabolic information from ^{18}F-FET. PWI also allows measuring *Vessel Size Imaging* (VSI) by combining *Gradient-Echo* (GE) and *Spin-Echo* (SE) information with diffusion data. VSI enables the assessment of vessel caliber, density and architecture information, which is not directly accessible using others PWI parameters. The main goal of this work is to explore the tumor vascular information from VSI guided by the metabolic information from ^{18}F-FET.

Materials and methods: Twenty-five patients with gliomas were recruited for the study. For each patient, Gd-DTPA was injected with a dose of 0.1 mmol/Kg of body weight. The measurements were performed on a 3T MR-BrainPET scanner. PWI images were acquired using the combined 5-echo GESE echo planar imaging with keyhole (EPIK) sequence simultaneously with ^{18}F-FET PET acquisition. After the conversion of the MR signal to *Concentration Time Curve* (CTC), the first–bolus passage was fitted using a *Gamma Variate Function* (GVF). The *Regions of Interest* (ROIs), in normal and tumor areas were delineated based on ^{18}F-FET information. For the assessment of vascular information VSI parameters (e.g. *Vessel Size Index* (Vsi), *Mean Vessel Density* (Q) and *Vessel Architecture Imaging* (VAI)) and CBV were evaluated. In addition, distance between local hot spots related to ^{18}F-FET PET was also computed.

Results: For all the patients, Vsi, CBV and Q revealed a heterogeneous variation in tumor region comparing to brain tissues of normal appearance. Lower values were found in white matter (WM) comparing to grey matter (GM). From the evaluation of Vsi, CBV and Q in tumor area, twenty-four out of twenty-five patients exhibited an increased Vsi, seventeen patients an increased CBV and ten patients a decreased Q. For all the patients, the locations of the local hot spots differed considerably between ^{18}F-FET and PWI metrics. From the evaluation of VAI, different types of vessels were distinguished (arteries, veins and capillaries) in the tumor.

Conclusion: VSI metrics present different information when compared to ^{18}F-FET. The metabolic guided analysis of VSI data provides further insights into the complex nature of the tumor vascularity and heterogeneity.

Key words: MR/PET, ^{18}F-FET, PWI, GESE, Vessel caliber

Contents

List of Figures

List of Tables

List of Abbreviations

ABBREVIATION/SYMBOL	EXPLANATION
T_E	Echo -Time
T_R	Repetition Time
ΔR_{2GE*}	T_2^* Relaxation Rate
ΔR_{2SE}	T_2 Relaxation Rate
^{11}C-MET	[^{11}C]-Methyl-L-Methionine
^{18}F-FDG	[^{18}F]-Fluoro-Deoxy-Glucose
^{18}F-FET	O-(2-[^{18}F] Fluorethyl)-L-Tyrosine
ADC	Apparent-Diffusion-Coefficient
AIF	Arterial Input Function
ASL	Arterial Spin Labeling
BBB	Blood-Brain Barrier
BET	Brain Extraction Tool
CA	Contrast Agent
CBF	Cerebral Blood Flow
CBV	Cerebral Blood Volume
CT	Computed Tomography
DCE	Dynamic Contrast Enhanced
DSC	Dynamic Susceptibility Contrast
DWI	Diffusion-Weighted Imaging
EPI	Echo-Planar Imaging
EPIK	Echo-Planar Imaging with Keyhole
FAST	FMRIB's Automated Segmentation Tool
FID	Free Induction Decay
FLAIR	Fluid-Attenuation Inversion Recovery
FOV	Field of View
FSL	FMRIB Software Library
FT	Fourier Transform
GD-DTPA	Gadolinium Diethylenetriamine Pentaacetic Acid
GE	Gradient-Echo
GM	Gray-Matter
GVF	Gamma Variate Function
LOR	Line of Response
LSO	Lutetium Oxyorthosilicate
MP-RAGE	Magnetization Prepared Rapid Gradient-Echo
MR	Magnetic Resonance
MRI	Magnetic Resonance Imaging
MTT	Mean Transit Time
NMR	Nuclear Magnetic Resonance
PET	Positron Emission Tomography
PWI	Perfusion-Weighted Imaging
Q	Mean Vessel Density
RF	Radio Frequency

ROI	Region of Interest
SE	Spin-Echo
SNR	Signal to Noise Ratio
TBR	Tumor to Brain Ratio
TF	Transmitted Fraction
TTP	Time to Peak
TVOI	Tumor Volume of Interest
VAI	Vessel Architecture Imaging
VEGF	Vascular Endothelial Growth Factor
VSI	Vessel Size Imaging
WHO	World Health Organization
WM	White Matter
mVD	Mean Vessel Diameter
Vsi	Vessel Size Index

1. Context and Outline

1.1 Introduction

Medical imaging is a powerful tool used in modern medicine for disease diagnosis, for localizing tumors and screening treatment response. *Magnetic Resonance Imaging* (MRI) and *Positron Emission Tomography* (PET) have become the most important imaging techniques in modern radiology. These techniques revealed an important usage in neuro-oncology due to its capability of early tumor detection (e.g. localization, state of growth and activity) [1].

Although its ability to differentiate tumor tissue and to assess tumor heterogeneity information from nonspecific tissue changes is limited. Three-dimensional (3D) contrast-enhanced MR imaging currently remains the method of choice for glioma diagnosis. Therefore, to gain additional functional information on tumor biology (e.g. vasculature), advanced MR imaging techniques, particularly *Perfusion Weighted Imaging* (PWI), are increasingly used [2].

Currently, *Dynamic Susceptibility Contras*t (DSC) is the most common method used to measure perfusion in brain tumors [3]. DSC-MRI relies on the intravenous injection of a paramagnetic contrast agent (e.g. *Gadolinium-Diethylenetriamine Pentaacetic Acid* (Gd-DTPA)) and the rapid measurement of the transient signal changes during the passage of the bolus through the brain [4]. *Cerebral Blood Volume* (CBV) is one the most relevant parameter derived from DSC-PWI. In brain tumors, CBV shows a significant correlation with microvessel density and its volume is, typically, larger, compared to healthy brain tissues [5, 6].

Besides MRI, radiolabeled amino acids PET have been successfully used in brain tumor diagnosis. Amino acid PET measures the magnitude of amino acid transport and its distribution in the tumor. In the tumor area, the incorporation of the amino acid is increased comparing to healthy tissue and these differences can be imaged [7]. Among the available PET tracers, ^{18}F-FET exhibited a better performance in neuro-oncology, proved by an accurate tumor area delineation and glioma grading, when comparing with others available tracers and MRI techniques [8-11].

In the cases of radiation therapy or biopsy, there are some major problems that affect planning: the precise delineation of vital tumor tissue and the missed information about the heterogeneity of the vessels in tumor tissues. Hereupon, the combination of PWI and ^{18}F-FET information has been proposed for clinical practice and an accurate delineation and the assessment of complementary information about tumor localization, size, growth and perfusion can be obtained [12,13].

Several studies have been performed by combing PWI and amino acid PET information in gliomas. Despite a good correlation found between CBV and amino acid PET tracers uptake [11-13], a recent study revealed that active tumor tissue of gliomas as depicted by ^{18}F-FET information provides a better performance on tumor delineation when compared with CBV measured with PWI [13]. Also, a poor correlation, a poor spatial congruence and different hot spot localization found within both techniques supported this conclusion. Thereby, due to the lack of results from the present parameters derived from PWI (e.g. CBV), in this dissertation, it is proposed an improvement of PWI computation parameters and its comparison with ^{18}F-FET information.

For this purpose, the PWI-MR sequence developed in the *Forschungszentrum Jüllich* was adopted in this work. This sequence acquires multiple contrasts (*Gradient* and *Spin echo* (GE and SE)) taking the advantages of the *Echo-Planar Imaging with Keyhole* (EPIK) acquisition scheme [14]. By combining GE and SE a new PWI methodology emerged, the so-called *Vessel Size Imaging* (VSI) [15-23]. VSI gives information about tumor vasculature, through the evaluation

of vessels caliber and density and about the distribution of the different types of vessels (arteries, veins and capillaries), which is otherwise not directly accessible using others PW parameters. Moreover, as brain tumors are characterized by abnormal and heterogeneous poorly constructed vasculature, associated to an increased microvessel caliber and decreased density, vascular information shows to be widely important particularly in tumor diagnosis, monitoring and therapy [24].

In this manner, due to the good performance of ^{18}F-FET in tumor delineation and the vascular information provided by VSI, a metabolic guided vascular analysis can be performed. This vascular analysis could improve the major problems that impact the tumor planning being reliable important in particular for glioma monitoring.

1.2 Outline of the Thesis

The overall aim of the work discussed here was to perform a metabolic guided vascular analysis of brain tumors by combining ^{18}F-FET PET information and VSI information obtained from MR PWI using multi-echo EPIK sequence. Previous publications have shown an unsatisfactory conformity by the combination of CBV derived from PW and ^{18}F-FET information for tumor delineation. In this way, the new PW sequence was explored to compute new parameters, named VSI. Thereby, PW parameters and ^{18}F-FET information will be combined and compared in order to provide metabolic and vascular information, essential for tumor monitoring and treatment planning.

This thesis is organized in six chapters described below. The present *Chapter 1* introduces the context, motivation and general organization of the work.

Chapter 2 introduces a comprehensive explanation of the relevant theoretic underpinnings of this work. This chapter is subdivided into four sections where the MRI, PET and MR/PET modalities and the brain tumors topic are introduced. The first section, describes the MRI basic principles, followed by a description of the imaging principles, MR sequences and instrumentation. The second section describes the strategies for acquiring functional images with PET, from the positron annihilation to the post-correction images. The data acquisition, reconstruction and correction methods, as well as PET instrumentation are explained. The third section describes the multi-modal MR/ PET approach and its application in brain studies. Advantages, design difficulties and instrumentation (BrainPET system) are also described. Finally, in the last section, a brief introduction to brain tumors, particularly regarding gliomas, will be addressed with a focus on its vasculature and diagnosis issues.

Chapter 3 discusses the strategies described in the literature to provide an accurate tumor diagnosis using PWI-MR and ^{18}F-FET PET information. Tumor Vasculature using VSI methodology is explored and the main motivation of this work is addressed. Clinical and human studies for VSI methodology, gliomas studies using ^{18}F-FET PET and the combination of PWI and amino acid PET tracers will be reviewed.

In *Chapter 4*, materials and methods developed in this dissertation are described. Patients information, MRI and PET acquisitions and processing methodology will be addressed (e.g. co-registration, segmentation, masking and tumor delineation). In addition, the methodology used to fit the *Concentration Time Curve* (CTC) (Gamma fitting) will be described, as well as the features used to analyze the data.

Chapter 5 presents the results obtained in this work from the methodologies explained in *Chapter 3* and *4*.

Finally, in *Chapter 6*, a detailed discussion of the entire thesis is presented as well as the conclusion and future perspectives of this work.

2. Medical Imaging in Oncology– MR/PET Basics

In this chapter, the principal theoretical concepts required for the understanding of the main content of the remaining chapters of this dissertation are given. An overview on *Medical Imaging in Oncology* will be exploited where *Magnetic Resonance Imaging* (MRI) and *Positron Emission Tomography* (PET) will be introduced. *Hybrid Imaging* technique for application in brain studies will also be explored. Also a brief introduction about brain tumors and its inherent vasculature, particulary for gliomas, will be performed.

2.1 Introduction

Medical Imaging is a group of different imaging modalities used to obtain images from the body. In clinical practice, medical images are a key tool for diagnostic and treatment purposes. Therefore, medical imaging plays an important role in initiatives to improve public health for all population groups [1]. Nowadays, a wide number of medical imaging techniques are available such as *Computed Tomography* (CT), PET and MRI [1]. Each technique has strong and weak highlights. Since 1990, the combination of more than one image modality has been introduced, named *Hybrid Imaging.* The combination of PET with CT and MR with PET are the main hybrid imaging techniques. Both provide further and complementary information compared to their separate purchase. Using hybrid imaging, an accurate diagnosis can be obtained with a special interest in MR/PET for brain tumors diagnosis [25].

2.2 Magnetic Resonance Imaging (MRI)

Nuclear M*agnetic Resonance* (NMR) has its roots in the pioneering work of Rabi et al. [26] Bloch et al. [25] and Purcell et al. [28] in the first half of the century XX. In 1944, Rabi who the first to show the effect of radiofrequency (RF) wave with the *Larmor Frequency* on nuclear magnetic moments. For the discovery of a resonance method for recording the magnetic properties of atomic nuclei, he has received the Nobel Prize in Physics. In 1946, Bloch and Purcell devised virtually identical methods for measuring nuclear magnetic moments. While Purcell discovered the phenomenon of nuclear magnetic resonance in solids (e.g. solid paraffin) [28], Bloch discovered it in liquids (e.g. water) [27]. Since these findings, NMR has been widely used to study the magnetic properties of molecules. The step from NMR to MRI was made by inventions of Lauterbur in 1973 [29]. Both researches showed that it is possible to manipulate the local magnetic fields using gradient fields. Therefore, these findings enabled the introduction of MRI, which has since then been a very successful imaging technique.

MRI is a nuclear medical imaging technique that allows imaging *in vivo* the human morphology, structure and dynamics with a high contrast and resolution. The main characteristics of MRI are present in the diagram of figure 2.1. MRI is a 3D technique, allowing to imaging multiple body planes without changing the subject position during the acquisition [30, 31]. This technique uses magnetic fields and electromagnetic energy to generate signals from the atomic

nuclei, in particular, the hydrogen nuclei (proton of the nuclei), which can be translated into images. In this subsection, the concepts related to MRI involved in this work will be introduced.

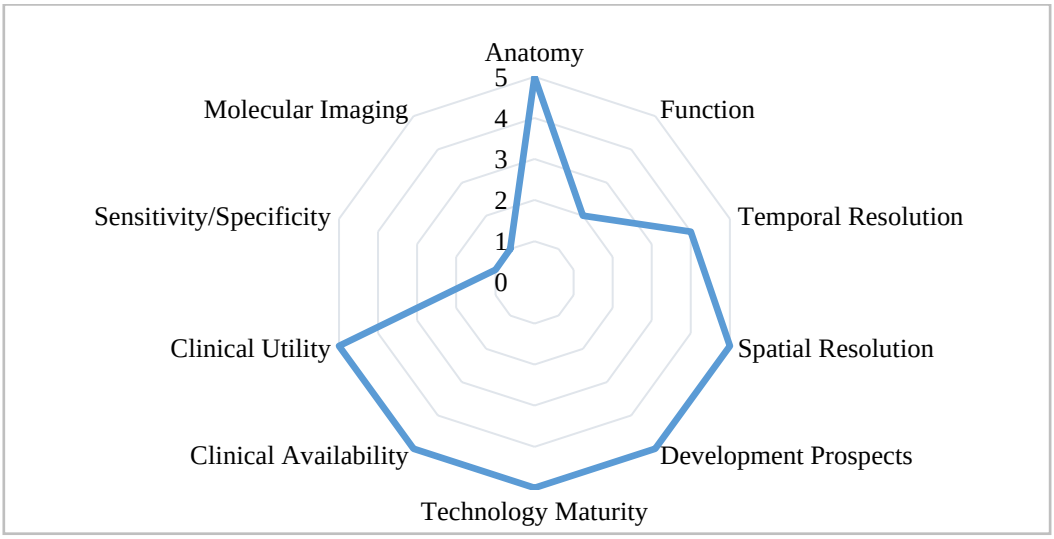

Figure 2.1: Features of MRI. Adapted from [32].

2.2.1 Basic Principles

Magnetic Resonance (MR) technique focuses on the atomic nuclei magnetic properties in order to provide anatomical images of the human body. In MR, the preferred nucleus is the hydrogen nucleus (^{1}H) because it is the most abundant in water (75%) and in the human body. Nevertheless, imaging of other nucleus such as sodium (^{23}Na) and potassium (^{19}K) is also possible [30, 31].

In the absence of an external magnetic field, the protons precess around random directions and orientations. Therefore, they compensate each other and the net value of the magnetization of the whole cohort is null. Otherwise, in the presence of an external homogenous magnetic field (B_0), the spins become quantized processing in two orientations. While one state is aligned parallel (spin-up), the other is aligned anti-parallel (spin-down) to the direction of the magnetic field. The energies of two states are given by:

$$E = \mu . B_0 = \gamma \hbar I . B_0 \quad \text{with} \quad \mu = \gamma J = \gamma \hbar I \qquad (2.1)$$

,where μ is the magnetic moment, γ the gyromagnetic ratio, J the angular momentum, $\hbar$ the Planck's constant divided by 2π, I the spin angular momentum that can be $\pm\frac{1}{2}$ for protons and B_0 the external magnetic field [33].

The spin-up (parallel) state has a slightly lower energy than the spin-down (anti-parallel) state. The energy difference between both levels is the energy needed for a proton to swap between the two states that is associated with the electromagnetic frequency required. The energy difference is given by:

$$\Delta E = \gamma \hbar . B_0 \qquad (2.2)$$

From the energy equation 2.2 the precessional frequency can be introduced, named *Larmor Frequency* (ω_0), equation 2.3.

$$\omega_0 = \gamma B_0 \qquad (2.3)$$

This frequency depends on the strength of the external magnetic field B_0 and of the gyromagnetic ratio (γ). For protons, the Larmor frequency is approximately 42.6MHz in a magnetic field of 1T.

Since the parallel state is slightly favoured, there are more protons in the spin-up than in the spin-down state. The number of protons in each state $(N_{up}|N_{down})$ follow the Boltzmann's distribution in thermal equilibrium, equation 2.4.

$$\frac{N_{up}}{N_{down}} = e^{\frac{\Delta E}{k_B T}} \approx 1 + \frac{\gamma \hbar B_0}{k_B T} \qquad (2.4)$$

, where k_B is the Boltzamann's constant and T is absolute temperature in degrees Kelvin.

The difference between the number of protons is each state $(N_{up} - N_{down})$ creates the *Net Magnetization* (M_0), equation 2.5.

$$M_0 = (N_{up} - N_{down}) . \mu = \frac{\rho \gamma^2 \hbar^2 B_0}{4 k_B T} \qquad (2.5)$$

, with the proton density ρ and $\mu = \frac{1}{2}\gamma\hbar$.

While the protons contributing to the net magnetization are all out of phase, the sum, meaning the net magnetization is exactly aligned with the magnetic field B_0 and can be measured [10].

2.2.1.1 RF Pulses

The magnetization is measured in the transverse (xy) plane where a time-varying part of the magnetization induces a signal in the receiver coils. The signal obtained in the coil is the so called *Free Induction Decay* (FID).

Even though there is a rotating component in this plane, the net magnetization is parallel to B_0 with no component in the xy plane. Therefore, the magnetization must be tipped from equilibrium into it. An alternating magnetic field B_1 having the same frequency as the Larmor frequency to be in resonance with the precessing spins must be applied to achieve this. These pulses are named *Radio-Frequency* (RF) pulses.

The spins can absorb energy and notate away from the longitudinal axis while precessing around it in the laboratory frame of reference. In a rotational frame of reference, only the nutation would be visible [33].

After the pulse is applied, the spins precess in phase and can therefore be detected. The flip-angle (α) depends only on the amplitude of B_1 and duration t_p of the RF field and can be calculated by:

$$\alpha = \gamma \int_0^{t_p} B_1(t)dt \quad (2.6)$$

2.2.1.2 Relaxation

When the RF pulse stops, the magnetization returns to equilibrium i.e. spins loss the transversal component. This process is called *Relaxation* and is induced by two independent processes. First, the dephasing of the spins (*Spin-Lattice* interaction) and second the loss of energy absorbed during the pulse (*Spin-Spin* interaction) [30].

The spin-lattice interaction results in the recovery of M_z after applying a RF pulse. This mechanism reflects the time necessary to realign the protons with B_0 by transferring protons energy to surrounding molecules. T_1 relaxation is mathematically explained by an exponential behaviour, equation 2.7. For a 90° RF pulse, T_1 relaxation is defined as the time taken for 63% of M_0 to recover after a 90°RF pulse, figure 2.2.

$$M_z(t) = M_{z_0}\left(1 - e^{\frac{-t}{T_1}}\right) \quad (2.7)$$

, where M_{z_0} is the equilibrium magnetization.

Otherwise, spin-spin interaction is the mechanism that results in a decrease of M_{xy} after applying a RF pulse. The loss of phase coherency of protons due to the changes on protons mobility causes the reduction of M_{xy}. Mathematically this process is explained by equation 2.8. For a 90° flip-angle, T_2 relaxation corresponds to the time it takes for 37% of M_{xy} to be obtained due to relaxation of transverse magnetization, figure 2.2.

$$M_{xy}(t) = M_{xy_0} e^{\frac{-t}{T_2}} \quad (2.8)$$

, where M_{xy_0} is the equilibrium magnetization

Furthermore, T_2 is also influenced by the inherent field inhomogeneities, resulting in a faster decay. In this case, the relaxation will occur at a rate of T_2*. T_2* is shorter than T_2 and is given by:

$$\frac{1}{T_2^*} = \frac{1}{T_2} + \frac{1}{T_{inhom}} = \frac{1}{T_2} + \gamma\Delta B \quad (2.9)$$

, where γ is the gyromagnetic ratio and ΔB the relaxation rate contribution attributable to field inhomogeneities across a voxel.

Since these processes take time to occur and the time taken is intrinsic to each tissue, it is possible to establish a correspondence between tissue type and the signal acquired.

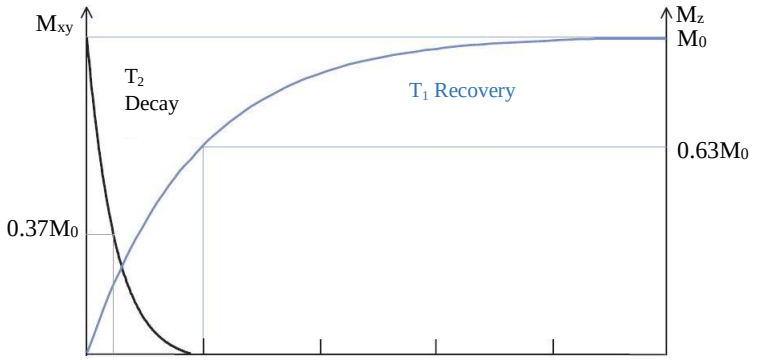

Figure 2.2: T_1 and T_2 relaxation times [33]. Although they happen at the same time, for a certain tissue T_2 is much smaller than T_1. This fact can not be visible in other tissues because the relation between both curves can be different.

2.2.2 Image Principles

2.2.2.1 Slice Selection

As it shown by equation 2.3, the resonance frequency of a spin is proportional to the field applied. In the presence of the static magnetic field, a RF pulse with the Larmor frequency will excite all spins in the imaging volume. However, it is possible to excite only a specific part of the imaging volume. Changes on the static field have to be done using a linear magnetic gradient [30]. By applying a linear magnetic gradient field in the z-direction (G_z), the amplitude of the magnetic field will vary with position (z). Consequently, the resonance frequency will also depend on the position:

$$\omega(z) = \gamma(B_0 + zG_z) \quad (2.10)$$

When a RF pulse is transmitted with a specific range of frequencies just the protons with the Larmor frequency that match the RF pulse frequency are excited, the so-called *Slice Selection*. The principle is depicted in figure 2.3. The thickness of the excited slice depends on the bandwidth ($\Delta\omega$) of the RF pulse and the steepness of the gradient, equation 2.11 [31].

$$\Delta z = \frac{\Delta\omega}{\gamma G_z} \quad (2.11)$$

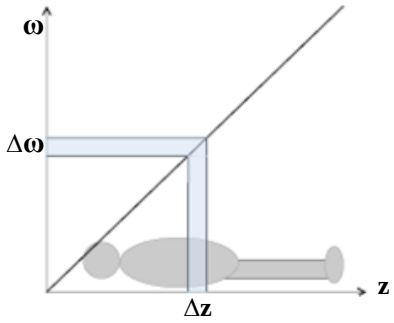

Figure 2.3: The principle of slice selection. By applying a RF pulse with a finite bandwidth (Δω), only the spins in a slice thickness (**Δz**) are excited, equation 2.11. Adapted from [34].

2.2.2.2 Frequency and Phase Encoding

Slice selection method does not differentiate between protons within each slice. Therefore, two additional gradients are usually applied in order to encode the spins in the slice. Those are named G_y and G_x depending on their direction. The first one corresponds to the *Phase Encoding Gradient* in the y direction and the second one to the *Frequency Encoding Gradient* in x direction respectively. Both gradients have identical properties but are applied in different directions and at different times. Since the three gradients (G_x,G_y, G_z) are applied, the spins can now be coded in all three directions (x, y and z).

2.2.2.3 K-Space and Image Reconstruction

In MRI, the spatial frequency domain is called *K-Space* and was introduced in 1983 by Ljunggren [35] and Twieg [36].

The 2D discrete *Fourier Transform* (FT) of the image yields a function, which describes the distribution of spatial frequencies k_x and k_y. The space of spatial frequencies is called k-space and is the inverse space of the physical co-ordinate system (x, y). The spatial frequency variables k_x and k_y are related to the time on gradient variables. Therefore, k-space data is just the MRI time domain data with a substitution of variables (t, (G_x,G_y, G_z)) to (k_x, k_y) [36].

K-space can be filled with information that codifies the image in the frequency domain. Therefore, by applying a FT on the k-space, the image reconstruction can be performed. For 2D imaging, a 2D FT is applied. For 3D images, the procedure is the same as explained for 2D but one more spatial frequency (k_z) and coordinate (z) is considered. Also, a 3D FT is applied for 3D imaging.

2.2.3 Image Sequences

A pulse sequence is simply the definition of RF and gradient pulses, where the time interval between pulses, their amplitude and the shape of the gradient affect the characteristics of the MR image. MRI pulses sequences are widely important allowing the acquisition of images with different kinds of contrast.

The *Repetition Time* (T_R) and the *Echo Time* (T_E) in milliseconds describe most sequences. T_R is the time from the application of an excitation pulse to the application of the next pulse. T_E refers to the time between the application of RF excitation pulse and the peak of the signal induced in the coil.

The two main types of MR pulse sequences used are *Spin-Echo* (SE) and *Gradient-Echo* (GE) sequences. The remaining developed MR sequences derive in some way from the combination of the SE and GE. Both sequences will be explained bellow.

2.2.3.1 Spin-Echo (SE)

In a SE sequence after the 90° RF excitation pulse, the refocusing of the spins is obtained by applying a 180º RF pulse. After the RF pulse, a G_y gradient fields are applied to spatially encode the spins and a 180º pulse is applied to rephrase the spins along with the same slice selective gradient. The signal (echo) is then acquired at T_E. A schematic overview of a SE sequence and respective sampled k-space is illustrated in figure 2.4 [33].

As shown in figure 2.4a, the 90º RF excitation pulse is applied together with a slice selection gradient. After the RF excitation, a G_y is applied along the y-axis. The amplitude of this gradient determines the coordinate k_y of the line that will be sampled in k-space (orange line), figure 2.4b. The 180º RF pulse is then applied together with the same slice selection gradient to flip the spins and make them rotate back towards coherence. The signal is acquired around T_E, while a G_x along the x-axis is switched on. This G_x scans a line in k-space in the k_x direction (blue line). Usually, G_x with the same polarity is applied during the phase-encoding gradient in order to move the k-vector towards the beginning of the line that is to be acquired (negative k_x). Furthermore, in order to acquire the others k-space lines, the process has to be repeated with a determined T_R.

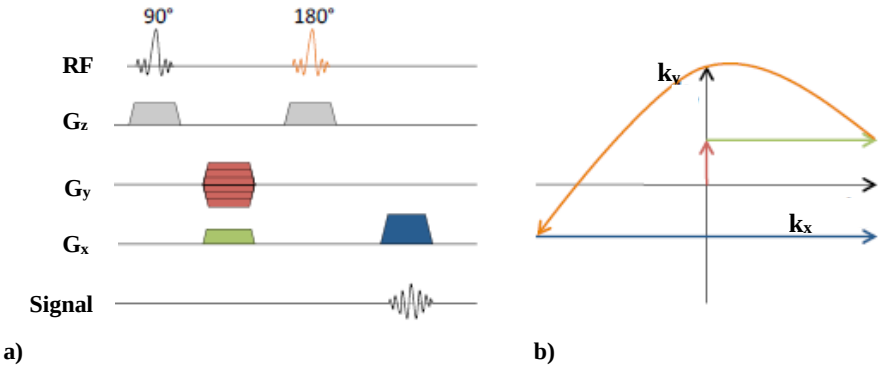

Figure 2.4: SE MR sequence. a) Schematic of a 2D SE sequence. b) K-space trajectory in the k_x and k_y plane. The data is acquired, while scanning the blue line in k-space. Adapted from [34].

2.2.3.2 Gradient- Echo (GE)

As implied by the name, in GE sequence gradients are used to diphase and rephrase the transverse magnetization vector instead of the 180º RF pulse. In GE sequence, an RF pulse is applied partially flipping the net magnetization vector into the transverse plane (flip-angle). A first gradient is applied to diphase and then a gradient with opposite sign is applied to rephase the spins [33].

GE sequence begins with the application of a RF excitation pulse simultaneously with the slice selection gradient. When the excitation pulse is turned off, the protons begin to dephase and G_y is applied along the y-axis. Simultaneously, a negative G_x is applied along the x direction in order to induce a faster dephasing of the protons. Thereafter, a positive G_y is applied to rephase the protons at the same time as the echo is measured (T_E), figure 2.5a. As well as SE sequence, the amplitude of the gradient determines the k_x and k_y coordinates of the line, which will be sampled in k-space, figure 2.5b. Here a shorter T_R can therefore be achieved when compared to a SE sequence, leading to shorter total acquisition times.

Furthermore, in GE sequence the refocusing of spins are purely based on gradients and not on a 180° pulse. Thereby, the local field inhomogeneities due to susceptibility effects are not compensated by the echo and the signal is dependent of T_2^* rather than T_2. This leads to T_2^*-weighted images instead of T_2-weighted images.

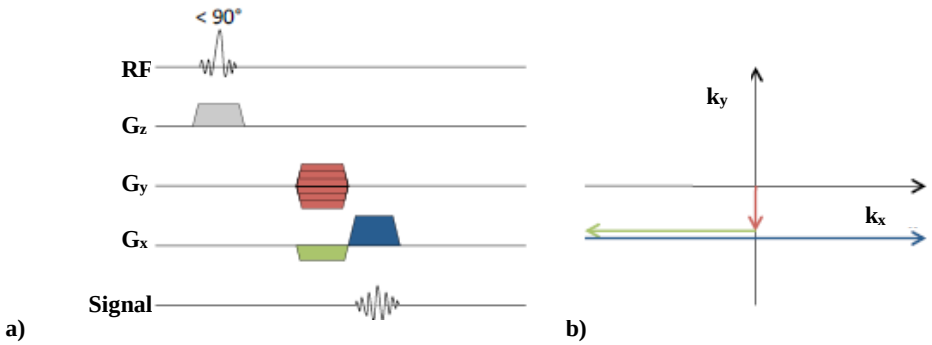

Figure 2.5: GE MR sequence. a) Schematic of a 2D GE sequence. b) K-space trajectory in the k_x and k_y plane. Adapted from [33].

2.2.3.3 Echo-planar Imaging (EPI)

Echo-planar Imaging (EPI) was introduced by Sir Peter Mansfield in 1977 who received the Nobel Prize in 2003 for his contribution to MRI and medical field [37].

EPI is a fast MRI pulse sequence that uses multiple GE with different phase steps in order to sample the k-space. In EPI, multiple lines of the k-space are acquired after a single RF excitation. The rephasing gradient reverses the spatial variation of the phase of transverse magnetization caused by a dephasing gradient. Thereby, the echoes acquisition will be accomplished by rapidly reversing the readout gradient or for a G_x along the x-axis [37].

Like a conventional SE sequence, an SE EPI sequence begins with 90°and 180° RF pulses. However, after a 180° RF pulse a short G_y gradient (blip) is applied promoting a rapid oscillation of G_x from a positive to a negative amplitude along the x-axis, forming a train of gradient-echoes. Each echo is phase encoded differently by phase-encoding blips on the phase-encoding axis. Further, each G_x oscillation corresponds to one line of imaging data in k-space and each blip results on a transition from one line to the next. In GE EPI sequences, the image is acquired after a single RF excitation pulse and uses the gradient to generate the echoes following the same process explained before. A schematic representation of a 2D SE and GE EPI sequence is illustrated in figure 2.6.

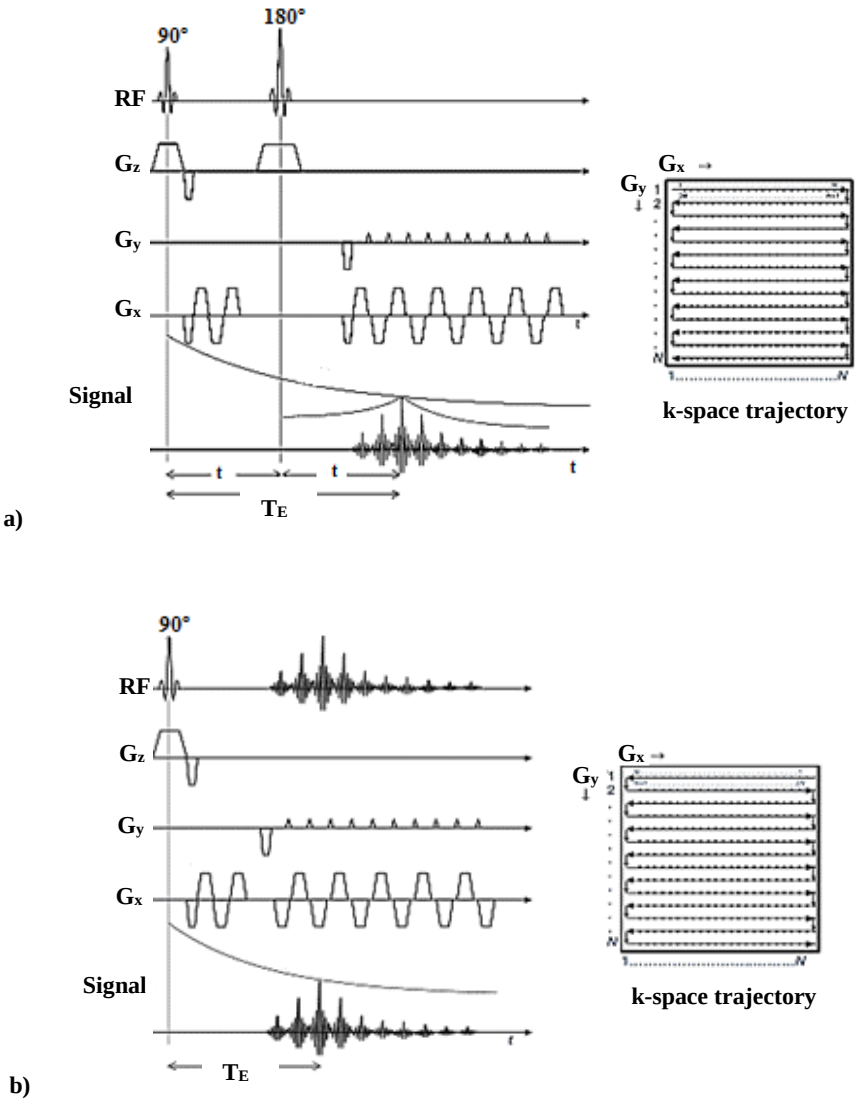

Figure 2.6: 2D EPI sequence and respective k-space trajectory. a) Schematic 2D SE and k-space trajectory. b) Schematic 2D GE and k-space trajectory [40].

2.2.3.3.1 Single-Shot and Multi-Shot EPI

Regarding the k-space sampling, EPI sequences can be divided into two groups: *Single-Shot* and *Multi-Shot* or also named segmented. The main difference between both sequences is on the k-space acquisition.

In a single-shot sequence, in a single excitation (one shot) the entire range of phase encoding steps are acquired [41]. Therefore, all of the k-space data are acquired in only one shot, achieved by generating and reading all of the required echoes from a single FID, figure 2.7a. However, the image acquisition matrix is typically no larger than 128x128. Nowadays, single-shot EPI is the most widely available fast imaging sequence on clinical scanners and facilitates whole-brain coverage at reasonable *Signal to Noise Ratio* (SNR)[1]. Single-shot can easily be

[1] SNR measures the signal strength relative to background noise.

applicable because does not need specialized gradient amplifiers to perform the required gradient switching.

In multi-shot sequence, more excitations are needed to acquire the information of one slice. Also, the range of phase steps is equally divided into several "shots" per slice. Thereby, a subset of G_x is acquired within each T_R and the k-space is acquired in each shot. The shots are repeated until a full set of data is collected, figure 2.7b. This sequence can be applied in *Diffusion -Weighted Imaging* (DWI) and PWI due to the shorter T_E [41].

Comparisons between single-shot and multi-shot EPI reported that in multi-shot, the SNR is higher than in single-shot due to the shorter T_E and presents less susceptibility artifacts due to shorter readouts. However, this sequence requires longer T_R when compared to single-shot for the same number of slices and resolution [41].

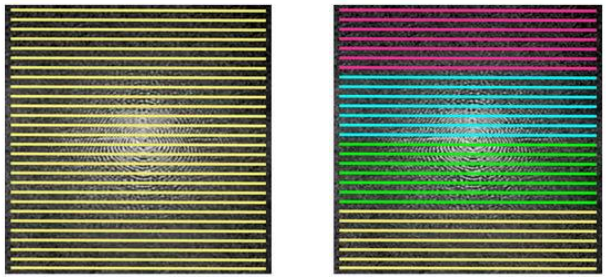

a) **b)**

Figure 2.7: K-space acquisition. a) Single-shot. b) Multi-shot EPI acquisition. Adapted from [42].

2.2.3.4 Echo-planar Imaging with Keyhole (EPIK)

An alternative to EPI sequence is named *Echo-planar Imaging with Keyhole* (EPIK) proposed by Shah et al. [43] and validated by Zaitsev et al. at 1.5T [14]. In EPIK, in the acquisition, each measurement scans the central k-space region completely, whilst the peripheral k-space regions are sparsely sampled resembling a multi-shot scheme, figure 2.8a. A complete k-space can be reconstructed by sharing the sparse region data from the consecutive scans. By applying EPIK sequence, improvements in temporal resolution, reduced signal-loss and reduced image artifacts compared to the single-shot EPI are achieved, figure 2.8b [14, 43].

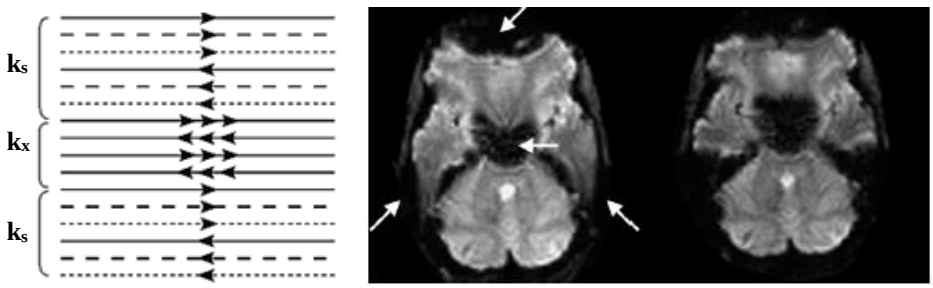

a) **b)**

Figure 2.8: EPIK sequence. a) Schematic representation of the k-space trajectory. Each k-space trajectory is divided into three distinct regions: a keyhole region (k_x) and two sparse regions (k_s). The solid, dashed and fine-dashed lines in k_s regions indicate the sampling positions performed at the 1st, 2nd and 3rd measurements, respectively. b) Brain images acquired in 3T. On the left EPI and on the right EPIK respectively. Adapted from [44].

2.2.4 Instrumentation

While MRI instruments vary considerably in design and specifications, all MRI scanners include several essential components. The *Main Magnetic Field*, *Gradient Field Magnets* and *RF Coils* are the three principal components.

First, for the subject to be scanned a main magnetic field is required. This magnetic field is generally constant in time and space, provided by a variety of magnets. The purpose of these magnets is to induce a net nuclear spin magnetization to the volume of interest.

Second, to induce spatial changes in the polarized magnetic field, gradient field magnets with a specific time and spatial dependencies are required. These spatial changes are able to manipulate the net nuclear spin magnetization so that it is dependent on the spatial localization in the volume.

Lastly, RF coils, both transmitter and receiver coils, are respectively required to transmit RF waves to the volume and to detect the resulting MR signal. While the transmitter coil creates the external B_1 field necessary to excite the nuclear spin, the receiver coil detects the weak signal emitted by the spins as they precess in the B_0 field [45].

2.2.4.1 B_0 Field

In MRI, the B_0 field strength can vary from 0.1T to 14.7T. For clinical practice, the systems currently in use have a field strength of 3T or lower, most commonly 1.5T. In the most systems, a superconducting magnet, using a superconductor current loop, generates a B_0 field. Niobium-tin and niobium-titanium cooled with liquid helium are the superconductors commonly used. Beyond superconducting magnet, resistive magnets can also be used. In spite of requiring more power and operate at lower field strength (≈0.2T), they can be used in so-called open-magnet MRI systems, whose are better tolerated by claustrophobic patients [45]. In research, higher field strengths are used, which can only be generated by superconductor magnets. For human whole-body imaging 7T [46] and for brain imaging up to 9.4T magnets are available [47].

2.2.4.2 Gradient Coils

Gradient coils are used for position encoding. Three pairs of gradient coils are used enabling the generation of linear magnetic gradient fields in the x, y and z directions. A magnetic gradient field is created by placing two coils perpendicular to the axis in which the gradient needs to be created, on both sides of the imaging volume. By inducing currents with opposing directions in the coils, both coils will induce opposite magnetic fields along the axis. As the strength of the field created by a coil depends on the distance from the loop, the sum of the fields from both coils is a linear gradient [46]. The principle of a gradient coil is illustrated in figure 2.9.

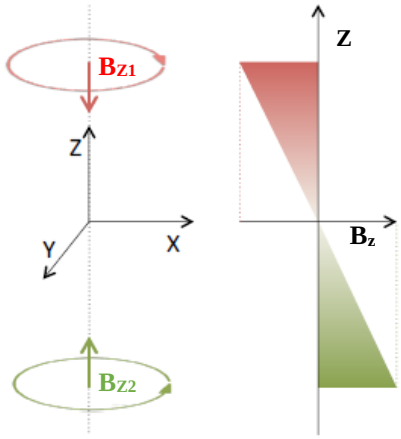

Figure 2.9: The principle of a gradient coil generating a linear gradient in the z-direction. a) Using two coils perpendicular to the z-axis on both sides of the imaging volume, in which opposing currents are induced. b) A linear gradient magnetic field is created in which the field depends on the z-position. Adapted from [34].

2.2.4.3 RF Volume Resonator

RF Volume Resonators are cylindrical or multi-loop coils, which generate a B_1 field perpendicular to the bore axis. RF volume resonators are able to excite the MR signal, essential when deep tissue has to be measured or if a coil does not provide convenient patient access [45]. A typical design of RF volume resonator in both clinical and animal MR scanner is named birdcage resonator [48]. Commonly used as a head or body coil, birdcage resonators can be used in both transmit-receive and only transmit configurations. This coil is used to achieve homogeneous excitation over a subject. The multi-channel coil configuration is advantageous because speeds up the acquisition. Surface coils can also be used to excite the MR signal. Nonetheless, as they can only detect signals from a superficial region, are not so useful for clinical practice.

2.3 Positron Emission Tomography

In 1957, Anger invented the gamma camera considered the start of modern nuclear medicine imaging. Since this invention, some design and operation modifications were done (e.g. pinhole collimators[2] and a rotating gamma camera) allowing tomographic images reconstruction and afterword's, single photon emission images computation [49]. Following a different track than single-photon imaging, in 1959 Anger and Rosenthal presented the first gamma camera with positron-imaging capability [50]. Positron imaging was used at first place to image ^{52}Fe radiotracer distributed in the bone marrow of patients with hematological diseases[3] [51]. Some years later, in 1964, Robertson and Bozzo [52] introduced the first design that resembles the currently used scanner. However, as at that time the computer systems were not powerful enough to enable this system integration, only more than one decade later and after several modifications the device was used for brain imaging [53]. Since the early 1980's, PET was introduced and used in many major hospitals.

PET is a powerful nuclear medicine imaging technique that can be used to measure metabolic activity or body function processes in vivo. The main features of PET are presented in the diagram of figure 2.10. In clinical practice, the patient receives a small intravenous injection of a radiotracer that follows the same pathways as the biomolecules of the body [53]. Therefore, PET images the kinetics and distribution of these biomolecules by detecting the radioactive decay. The concepts related to PET involved in this work will be introduced.

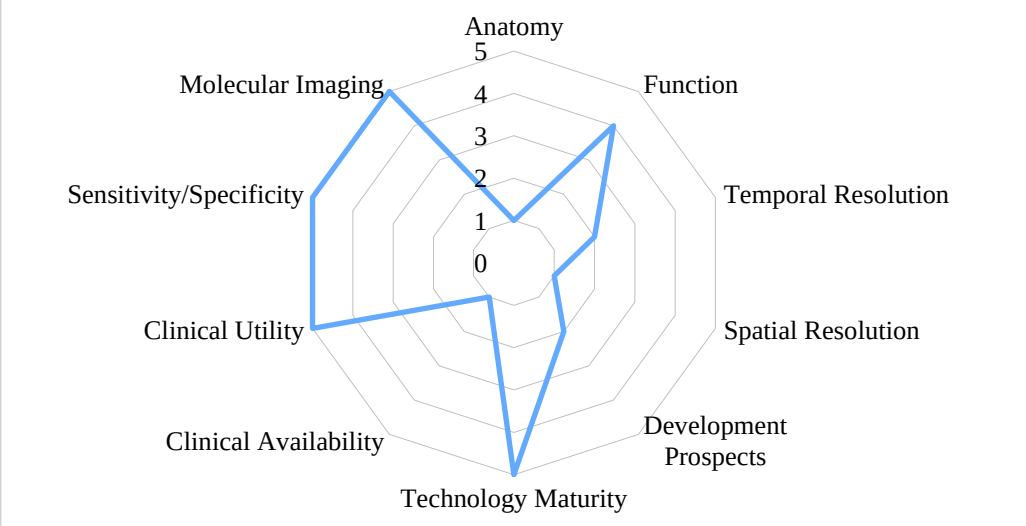

Figure 2.10: Main features of PET. Adapted from [54].

2.3.1 Basic Principles

To measure the physiological and biochemical process of a single molecule in vivo, this technique uses the tracer principle, which states that a radioactive material participates in

[2] Pinhole collimators have a single hole that drilled into the sheet with high atomic number material.
[3] Related to blood disorder.

metabolic reactions in the same way as its non-radioactive counterpart. Based on this principle and by labeling the natural biochemical substance or a drug tagged with a positron-emitting radioisotope (tracer), which are administered intravenously to the patient, it is possible to measure the concentration of the radiotracers during the time observed [55, 56].

These images are produced as a result of the isotope decay which emits a positron (β+). This β+ annihilates with an electron (e-) of a nearby atom producing two 511 keV photons that leave the annihilation site in opposite directions (180 °degrees apart),
figure 2.11. If the scanner detects the two photons almost at the same time, it is assumed that those have been originated from the same positron emission. In this case, the detection of both photons is named *Coincidence* [54, 55].

For PET imaging, the time information provided by the module is important, because two incident photons can only be considered a coincidence if both photons are detected within a certain time window, defined as *Coincidence Window*. The coincidence detection is performed online by the coincidence electronics of the scanner and the coincidence window is determined by the resolution time of the modules. The total of events detected by the coincidence on the defined window is referred to as a *Prompt Coincidence*. For each prompt coincidence, a *Line of Response* (LOR) along the annihilation occurred is determined, figure 2.11b.
The combined information of all the measured LORs during the acquisition is used to get information about tracer distribution, allowing the producing of a 3D image. It is important to keep in mind that radioactive decay is a random process, following a *Poisson* distribution. Consequently, detected and acquired data by the scanner will contain Poisson noise [56].

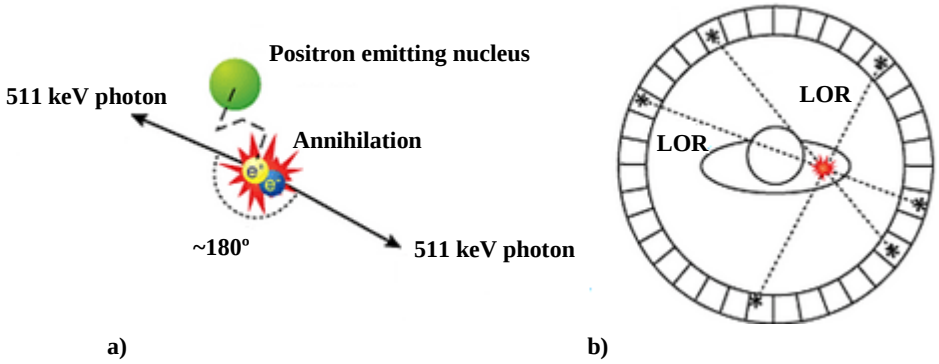

Figure 2.11: PET imaging principle. a) After the annihilation of a positron and an electron, two 511 keV photons are emitted in opposite directions (~180°). b) When two interactions are simultaneously detected within a ring of detectors surrounding the patient, it is assumed that an annihilation occurred on LOR connecting the two interactions. By recording many LORs the activity distribution can be tomographically reconstructed. Adapted from [57].

However, not all the prompt events detected by PET system are true events, because there is a probability of a photon to escape from the *Field Of View* (FOV) of the scanner or to be attenuated into the body. Therefore, *Scattered*, *Random* and *Attenuation Events* can also be detected.

Scattered Events are a consequence of the interaction of at least one photon from the annihilation with the matter (e.g. Compton Effect)[4], which could induce changes of its direction before the detection, figure 2.12a.

[4] Dominant effect at 511KeV

Random Events are coincidences detected by the PET scanner within the coincidence window but both detected photons are originated from a different positron emission, figure 2.12b [56]. Both events do not contain relevant information and cause image degradation.

Moreover, during the travel through the tissue the photons can also be absorbed by the tissue, resulting in loss of PET signal, named *Attenuation Event*, figure 2.12c.

Considering these events, an estimated number of true coincidences could be set. Wherefore, from the estimated number of true coincidences during a certain time, it is possible to quantify the tracer distribution as a spatial and time function. For that reason, prompt events must be corrected from several factors. Further information can be found in [56].

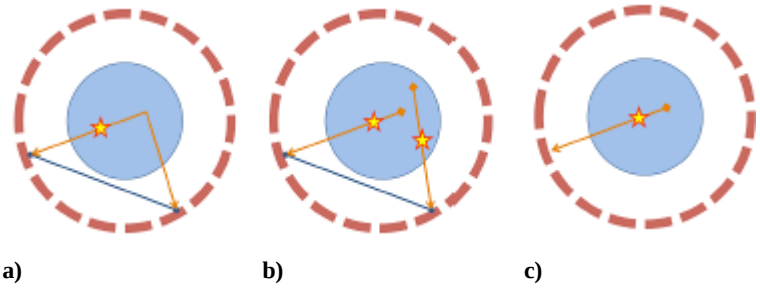

Figure 2.12: PET events. a) Scatter. b) Random coincidences. c) Attenuation. Adapted from [34].

2.3.2 Image Reconstruction

After the understanding of the basic principles of PET and the importance of correcting data required to quantitative and qualitative PET, it is important to understand how the data is organized and reconstructed. In this subsection data acquisition, organization and reconstruction will be explained. Further information can be found [59, 60].

2.3.2.1 Data Acquisition and Organization

Despite the 2D or 3D data acquisition, PET data acquisition can also be acquired in different modes related with the temporal information. Currently, the standard data acquisition is named *List-Mode* and will be the one that will be mentioned. List-mode acquisition is a versatile scheme, which allows flexible post-acquisition time schemes. This mode enables to acquire static, dynamic or gated images and several photon characteristics for each event (e.g. time, spatial coordinates and energy of the photon) can be recorded.

A static image represents a time average of the radiotracer distribution over the data acquisition time, introducing only spatial information. From the list mode data, a static image is obtained by summing all the events weighted by the acquisition time. These images are often used when the dynamic of the radiotracer changes very slowly or when it does not include extra information [58, 60]. Otherwise, dynamic and gated images are a sequence of images, which includes time information of the radiotracer distribution. While dynamic images are used to assess to organs functionality with kinetic analysis, gated images are used mostly in cardiac images, where the image acquisition should be synchronized with the cardiac or breathing cycles [60].

After data acquisition and before be reconstructed, PET data needs to be organized. Sinograms are the matrices used to organize the data, which relate the LOR information with the spatial place in the FOV [60]. These structures consider that each LOR in 2D PET can be

characterized as a *Projection* (p), equation 2.12, by the cartesian distance to the center of FOV (s) and an angle (ϕ) that explains the orientation of the LOR. These LORs or projections are related with activity concentration $A(x, y)$ in the Cartesian coordinates in the FOV by the Radon transform, $L(\Phi, s)$:

$$p(\Phi, s) = \int_{L(\Phi,s)} A(x, y)dl\ (\Phi, s) \quad (2.12)$$

As PET data is acquired in 3D acquisition mode, two variables needed to be added. One related with the obliqueness of the LOR with respect to the transaxial plane (θ) and the other one related to the position in the axial direction (z). Further information can be found in [60].

2.3.2.2. Data Reconstruction

The goal of image reconstruction is to recover the radiotracer concentration from the acquired data. Reconstruction scheme uses a set of *Projections* (p), the *System Model* (H) and the *Error of the Observations* (n) to find the *Unknown Image* (f) [54]. One way to represent the imaging system is as follows in equation 2.13:

$$p = Hf + n \quad (2.13)$$

Different methods have been proposed for PET image reconstruction and can be subdivided into two groups, *Analytical* and *Iterative Methods* [59].

Analytical reconstruction assumes deterministic models and uses the inverse Radon transform to obtain a mathematical solution to the system model. The deterministic approach has the advantage of simplifying the reconstruction process, making it fast and easy. However, this approach oversimplifies, by neglecting the noise presented in the system leading to reconstruction artifacts.

On the other way, iterative reconstruction methods assume that the data is stochastic derived from physical factors such as: positron decay process, effects of attenuation, scatter and random. Unlike analytical reconstruction, iterative reconstruction methods converge to closer solutions at each iteration for a set of constraints and have the advantage of higher accuracy, by not neglecting the influence of noise [60]. Although, this method is much more computationally demanding than analytical methods. Further information can be found [60, 61].

2.3.3 Data Correction

As stated before, prompt events must be corrected from several factors in order to obtain a good image quality. Some factors are caused by the interaction of the photons with the matter and others by some characteristics of the scanner. Considering the interaction of photons with the matter, *Scatter, Attenuation* and *Random Corrections* have to be performed.

Scatter Event is characterized by inducing a blurring on the image, reducing image contrast and causing image degradation. To correct such effect, two different strategies can be

applied [62]. One strategy is based on photon energy since scattering of a photon leads to a reduction of the energy of the photon and the other one, based on the estimating of the remaining amount of scattering in the acquired data by numerical calculations. At the *Forschungszentrum Jülich*, in the BrainPET scanner, the second strategy is applied. Further information about this method can be found in [63].

Random Events also result in a decrease of image contrast. Random events become significant, compared with true events, when detector rates are very high. This fact is more problematic for detectors with low detection efficiency and for 3D imaging. The rate of random events between two detectors is given by:

$$R = 2\tau R_i R_j \quad (2.14)$$

, where Ri and Rj are the rates of random events in detector i and j, respectively.

Moreover, for random events correction, two methods can be considered. One uses a single time window and the other one uses two-time windows, named delayed time window method. In the BrainPET scanner, it is implemented the second method. Further information about this method can be found in [63].

Attenuation Event is the one it has higher visual and quantitative effect from all the described corrections. This event is characterized by reducing the image intensity due to the absorption in the tissue of some photons. The fraction of photons that penetrate through the tissue is named *Transmitted Fraction* (TF) and is determined by the attenuation coefficient (μ) given by:

$$TF = e^{\int -\mu(s)ds} \quad (2.15)$$

, where the line integral represents the path that is traveled by the photon.

In order to correct data from attenuation, it is required the knowledge of an attenuation map (m-map) and the transmission image. However, as currently no standalone PET scanners are available in the market to derive the m-map, the transmission image needs to be post-processed with a scaling factor (linear or non-linear) and with a post-filtering Gaussian smoothing. The filter is required for data co-registration, when more than one technique is combined (MR/PET scanner). Further information about attenuation correction can be found in [63].

Considering now the characteristics of the scanner that compromise the image quality, *Dead Time, Normalization* and *Motion* can be denominated.

The *Dead Time* of a detector corresponds to the interval where none photon is detected. This event is particularly troublesome, in especial for coincidence detection, because both photons must be detected. Therefore, to correct this characteristic is advisable to use systems with many independent detectors or requiring faster PET scintillators and processing electronics.

Normalization Correction Method corrects the image for both scanner geometry and crystals efficiency. Having in mind that PET acquisitions are done in 3D, more LORs contribute to the same voxel in the space and so on more random and scatter events are detected comparing with the 2D PET acquisition, figure 2.13. In one hand the central detectors are crossed by a higher number of LORs and are more sensitive. On the other hand, at the edges of the scanner the detectors are intersected by fewer LORs and consequently are less sensitive. Therefore, both differences in geometric sensitivity and different detectors efficiently must be corrected using normalization methods [63].

Motion Correction is also an important factor to be corrected because movements of the patient during the PET acquisition introduce a blur in the acquired data. Particularly in brain imaging, head movements often occur in scans in long acquisitions, such as in a dynamic ^{18}F-FET PET (approximately one hour). The simplest method to reduce the patient motion is to use immobilization devices. However, they are very uncomfortable for the patients. Nowadays alternative off-line frame-by-frame methods can be used. This method measures the degree of the movement between frames and further calculates the correction parameters. Choosing a reference image, the frames will be co-registered with the reference imaging choosing the metric.

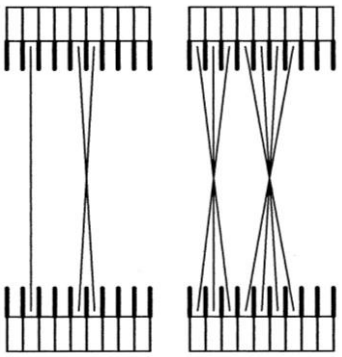

a) **b)**

Figure 2.13: PET data acquisition. a) 2D. b) 3D. Adapted from [63].

2.3.4 Positron Tracers

2.3.4.1 Positron Emitters - Radioisotopes

The operation of PET needs to labeled biological molecules like glucose ($C_6H_{12}O_6$), oxygen (O_2) or proteins. These molecules are label using radionuclides such as carbon (^{11}C), oxygen (^{15}O), nitrogen (^{13}N) and fluorine (^{18}F). In this way, all the isotopes used are radioactive with a rapid time of decaying by positron emission (short half-life) and with a limited positron range. Both facts contribute to a good image quality [56].

For large proton-rich nuclei, the main form of decay is via positron emission, where one atomic proton (p^+) decays into a positron (β^+) and a neutron (n^0), equation 2.16.

$$p^+ \rightarrow n^0 + \beta^+ + \upsilon^0 + \text{energy} \quad (2.16)$$

, where υ^0 is a neutrino, balancing the energy momentum and angular momentum of the initial and final state.

The most commonly used isotope in PET scans is ^{18}F due to its longer half-life (109.77min), which allows supplying places far from the molecular probes. ^{18}F decays by emitting positrons with the lowest maximum energy of the emitted positron ($E_{\beta^+_{max}}$=0.634MeV), equation 2.17 [63].

$$^{18}F \rightarrow {}^{8}O + \beta^+ + \upsilon + 0.634\ \text{MeV} \quad (2.17)$$

2.3.4.2 Radiotracers used in Brain Studies

Tracer compounds are used to track biochemical and physiological processes rather relevant particularly for brain studies. Currently, evaluation based on PET imaging in brain tumors is conducted by means of mainly three radiotracers. The glucose analogue *^{18}F-Fluor-Deoxy-Glucose* (FDG) and the radiolabeled amino acids *^{11}C-Methyl-L-Methionine* (MET) and O-*(2-[^{18}F]-Fluorethyl)-L-Tyrosine* (FET) [7]. A brief description of each one will be presented in this subsection.

2.3.4.2.1 ^{18}F-Fluoro-D-Glucose (^{18}F-FDG)

The radiotracer ^{18}F-FDG is derived from 2-deoxy-d-glucose and gives information about the first steps of glucose metabolism. ^{18}F-FDG is used in brain studies allowing an accurately staging and differentiating between malignant and benign lesions. As malignant brain tumors are characterized by an increase in glucose consumption, differences between healthy and tumor regions can be visualized using this radiotracer [63].

Some studies have already published a well-established relationship between histological features and radiotracer uptake for ^{18}F-FDG [7, 67]. Consequently, ^{18}F-FDG has been shown to be a valuable tool for guidance of stereotactic biopsies in human gliomas.

2.3.4.2.2 ^{11}C-Methyl-L-Methionine (^{11}C-MET)

Beyond glucose consumption, tumor cells are also characterized for irregular protein mechanisms. Methionine is a naturally occurring essential amino acid being crucial for the formation of all the proteins. This amino acid is labeled with carbon-11 (^{11}C) forming the ^{11}C-Methyl-L-Methionine (MET) radiotracer [68]. Therefore, ^{11}C-MET uptake is mainly determined by a specific carrier-mediated mechanism, which correlates with proliferative activity and micro-vessel density in tumor cells [69].

Considering the use of ^{11}C-MET in brain studies, particularly in gliomas diagnosis, MET uptake is influenced by its specific activity in plasma, molecules transference across the *Blood-Brain Barrier* (BBB)[5], intracellular metabolism and the incorporation of ^{11}C-MET in proteins. Thereby, a disruption of BBB is not a prerequisite for an increased ^{11}C-MET uptake but a damaged in BBB may enhance leakage of the tracer to the extracellular space, contributing to its increased uptake in malignant gliomas [70]. Moreover, ^{11}C-MET exhibits a short half-life since depends on ^{11}C decay and for its production it is required an on-site cyclotron, which is disadvantageous.

2.3.4.2.3 ^{18}F-FluorEthyl-L-Tyrosine (^{18}F-FET)

More recently, ^{18}F-FET tracer was introduced with main interest for brain studies. ^{18}F-FET measures the magnitude of amino acid transport and its distribution in the tumor but does not participate in any metabolic pathway directly [63]. Unlike ^{11}C-MET, ^{18}F-FET is not

[5] BBB is a highly selective permeability barrier that separates the circulating blood from the brain extracellular fluid in the central nervous system (CNS).

incorporated into proteins but rather mediated by an active transendothelial amino acid transporter denoted LAT2 (Linker for activation of T cells family, member 2) [67]. LAT2 has not been identified in inflammatory cells, which precludes the uptake of ^{18}F-FET in inflamed tissue. This fact potentially makes ^{18}F-FET even more tumor specific than ^{11}C-MET and ^{18}F-FDG [71, 72]. Moreover, ^{18}F-FET has a longer half-life (~109 minutes) enabling tracer production in a central cyclotron and its transport to other units facilitates the PET acquisitions [7].

In tumor imaging, ^{18}F-FET shows a high uptake in tumor regions due to its increased transport and suitable uptake kinetics. The uptake of ^{18}F-FET in brain tumors reaches a plateau approximately 20 minutes post-injection. However, in normal tissues *Gray* (GM) and *White Matter* (WM), the uptake continues to increase for a longer period, leading to lower *Tumor-to-Brain Ratio* (TBR) from 20 to 60 minutes after injection [74]. TBR is calculated by the ratio between the tumor area and the brain tissue of normal-appearing. For gliomas, this value was defined to 1.6 [73], i.e. the tumor area corresponds to the area with a metabolic activity 1.6 times higher than the background brain.

In clinical practice, ^{18}F-FET and ^{11}C-MET have been shown to be equally sensitive and specific [72]. However, for lower malignancy tumors (e.g. low-grade glioma), ^{18}F-FET shown a better efficacy in tumor delineation. In this manner, ^{18}F-FET demonstrates convincing results especially in the diagnostics of brain tumors and treatment planning [73-75].

2.3.5 Instrumentation

Detection systems are a key component of PET imaging system. An understanding of their properties and design it is important to obtain quantitative information. *Scintillation detectors*, *Photodetectors* and *Photomultiplier tubes* are the main components of PET systems [76]. Usually, a PET detector system uses a multiple-block-detector arrangement with a detector blocks arranged in a ring structure.

Scintillation detectors are the most used radiation detectors in PET imaging. A scintillator is used to detect gamma photons. As in PET imaging, the main interest is to detect gamma photons with a specific energy (511 keV), only photoelectric absorption and Compton scattering are relevant interaction mechanisms to detect. Moreover, for an accurate detection, the scintillator should have a high light yield and low decay time. A fast decay time leads to short coincidence windows that will limit the number of random coincidences. The output of the scintillator is a weak light signal and then signal amplification is required. Therefore, a *Photodetector* is used to convert the weak light output of the scintillator into a detectable electrical signal.

Photomultipliers Tubes (PMT's) have had a huge use in PET due to the combination of high gain, stability and low noise. PMTs is composed by a light transmitting window, a photocathode, a series of electrodes (dynodes) and an anode inside a glass envelope, in vacuum. The electrons are collected in the anode where a measurable current is produced [77]. Nevertheless, a new range of photodetectors has experienced an increased use in PET due to their advantages over PMTs, named *Solid-State Photodetectors*. These types of detectors are used in MR/PET systems due to the lack of response to magnetic fields. In PET system is used a solid-state photodetector also known as *Avalanche Photodiode* (APD). Further information can be found in [78].

2.4 Hybrid Imaging

Nowadays, a wide number of medical imaging are available for clinical practice. CT, PET and MRI are the main techniques used in brain studies. CT provides anatomical information, PET provides functional/metabolic information, while MRI provides anatomical and functional/metabolic information [1, 25]. As each modality has strong and weak highlights, the combination of different information in one single image brings clinical benefits. The simultaneous acquisition of two different techniques compacted into one scanner is known as Hybrid Imaging [1]. PET/CT and MR/PET are the principle hybrid systems available for clinical practice.

On the previous sections, MR and PET principles involved in this work were introduced. In this section, the combination of both techniques in a hybrid scanner, particulary for brain studies, will be addressed. The characteristics of this technique are illustrated in figure 2.14. Further information can be found in [79, 80].

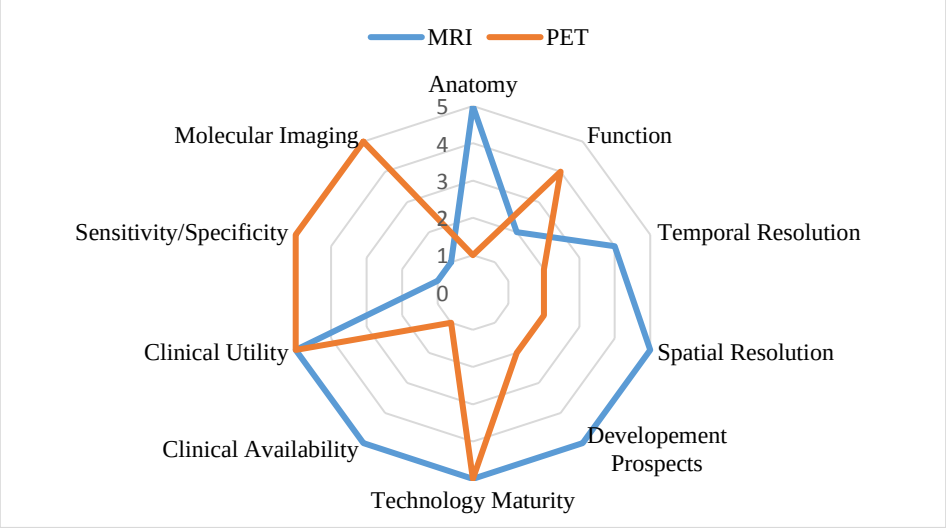

Figure 2.14: Features of MR/PET. Adapted from [32].

2.4.1 Magnetic Resonance (MR)/ Positron Emission Tomography (PET)

From the information presented in the previous subsections, the combination of MR/PET can be considered important in clinical practice. Beyond MR and PET standalone, by combining both techniques, a versatile high resolution anatomical, functional and molecular imaging it is possible to achieve. Regardless of the advances, the limitations of MR/PET might be the associated higher costs and the selection of an efficient PET tracer [1, 80].

For brain studies, combination of MR and PET improves tumor diagnostic. In one hand, MR imaging allows the differentiation between brain regions with normal cells (healthy tissue) from regions with tumor cells (tumor tissue). However, the differentiation of tumor tissue from unspecific changes in the surrounding tissue shows to be difficult. On the other hand, PET imaging provides information about tracer uptake revealing information about the tumor activity

[55]. Hereupon, by combining both techniques localization, state and growth tumor information can be easily accessed comparing with MRI and PET standalone instruments [81].

2.4.2 Instrumentation

2.4.2.1 Design of MR/PET Scanner

In the mid of 1990's Hammer and co-workers [82] addressed the first design of MR/PET system. In this first system, the PET scintillator blocks inside a clinical MRI. The information is extracted from the scintillator through light guides that are fed into the electronics detector. These detectors are situated outside of the primary magnetic field of the MRI system. Some years later, improvements on the design were done. In the mid of 1990s, Shao and co-workers developed a small ring of PET detectors with a diameter of 3.8 cm for pre-clinical small animal imaging [83]. On the following years, subsequent prototypes were suggested for different groups [84, 85]. Since 2006, the simultaneous MR/PET system for human brain became available on the market.

Based on these facts, it is possible to distinguish three different approaches towards MR/PET system [84]. On the first design, the gantries are separated and operated in different rooms. So on, the patients have to be transferred between separate MR and PET systems. The image acquisition is not simultaneous and images are acquired with a delay, figure 2.15a. On the second design, the gantries are arranged in line with the main scanner axis, figure 2.15b. The patient handling system is mounted in between. In this system, the delay between MR and PET acquisitions has to be taken into account but is reduced comparing with the first design. Moreover, in 2006, it was developed the more recently design a simultaneous MR/PET system, figure 2.15c. Both systems are together forming a fully integrated system where the delay is absent. In this system, the PET detector ring was designed as an insert that can be placed inside a MR system. In our project the data it was acquired using a more recent design. Further specifications of this system will be explained in the next section.

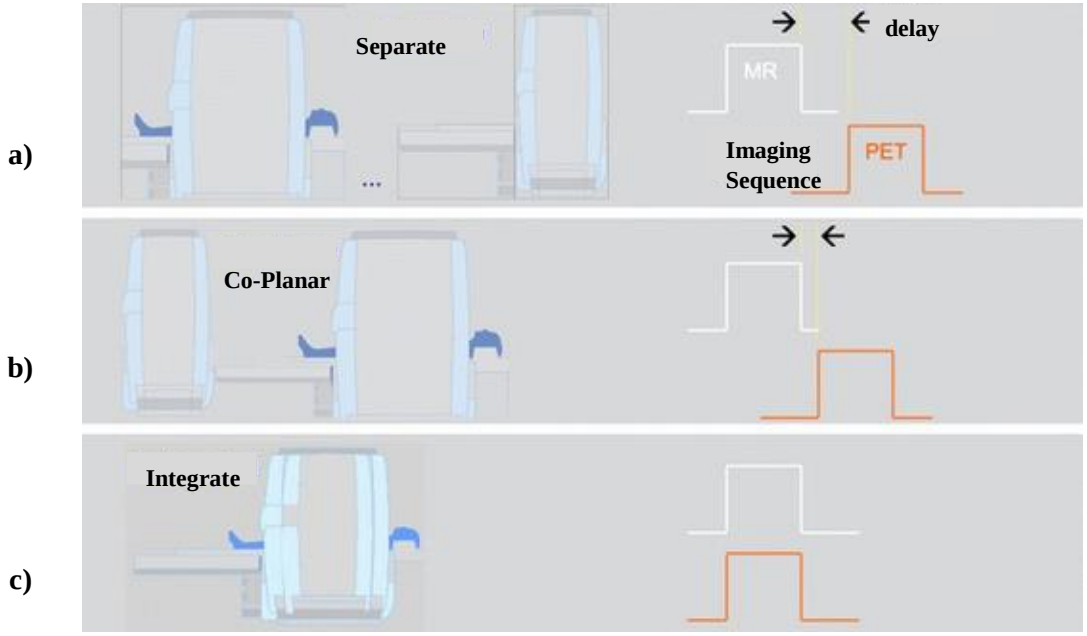

Figure 2.15: Different designs for combined clinical MR/PET systems. a) Patients can be shuttled between separate MR/PET systems operated in different rooms. b) Patients are positioned on a common table platform between stationary PET and MR systems; the delay between the MR and PET examination is reduced (Philips Healthcare). c) Patients are positioned inside an integrated MR/PET gantry (Siemens Healthcare) with a PET insert that is mounted within a whole-body MR offering simultaneous MR/PET acquisition. Adapted from [85].

2.4.2.2 The BrainPET System

The BrainPET system was the first prototype of an MR-compatible PET scanner for human imaging. In the *Forschungszentrum Jülich*, the high resolution BrainPET is installed since 2008, in a 3T Magnetom TRIO MR scanner by Siemens figure 2.16. The BrainPET is inserted inside of the MR bore on the center of the magnet. The PET inserts are based on APDs since conventional photo multipliers do not work inside the magnetic field of the MR scanners [86, 87]. MR scanner and BrainPET insert can also be operated as standalone medical imaging devices.

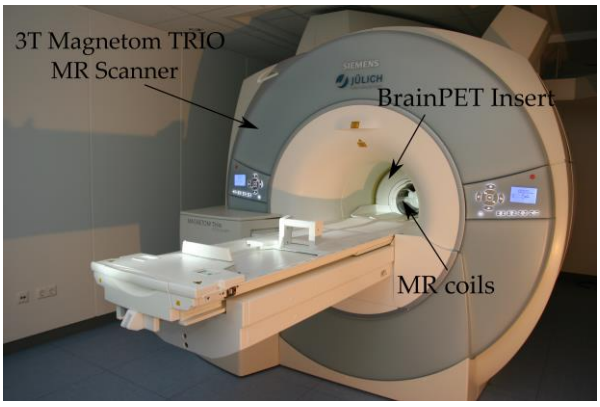

Figure 2.16: Hybrid 3T MR-BrainPET system present in INM-4 *Forschungszentrum Jülich*. The BrainPET is inserted between the magnet and the MR coils. Adapted from [88].

2.4.2.3 The BrainPET System Geometry

The BrainPET is a compact cylinder with a length of 72 cm and an outer diameter of 60 cm fitting into a bore of the magnets. Within its inner diameter of 32 cm, there is a birdcage head coil used for transmitting radiofrequency pulses and receiving the signals and inner 8-channel coils for receive only. The BrainPET consists of 32 copper-shielded cassettes arranged radially and each cassette contains six *Lutetium Oxysilicate Scintillation Crystals* (LSO) detector modules covering an axial FOV of 19.2 cm. The front end of the detector block is composed of LSO-APD modules whose are formed by coupling the LOS with 12x12 matrix of 2.5x2.5x20 mm^3 coupled with APD with a 3x3 array. Thereby, the LSO-APD detector arranges in the z direction, resulting in 72 crystal rings [86, 87]. In figure 2.17, it is illustrated the BrainPET components.

Moreover, each detector module contains a high voltage board supply, supplying 500V to the APDs, a board with a charge sensitive pre-amplifier ASIC and an output driver board. The system is cooled with air and each cassette is connected to a data acquisition electronic via 10m long cables. Furthermore, the BrainPET provides a resolution of 3 mm at the center. The positioning of the BrainPET insert in the center of the magnet offers the opportunity for iso-center imaging in space and time.

The BrainPET detectors installed in the *Forschungszentrum Jülich* MR-PET Scanner deliver high-resolution images. In order to produce high-quality PET images, a quantitative data of metabolic functions, an iterative reconstruction and efficiency and a random, attenuation, scatter, dead time and decay corrections are available [86].

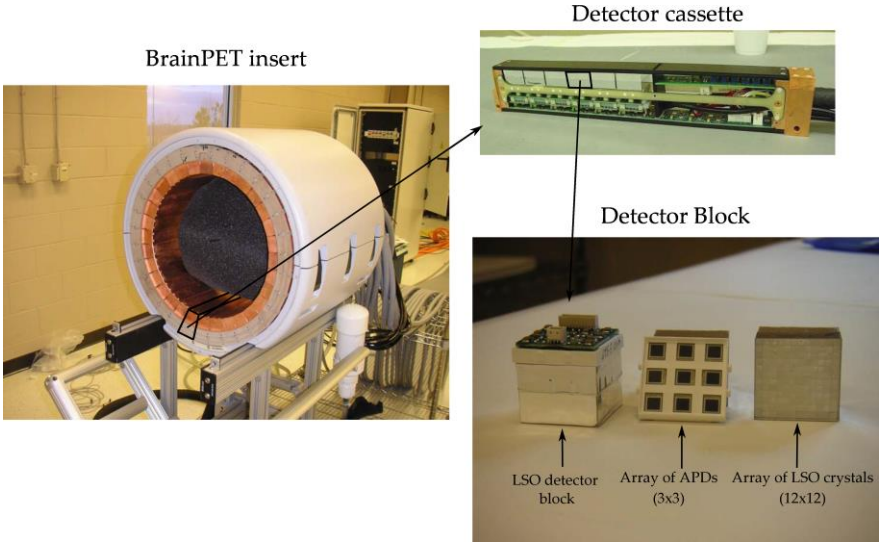

Figure 2.17: BrainPET component. Brain PET insert, detector cassette and detector block respectively. Adapted from [88].

2.5 Brain Tumors

2.5.1 Gliomas

Gliomas are central nervous system tumors that result from an uncontrolled proliferation of glial cells, the cells that provide support and protective functions to the neurons. Unlike neurons, glial cells in the human brain have the ability to divide and multiply. The deregulation of these processes gives rise to this type of tumor. The clinical management of gliomas is a true challenge in oncology due to their large impact on the patient and relative insensitivity to most conventional therapies [89]. In this subsection, classification and grading of gliomas will be introduced as well as, it inherent vasculature will be exploited.

2.5.1.1 Classification and Grading of Gliomas

According to the classification of the *World Health Organization* (WHO), it is possible to distinguish three main types of gliomas by their histologic features: *Astrocytomas*, *Oligodendrogliomas* and *Oligoastrocytoma* (a mixed form with both oligodendroglial and astrocytic components). These tumors are typically heterogeneous, which means that different levels of malignant degeneration can occur in different regions within the same tumor. Therefore, lower malignancy corresponds to *Low-Grade Gliomas* (LGG) - grades I and II and higher malignancy to *High-Grade Gliomas* (HGG) - grades III and IV. LGG are considered benign tumors, while HGG are malignant and carry a worse prognosis [90].

The LGG are characterized by slowly growing. While, grade I gliomas rarely spread to other tissues and tumor cells may be removed by surgery due to the similarity to normal cells, in grade II gliomas the tumors may spread to nearby tissue and some of them may become higher-grade tumors afterwords. In contrast, in HGG the grade III and IV grow quickly and are likely to spread into nearby tissue [91]. Furthermore, its even possible to define different subtypes of LG and HG gliomas. LGG can be distinguished in pilocytic astrocytoma (grade I), astrocytoma (grade II) and oligodendrogliomas (grade II). HGG can be distinguished in anaplastic tumors astrocytoma and oligodendroglioma (grade III) and glioblastoma (grade IV) [91].

Nevertheless, this current standard criterion for tumor grading based on histopathologic[6] assessment has two major limitations. It is an invasive procedure and it has an inherent sampling error, especially with stereotactic biopsy[7] [91]. Thereby, gliomas diagnosis and grading using vascular information from MR/PET techniques may overcome these limitations.

[6] Histopathologic assessment is a microscopic examination of tissue. In clinical medicine, refers to the examination of a biopsy or surgical specimen by a pathologist after the specimen has been processed and histological sections have been placed onto glass slides.

[7] Stereotactic brain biopsy is a minimally invasive procedure that uses this technology to obtain samples of brain tissue for diagnostic purposes.

2.5.2 Tumor Vasculature

2.5.2.1 Tumor Heterogeneity

The normal vasculature is arranged in a hierarchy of evenly spaced, well-differentiated arteries, arterioles, capillaries, venules and veins. In contrast, the tumor vasculature is composed of a chaotic mixture of abnormal hierarchically organized vessels that differ from those of normal tissues with respect to organization, structure and function. Unlike normal blood vessels, those supplying tumors commonly follow a serpentine course, branch irregularly and are in average larger than their normal counterparts, figure 2.18. The increasing diameter of the vessels impairs tissue nutrition, resulting in an inefficiently O_2 and nutrients feeding, as is demonstrated by the increasing O_2 content of the venous blood draining. Another long-recognized property of tumor blood vessels is that they are hyperpermeable to plasma and plasma proteins although, hyperpermeability is confined to only a subset of tumor blood vessels.

Thereby, it has been recognized that tumor blood vessels are heterogeneous and both tortuosity and dilation are its principal visible characteristics. *Tumor Heterogeneity* difficults both the evaluation and prediction of tumor vessels architecture, only accessed using an invasive technique, such as biopsy. However, a complete vessel distribution cannot be accessed by biopsy alone, because this technique is usually confined only to one or two portions of a tumor [24].

2.5.2.2 Angiogenesis

As all the cells in human body, brain tumor cells need O_2 and nutrients to grow and survive. *Angiogenesis* is the natural process responsible for the formation of blood vessels from pre-existing vasculature i.e. new networks (e.g. capillary blood vessels) or vascular supply from the existing cells. Hereupon, angiogenesis is one of the hallmarks of tumor required for tumors growth, as satisfy their need for O_2 and nutrients [92].

The regulation of the growth of new vessels is done by pro- and anti-angiogenic molecules. Certain factors can disturb the balance of new vessels by stimulating the production of pro-angiogenic molecules such as hypoxia, pH, mechanical stress and inflammatory response. Hypoxia[8] is the factor with the greatest impact arising when the nearest functional blood vessels are too far way to deliver sufficient O_2 to the tumor cells [92]. This fact leads to the expression of *Vascular Endothelial Growth Factor* (VEGF), which consequently will promote the growth of new blood vessels. The overproduction of pro-angiogenic factors causes an abnormal tumor vasculature in both morphology and function. However, compared to normal blood vessels, the new vessels are characteristically abnormal by virtue of having increased tortuosity (figure 2.18) and increased permeability to macromolecules due to the presence of large endothelial cell gaps. Consequently, new vessels often have both abnormal flow characteristics and abnormal permeability that can be exploited as potential surrogate markers for the evaluation of tumor growth. Further, tumors cannot enlarge beyond 1 to 2 mm unless they are vascularized.

The vascular abnormalities and dysfunctional vasculature contribute to greater malignancy [93] and lead to an irregular delivery of chemotherapeutics to the tumor, whose can reduce the efficacy of radiation therapy. Thereby, angiogenesis plays a very important role in tumor vascular function.

[8] Deficit of available oxygen.

Judah Folkman in 1971, proposed the concept of inhibiting angiogenesis for treating tumors [94]. Indeed, recent findings from pre and clinical studies of antiangiogenic therapy for brain tumors showed that by inhibiting and controlling angiogenesis, it is possible to manage the tumor treatment. By predicting the area with a higher increase vessel caliber, a more precise treatment and a guided therapy can be performed.

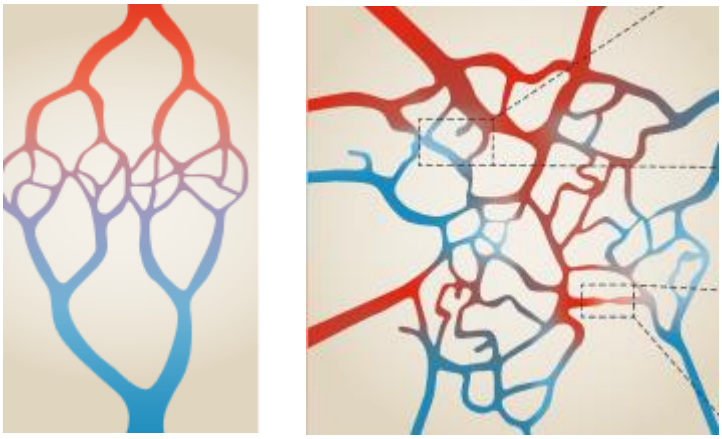

a) **b)**

Figure 2.18: Vessel caliber in solid tumors. a) Normal blood vessels. b) Tumor blood vessels. Normal vessels form highly organized capillary beds, which are well suited for the delivery of O_2 and nutrients to the tissue. The red vessels indicate oxygen-rich feeding arteries and arterioles, blue vessels are veins carrying deoxygenated blood and the intermediate regions indicate a transient capillary stage. Tumor vessels are disorganized with large, tortuous vessels, blind ends and frequent branching, which may lead to poor perfusion and collapse of non-functional vessels. Slow blood flow is indicated by reduced color intensity. The points represent hypoxic regions. Adapted from [95].

3. Dynamic MRI Contrast Agent: Basics and State of the Art

In the *Chapter 3* the strategies described in the literature to provide information about state, localization and size of brain tumors using perfusion will be discussing. The DSC-MRI perfusion method will be introduced as well as the combination of GE and SE sequences and the advantages of using multi-echo sequences. *Vessel Size Imaging* (VSI) methodology will be explored and clinical and human studies will be reviewed. Furthermore, ^{18}F-FET PET and MR/PET studies using perfusion MR will also be addressed. In the end of this chapter, the mainly motivation of our work will be highlight.

3.1 Introduction

Clinical perfusion contrast-enhanced MRI is currently recognized as one of the most powerful tools for assessing tumor vascularization through the evaluation of hemodynamic parameters. As tumor vascularization is abnormal, its information can be used for tumor diagnosis. In 1991, Fisel [96] and others concluded that T_2-weighted perfusion MR images were sensitive to vessel caliber. Motivated from these conclusions, some years later, a new perfusion vascular methodology was introduced named VSI [25], allowing the estimation of the vessel caliber of brain tumors. As stated on *Chapter 2*, amino acid PET tracers, particularly ^{18}F-FET demonstrated a greater potential for gliomas diagnosis. Hereupon, by combining both VSI and ^{18}F-FET information, it is expected to access an accurate tumor diagnosis, which could potentially be an alternative to biopsy.

3.2 Contrast

Apart from differences in the local water content, the basic contrast in MR images results from regional differences in the intrinsic relaxation times T_1 and T_2. Each one can be independently chosen to dominate image contrast [97]. However, the intrinsic contrast provided by water in T_1 and T_2 are often too limited to enable a sensitive and specific diagnosis. For that reason, *Contrast Agent*s (CA), which alters the image contrast following intravenous injection, are readily used in neuro-oncology.

Tumor blood vessels are more permeable to large molecules than many normal vessels providing an intriguing mechanism for selective delivery of macromolecules in malignancy tissues. This concept explains the enhanced permeability of the tumor and its identification in contrast-enhanced MR images.

The most used CA is the paramagnetic Gd-DTPA. Gd-DTPA is a paramagnetic BBB contrast, which means that BBB disruption could be visible [98]. This characteristic is useful for tumor delineation, particularly for malignancy tumors, because higher malignancy is featured by BBB disruption. Nevertheless, using this contrast enhanced both T_1 and T_2 relaxation enhancements images with different contrast can be are produced (brightening or darkening, respectively) providing important diagnostic information.

3.3 Basics of Perfusion

Perfusion and *Vascular Permeability* quantification can provide important information about state and size of brain tumors. Perfusion is a fundamental biological function that refers to the delivery of O_2 and nutrients to tissue by means of blood [2]. There are two major approaches to measure cerebral perfusion with MRI, with or without using an exogenous CA. The first group includes DSC, while the second group relates to *Arterial Spin-Labeling* (ASL), figure 3.1. Perfusion MRI is sensitive to microvasculature providing vascularity information, which yields the possibility of been applied in the classification of tumors [3, 4].

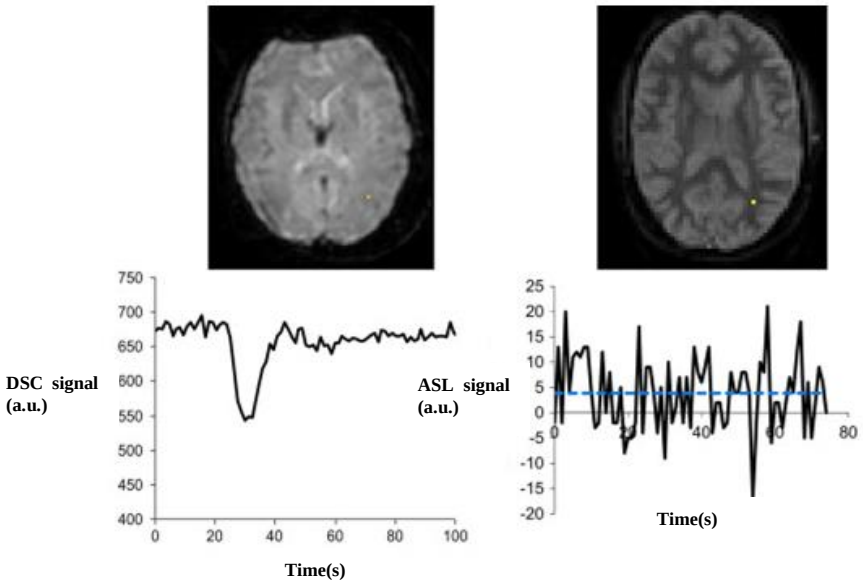

Figure 3.1: Perfusion EPI. a) DSC. b) ASL. The plots in the bottom row show data for a typical volume of interest (VOI), in WM. Adapted from [4].

3.3.1 Dynamic Susceptibility Contrast (DSC)

Currently, DSC is the most commonly used MRI method to measure perfusion in cerebral ischemia and brain tumors. It relies on the intravenous injection of a paramagnetic CA (e.g. Gd-DTPA) and rapid measurement of the transient signal changes during the passage of the bolus through the brain. This technique uses fast imaging (e.g. EPI-based) to capture the first-pass of the CA, known as *Bolus Tracking*. After the injection of the CA, the hemodynamic signal of DSC will depend on the T_2 or T_2* relaxation times and transiently decreases because of the increasing susceptibility effect [2, 3].

In DSC-MRI, as the CA passes in high concentration through the microvasculature, susceptibility-induced T_2 and T_2* relaxation occurs in surrounding tissues, resulting in a decrease of signal intensity, figure 3.1a. This decrease of signal intensity is assumed to be linearly related to the concentration of the CA in the microvasculature. The change in the signal intensity of the tissues is quantitatively related to the local concentration of CA and is converted into a CTC, figure 3.2. Therefore, by applying a tracer kinetics to CTC on the first-passage of CA through the capillary bed, parameters related to haemodynamic perfusion such as *Cerebral Blood Flow*

(CBF), *Cerebral Blood Volume* (CBV), *Mean Transit Time* (MTT) and *Time to Peak* (TTP) can be estimated [2, 3]. On the next subsection, these parameters will be defined.

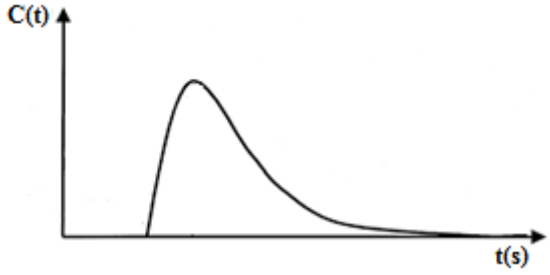

Figure 3.2: CTC curve.

3.3.2 Arterial Spin Labeling (ASL) and Dynamic Contrast Enhanced (DCE)

ASL is an alternative method to measure perfusion of tissue achieved by magnetically labeling the incoming blood, being contrast free. This technique is non-invasive because it uses arterial water as an endogenous diffusible tracer and so no injected CA or ionizing radiation is used. ASL requires the subtraction of two images, one in which the incoming blood has been labeled and the other in which no labeling has occurred [4].

Comparing DSC and ASL, DSC was advantageous since the calculation of some hemodynamic parameters (e.g. CBV and CBF) are underestimated in regions with delayed arrival when the ASL method is used and also the SNR of DSC data is higher than ASL data, figure 3.1b. Nevertheless, because both DSC and ASL are not able to evaluate the vascular permeability, a new dynamic contrast method can be introduced, named *Dynamic Contrast Enhanced* imaging (DCE).

DCE imaging refers to acquisition and analysis of MRI data that describes the uptake of an intravenous CA in a ROI. In short, one image series is acquired without contrast enhancement (baseline images) followed by a series of images acquired over time after an intravenous bolus of conventional CA. Quantitative physiological parameters are extracted by examining the signal changes relative to baseline in both tissue and large arteries [99]. Therefore, temporal changes in contrast-enhancement effectively provide a CTC, which can be analysed to quantify a range of physiological parameters such as: *Volume Transfer Constant* (K_{trans}) and *Extravascular Extracellular Space Volume* (v_e). These parameters provide information about the functional status of the vascular system within tumors and adjacent tissues. DCE depends on T_1 relaxation time and DCE signal increases due to T_1 shortening effect associated to the paramagnetic CA [99]. However, as some pulse sequences intentionally reduce T_1sensitivity, DCE technique is mainly used in brain studies.

3.3 State of the Art

3.3.1 Methods

3.3.1.1 Single-echo GE and SE EPI for Perfusion Quantification

As reported in [2] single-shot GE and SE EPI can be used to get dynamic information. In order to analyse DSC-MRI inherent parameters after data acquisition, a CTC has to be computed. Therefore, it is necessary to obtain an accurate estimate of the baseline MR signal intensity $S(0)$ prior to the arrival of CA.

3.3.1.1.2 Quantification of the Susceptibility T_2* Contrast

For single-shot GE EPI sequences, the MR signal (S), as a function of the contrast concentration C, can be approximated by:

$$S(C) = M_0 \frac{\sin(\alpha)\left[1-e^{-T_R \times R_1(C)}\right]}{(1-\cos(\alpha))e^{-T_R \times R_1(C)}} \cdot e^{-T_E \times {R_2}^*(C)} \leftrightarrow S(C) = M_0 \times E_1(C) \times e^{-T_E \times {R_2}^*(C)} \quad (3.1)$$

, where R_1 is the (contrast concentration-dependent) relaxation rate $1/T_1$, ${R_2}^*$ is the (contrast concentration-dependent) relaxation rate $1/{T_2}^*$, α is the flip-angle, T_R is the repetition time, T_E is the echo time, M_0 is proportional to the equilibrium magnetisation and E_1 is the term containing T_1 effects.

From equation 3.1, it is possible to calculate the susceptibility-induced signal drop for GE:

$$\Delta {R_{2GE}}^* = {R_{2GE}}^*(C) - {R_{2GE}}^*(0) = \frac{1}{T_E}\left[\ln\left(\frac{S(0)}{S(C)}\right) + \ln\left(\frac{E_1(0)}{E_1(C)}\right)\right] \quad (3.2)$$

The second term of the equation describing the T_1 effects is assumed to be negligible compared with the much stronger ${T_2}^*$ effects and thus is ignored.

Therefore, if T_1 effects are small in the tissue, for single-echo GE EPI sequences, CTC can be approximated from a simplified by:

$$\Delta R_{2GE^*_{app}} = \frac{1}{T_E}\left[\ln\left(\frac{S(0)}{S(C)}\right)\right] \quad (3.3)$$

, where $\Delta R_{2GE^*_{app}}$ is the measured apparent change in ${T_2}^*$ relaxation rate caused by the CA.

3.3.1.1.3 Quantification of the Susceptibility T_2 Contrast

In contrast with GE, the SE sequence is dependent of T_2. Therefore, T_2 quantification will follow the procedure described above but with a different scale factor. For single-echo SE sequence the susceptibility-induced signal is given by:

$$\Delta R_{2SE} = R_{2SE}(C) - R_{2SE}(0) = \frac{1}{T_E}\left[\ln\left(\frac{S(0)}{S(C)}\right) + \ln\left(\frac{E_1(0)}{E_1(C)}\right)\right] \quad (3.4)$$

For the same reason can be simplifies as:

$$\Delta R_{2SE_{app}} = \frac{1}{T_E}\left[\ln\left(\frac{S(0)}{S(C)}\right)\right] \quad (3.5)$$

, where $\Delta R_{2SE_{app}}$ is the measured apparent change in T_2 relaxation rate caused by the CA.

3.3.1.1.4 Cerebral Blood Flow (CBF)

CBF is one of the PW parameters, which characterizes both brain physiology and function. CBF evaluates the blood's ability to perfuse brain tissue adequately in a given time period, representing the instantaneous capillary flow in tissue. CBF is measured in units of mL/min/100g [5]. CBF can be estimated computing the equation 3.6.

$$C(t) = CBF.\,R(t) \otimes AIF\,(t) \quad (3.6)$$

, where $R(t)$ reflects both the tissue perfusion and the macrovascular transport effects of delay and dispersion, AIF (t) the *Arterial Input Function* and $\otimes$ the convolution process. AIF can be obtained from the mean curve of the CTC that correspond to arterial pixels.

Finding the solution of the maximum of $CBF.\,R(t)$, CBF can be estimated. Therefore, equation 3.6 can be solved by applying the convolution theorem:

$$CBF.\,R(t) = FT^{-1}\left[\frac{FT(C(t))}{FT[AIF(t)]}\right] \quad (3.7) \qquad CBF = \max[CBF.\,R(t)] \quad (3.8)$$

, where FT^{-1} is an inverse of FT.

3.3.1.1.5 The Correction Factor (K_H)

The *Correction Factor* (K_H) accounts for the higher proportion of red blood cells (H_{ct}) in arterial blood compared with capillary blood. As reported on the literature [2], K_H is used when an absolute quantification is required. Thereby, hemodynamic parameters have to scale by this

correction factor. As the CA can only distribute in the plasma portion of the blood ($1 - H_{ct}$), the amount of plasma affects the susceptibility-induced relaxation. K_H is often set to 0.733.

$$K_H = \frac{1-Hct_{artery}}{1-Hct_{capillary}} \qquad (3.8)$$

3.3.1.1.6 Cerebral Blood Volume (CBV)

CBV is defined as the volume of blood in a given amount of brain tissue. This parameter measures the microvascular blood volume, which is proportional to the total amount of intravascular CA in the tissue. CBV can be determine from the area under the CTC:

$$CBV = \int_0^\infty R(t)dt \qquad (3.9)$$

In order to obtain the correct units CBV should be scale by K_H and be normalised by density of brain tissue (ρ) ($K_H|\rho$), which in practice is set to mL/100 g.

3.6.1.1.7 Mean Transit Time (MTT) and Time to Peak (TTP)

MTT is a measure of the main time for blood or CA to perfuse a region of tissue [99]. As referred in [2, 99], MTT is calculated using the central volume principle[9], equation 3.10. MTT is measures in units of s.

$$MTT = \frac{CBV}{CBF} \qquad (3.10)$$

TTP reflects the time from the beginning of the CA injection to the peak enhancement within a ROI. TTP is inversely related to CBF in which reduction of blood flow results in an increase in the time needed for the contrast to reach its peak in the perfused volume of brain tissue [3, 4]. TTP is measured in units of seconds (s).

3.3.1.2 Double -Echo

The problems associated with standard single-echo in dynamic acquisitions arise from the assumption that changes in the measured signal intensity only reflect changes in $T_2{}^*$relaxation times associated with CA. However, this assumption is valid in healthy tissues but not in pathologies, which are characterized by a BBB disruption. When BBB is disrupted, CA will be accumulated in the surrounding tissue affecting both $T_2{}^*$and T_1 relaxation times. Herein, CA leakage breaks down the assumed relationship between measured signal intensity and underlying CA concentration because signal changes can not be assumed to be dominated by changes in $T_2{}^*$.

[9] From CBV = CBF x MTT

This broken assumption means that single-echo DSC-MRI lacking T_1 leakage correction yields unreliable estimates of tissue perfusion whereby, T_1 must be corrected. Two different methodologies were proposed to minimize T_1 effects. One refers to the injection of a small pre-bolus, which reduces the leakage effects and the other one to the implementation a multi-echo technique, which is insensitive to the T_1 effects of CA extravasion [4-6]. In the multi-echo technique, the images acquired ate each T_E can be used to correct the T_1 effects.

Dual-Echo GE was introduced by Kuperman et al. in 1996 [100] and Miyati et al in 1997 [101].

Following the steps defined above, the susceptibility-induced signal drop for dual-echo can be rewritten for GE sequences by:

$$\Delta R_{2GE}{}^{*} = R_{2GE}{}^{*}(C) - R_{2GE}{}^{*}(0) = \frac{1}{T_{E_2} - T_{E_1}} \left(\ln \left[\frac{ST_{E_1}(C)}{ST_{E_2}(C)} \right] - \ln \left[\frac{ST_{E_1}(0)}{ST_{E_2}(0)} \right] \right) \quad (3.11)$$

, where T_{E_1} and T_{E_2} are the first and second echo time (T_E). Following, CTC is calculated by:

$$C(t) = \frac{1}{r_{tissue}(T_{E_2} - T_{E_1})} \left(\ln \left[\frac{ST_{E_1}(t)}{ST_{E_2}(t)} \right] - \ln \left[\frac{ST_{E_1}(0)}{ST_{E_2}(0)} \right] \right) \quad (3.12)$$

, where r_{tissue} is the CA $T_2{}^{*}$ relaxivity for GE.

3.3.1.3 Combination of GE SE EPI – The Image Contrast

As reported by several studies, DSC can be acquired using either SE or GE EPI sequences, which provide different contrasts [3, 16]. The CA induced susceptibility gradients in the tissue promotes proton dephasing because of static field inhomogeneities and diffusional motion.

SE acquisitions refocus the dephasing caused by the static field inhomogeneities producing T_2-weighted images. These images are only sensitive to the diffusion of the tissue water protons through the inhomogeneities. Therefore, SE DSC signal drop is largest in the vicinity of capillaries, where the phase accumulation across the diffusion distance is greatest. Consequently, SE DSC images are sensitive to the microvasculature.

In contrast, GE acquisitions do not refocus static field inhomogeneities and are sensitive to changes in $T_2{}^{*}$. Susceptibility-induced signal drops is higher in GE than in SE acquisitions across all vessels size. Thereby, GE results to be more sensitive to the macrovasculature. As GE is more sensitivity weighted towards the microvasculature, the derived perfusion maps are dominated by the macrovasculature signal (which is not tissue perfusion). Consequently, they may not detect compromised microvasculature [102].

Comparing both techniques, a higher dose of CA is required for a SE acquisition to achieve the same SNR as a GE acquisition. This can be explained due the T_E of SE sequence being longer than GE sequence. The GE EPI sequences have the advantage of being acquired more rapidly, allowing higher temporal resolution, compared with the SE EPI for the same number of slices/resolution. Thereby, for brain studies GE EPI is more commonly used due to its higher SNR, lower contrast dose requirement and the ability to quantify the contrast concentration

in artery and tissue. Further, using multi-echo GE, T_1 effects can be corrected, which is important in dynamic imaging [103].

Notwithstanding, the combination of SE and GE (GESE) sequences with EPI has recently been developed emerging the possibility of combining both advantages in one acquisition [3, 102]. In one way, it is possible to simultaneously quantify $\Delta R_{2GE}{}^{*}$ and ΔR_{2SE}. In other way, higher specificity to the microvasculature of SE EPI with the ability to measure the macrovasculature from GE EPI can be obtained in the same image. Figure 3.3 illustrates the DSC-MRI contrast achieved with GESE EPI acquisition for five T_E.

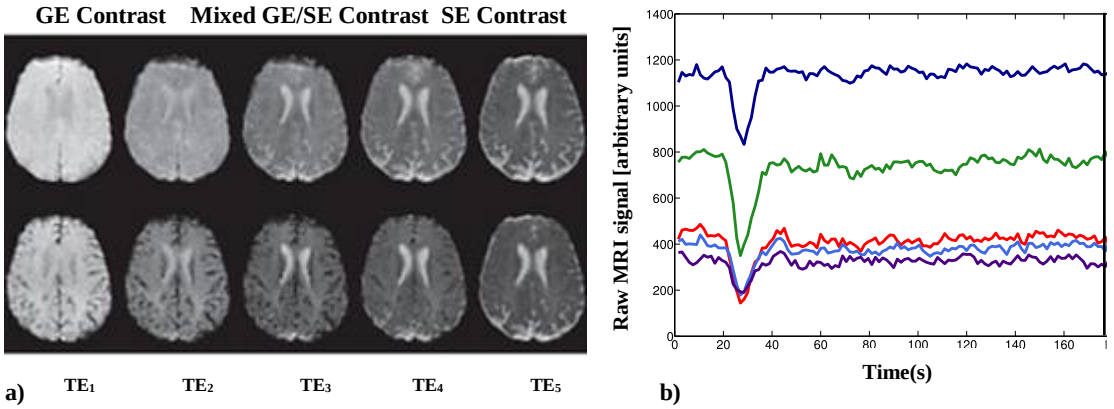

Figure 3.3: Multi-echo GESE EPI perfusion. a) EPI images in a selected patient acquired during baseline (top row) and at the peak of the bolus passage (bottom row). b) MRI signal time course of each EPI train in a specified voxel within GM. The dark blue color corresponds to T_{E_1}, the green to T_{E_2}, the red to T_{E_3} the light blue to T_{E_4} and the purple to T_{E_5}. Adapted from [102].

3.3.1.4 Cerebrovascular Network

The *Cerebrovascular Network* can be described based on the theory of susceptibility-induced MRI signal dephasing in a cerebrovascular network. This model adapts the model for multiple vessel generations to introduce the kinetics of the bolus passage through the micro and macrovasculature [16, 104].

The cerebrovascular network comprises both micro and macrovasculature types of vessels. From the microvasculature it is possible to distinguish arteries, capillaries and veins and from the macrovasculature arterioles and venues [16]. Arterioles/venules are formed by the branching of pial vessels, which enter into the tissue perpendicular to the cortical surface and transverse to cortical depth. Branching from the penetrating arterioles, a capillary network is formed, thinner compared with arteriole (diameter < 10 μm). From inside of the capillaries, O_2, glucose and nutrients diffuse out of the vascular network and into the tissue. Metabolic waste products (e.g. carbon dioxide) also diffuse from the tissue into the vasculature. Therefore, capillaries intersect with the venular network and the penetrating venules transport deoxygenated[10] blood to the cortical surface. In this manner, this network is modelled by a tree structure with symmetric arterial and venous parts, figure 3.4 [16]. This organized network enables the efficient delivery of O_2 and glucose to brain cells, which is essential since brain cells do not naturally store or produce these molecules. Therefore, the cerebrovascular network

[10] Without oxygen

explains micro and macrovasculature structures and introduces the importance of vessel size quantification

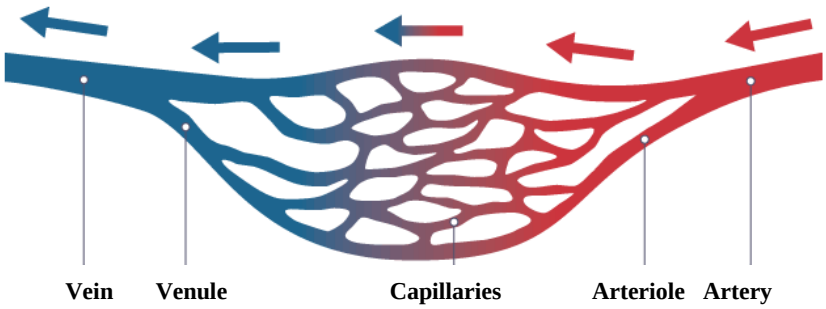

Figure 3.4: Cerebrovascular network. Arterial system corresponds to red and venous system to blue. Adapted from [105].

3.3.1.5 Vessel Size Imaging

In 1991, Fisel, Rosel and colleagues pioneered the theoretical foundation for vessel caliber MRI technique [25, 96]. In a series of studies, these researchers using Monte Carlo simulations concluded that T_2-weighted perfusion MR images were sensitive to the vessel size due to the magnetic susceptibility effect created by blood and CA flowing through the vessels. Motivated by these findings VSI was introduced. VSI is a new MR technique achieved by measuring the changes of ΔR_{2SE} (tranverse relaxation rate and $\Delta R_{2GE}{}^{*}$ caused by the injection of a paramagnetic CA [16]. The ΔR_{2SE} is sensitive towards the microvasculature and the $\Delta R_{2GE}{}^{*}$ shows higher specificity to the macrovasculature. From VSI, several parameters were proposed, named *Mean Vessel Diameter* (mVD), *Mean Vessel Density* (Q), *Vessel Size Index* (Vsi) and *Vessel Architectural Imaging* (VAI) and will be explained in detail in this section [12, 13, 16].

3.3.1.5.1 Mean Vessel Diameter (mVD)

In 1998, Dennie et al. [20] proposed the dimensionless parameter mVD, which provides an indication of the average vessel size within a voxel. This parameter depends on the average vessel size and on the CA concentration. mVD is calculated based on the ratio between the integrals of $\Delta R_{2GE}{}^{*}$and ΔR_{2SE}, equation 3.13.

$$mVD = \frac{\int \Delta R_{2GE}{}^{*}(t)dt}{\int \Delta R_{2SE}(t)dt} \qquad (3.13)$$

This equation is valid when there is a high CA dose with a T_E dependence on ΔR_{2SE} and a small coefficient of variation of the vessel size distribution [20].

3.3.1.5.2 Mean Vessel Density (Q)

Two years later, in 2000 Jensen and Chandra [19] introduced Q. Q is the parameter sensitive to the microvessel density and calculated based on ratio between the integrals $\Delta R_{2GE}{}^{*}$and ΔR_{2SE}.

$$Q = \frac{\int \Delta R_{2SE}(t)dt}{\int (\Delta R_{2GE}{}^{*})^{2/3}(t)\,dt} \qquad (3.14)$$

The ratio $\left(\frac{\Delta R_{2GE}{}^{*}}{\Delta R_{2GE}{}^{*2/3}}\right)$ is obtained by fitting the linear dependence between $\Delta R_{2GE}{}^{*}$and ΔR_{2SE}. Q is independent of the CA concentration, depending only on intrinsic tissue properties and highly dependent on T_E. Thereby, the appropriate T_E has to be selected to get an accurate measurement, CA concentration has to be sufficiently high ($\Delta\chi \gg \chi_0$) and the normalized CBV small enough (CBV << 1) for Q to be sensitive to the histologic vessel density. $\Delta\chi$ is defined as the magnetic susceptibility difference between the intra and extravascular compartments induced by the presence of a CA in the vasculature and χ_0 the blood susceptibility without the CA.

If histology of vessel brain tissue is available (based on biopsy information), equation 3.14 can be rewritten in terms of the histologic vessel density as:

$$Q = 1.678.k.(D.N)^{1/3} \qquad (3.15)$$

, where k is a dimensionless parameter dependent on the radius of the vessel always less or equal to one and depends on the distribution of the vessel radii, N is the microvessel density and D the diffusion coefficient of water in tissue (D ~1.0 $\mu m^2/ms$). k can also be calculated as given by:

$$k = \frac{\langle R^{4/3}\rangle}{\langle R^2\rangle^{2/3}} \qquad (3.16)$$

, with R being the vessel radius and the angle brackets indicating an average over the vascular network.

Nevertheless, it is not possible to quantify directly the mean vessel diameter by estimating Q based on histological information due to the lack of intra-subject of histological data. Regardless, Q can be quantified using mVD PW information [20].

3.3.1.5.3 Vessel Size Index (Vsi)

In 2001, Tropes et al. [21] presented Vsi, which gives information about the vessel caliber. Vsi can be computed using the following equation:

$$Vsi = \left(\frac{\int \Delta R_{2GE}{}^{*}(t)dt}{\int \Delta R_{2SE}(t)dt}\right)^{3/2} \qquad (3.17)$$

However, for the application in human studies Vsi has to include the measurements of the *Apparent Diffusion Coefficient* (ADC) in $\mu m^2/s$, $\Delta\chi$, the magnetic field (B_0) and the gyromagnetic ratio γ in $rad.s^{-1}.T^{-1}$. Therefore, equation 3.17 can be rewritten as:

$$Vsi = 0.424\left(\frac{ADC}{\gamma.\Delta\chi.B_0}\right)^{1/2}.\left(\frac{\int \Delta R_{2GE}{}^{*}(t)dt}{\int \Delta R_{2SE}{}^{3/2}(t)\,dt}\right) \qquad (3.18)$$

This equation is valid for small CBV (<< 1) and large echo times (T_E >>1/ ($2\pi.\gamma.\Delta\chi.B_0$)).

As well as in Q estimation, the ratio of $\left(\frac{\Delta R_{2GE}{}^{*}}{\Delta R_{2SE}{}^{3/2}}\right)$ is obtained by fitting the linear dependence between $\Delta R_{2GE}{}^{*}$and ΔR_{2SE} during the first-pass of the CA.

3.3.1.5.4 Apparent Diffusion Coefficient (ADC)

Apparent Diffusion Coefficient (ADC) describes microscopic water diffusion in the presence of some factors (e.g. membranes or viscosity) that restricts this diffusion within tissues. ADC can be derived on a voxel-by-voxel in specific region. For a given direction, ADC is calculated on a pixel-by-pixel basis by fitting signal intensities to the *Stejskal-Tanner* using a least –squares method, equation 3.19:

$$S(b) = S(0)\,e^{-b.ADC} \qquad (3.19)$$

, where S(b) represents the signal after the diffusion gradients have been applied, S(0) the MR signal at baseline and b corresponds to the b-value. The b-value is a factor that reflects the strength and timing of the gradients used to generate DW images.

ADC correlates with tumors cell density whereby, different tumor malignancies corresponds to different values of ADC [106].

3.3.1.5.5 Relations between different parameters

The relation between Vsi and mVD is deduced by replacing the ratio $\frac{\Delta R_{2GE}{}^{*}}{\Delta R_{2SE}}$ in equation 3.18.

$$Vsi = 0.424\left(\frac{ADC}{\gamma.\Delta\chi.B_0}\right)^{1/2}.(mVD)^{3/2} \qquad (3.20)$$

Considering B_0 equal to 3T and a single bolus injection of Gd-DTPA the relation between Vsi and Q can also be derived:

$$Vsi = 0.867(ADC.CBV)^{1/2}.(Q)^{-3/2} \qquad (3.21)$$

The CBV was calculated as the area under the curve of $\Delta R_{2GE}{}^{*}$ and normalized to 3% in the normal apparent white matter.

3.3.1.5.6 Vessel Architecture Imaging (VAI)

Vessel Architecture Imaging (VAI) has been introduced as a new concept on vessel caliber MRI. VAI methodology was first proposed by Kiselev et al. in 2005 [18] from the high sensitivity of the macrovessel MRI signal information found for deoxygenated capillary and venous blood volume. In VAI procedure, both relaxation curves ($\Delta R_{2GE}{}^{*}$ and ΔR_{2SE}) are combined and two different steps can be performed to assess vascular information. Both methodologies are complementary.

In the first step, $\Delta R_{2GE}{}^{*}$ and ΔR_{2SE} curves are combined in a scatter plot resulting in a referred vessel vortex curve, illustrated in figure 3.5. The vessel vortex direction of the curve is defined by what direction the point-by-point scatter plot propagates (clockwise or counter-clockwise). The long axis of the vessel vortex curve (the nº 1) is found by a linear fit and an increase in the long axis is equivalent to an increase in the area under the relaxation rate curve, which is the traditional measure of CBV (the nº 2). The short axis of the vessel vortex (the nº 3) is the maximum length of a straight line perpendicular to the long axis. Finally, the slope value is the gradient of the long axis and describes its steepness (the nº 4).

In the second step, the TTP of both $\Delta R_{2GE}{}^{*}$ and ΔR_{2SE} curves are compared (figure 3.6a and figure 3.6c) and from the analyses of the time shift between the curves, information about the type of vessels can be obtained.

Thereby, from the combination of the information provided from both steps, in areas with a fast inflow of CA, GE signal peaks earlier than SE signal and the voxel curve transverse in a clockwise direction, figure 3.6b. The vascular system consists of arterioles and capillaries only or, for some geometrical, pathological or physiological reason, fast-inflow arterioles with larger calibers than venules. On the other way around, the curve transverse in counter-clockwise direction and the vascular system contains both slow-inflow, larger caliber venule-like vessel components and faster-inflow, smaller caliber arteriole-like or capillary-like vessel components, figure 3.6d. Further, if the differences between the TTP of both GE and SE signal are small, the voxel curve transverse in a counter-clockwise direction corresponding to the cappilares. However, if all vessels have identical caliber and SO_2 concentration or if a vascular system with a fixed SO_2 concentration contains arterioles, capillaries or venular structures only, even with different radii, there is no vortex.

Hereupon, VAI methodology reveal information about the vessel types present (arteries, capillaries and veins), as well as the relative difference in radii and oxygen saturation levels between this vessel. Thereby, from VAI, further information about tumor heterogeneity can be obtained, which is not possible to be assessed using other techniques [17, 18]. Moreover, it is important to take into account that, under normal conditions, venues caliber is bigger than arteriole caliber [17].

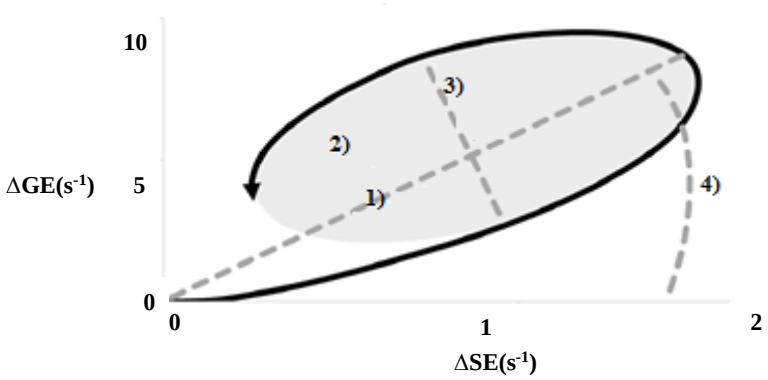

Figure 3.5: Vessel vortex curve from GE SE pairwise relaxation curves. Adapted from [12].

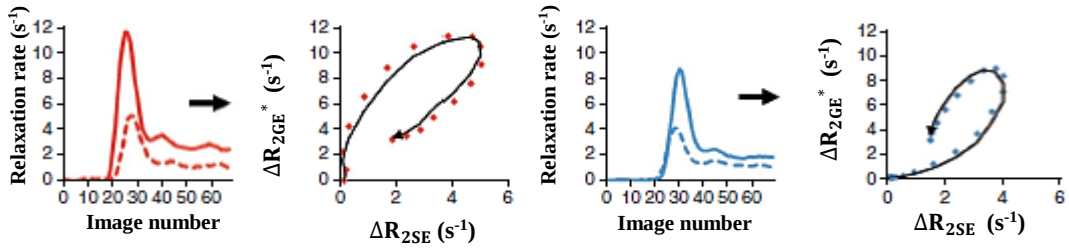

Figure 3.6: Relaxation curves and respective direction of the voxel curve. a) ΔR_{2SE} and ΔR_{2GE}^{*}. b) Clockwise vessel vortex curve. c) ΔR_{2SE} and ΔR_{2GE}^{*}. d) Counter-clockwise vessel vortex curve. On figure a, SE signal peaks earlier than the GE signal resulting in a counter-clockwise vortex (figure d). On figure c, GE signal peaks earlier than the SE signal resulting in a clockwise vortex (figure b). Adapted from [12].

3.3.1.5.7 Standard Perfusion Parameters and Vessel Size Imaging

As stated before, it is defined that GE contrast is sensitive to vessel of all sizes (micro and macrovasculature) in contrast with SE contrast, which is weighted toward microvascular structure [22]. Therefore, VSI methodology provides an insight into the properties of microvasculature that are often shielded in the GE perfusion measurements dominated by larger vessels. Unlike VSI, PW parameters such as CBV and CBF are presented as a relative values and MTT is influenced by the injection condition of CA. Among VSI parameters, Vsi is a quantitative parameter, it enables a comparison in inter-subject and longitudinal studies, which is advantageous. However, the dependence of CBV in Vsi may be taken into account (equation 3.21). When the mVD remains unchanged, the Vsi map has a similar appearance to the relative CBV contrast.

Based in the presented methodology, VSI can be used to monitor vasculature changes in different gliomas grades [13, 21]. Vessel caliber parameters can be studied separately or together for complementary information about the microvascular network.

3.3.2 Studies

3.3.2.1 Vessel Size Imaging

3.3.2.1.1 Clinical Studies for Small Animal

Several pre-clinical studies have been performed in order to determine the value of MRI based vessel caliber. Comparisons between VSI and histological data have been performed in order to validate the feasibility of VSI.

Pre-clinical animal studies have shown excellent agreement between MRI and histological vessel calibers in orthotopic glioma xenograft model[11] [20, 21, 23, 107]. However, absolute average of determined vessel calibers tends to be slight overestimate compared with histological vessel caliber measurements. This fact was explained due of the incomplete understanding of the relationship between blood MRI signal and the underlying physiology. Collectively, these studies provide first corroborating evidence that determination of vessel calibers can serve as a surrogate marker of the microvasculature in tumors motivating its implementation in human's studies. Only studies without any administrated treatment were mentioned.

3.3.2.1.2 Vessel Size Index (Vsi) - Human Studies

Following the substantial increase of pre-clinical studies about vessel caliber MRI over the past decade, the number of clinical studies related in human cancer, stroke and hypercapnia also increased. Only the studies with cancer data will be mentioned.

The first human vessel caliber MRI data in cancer was measured in intracranial tumors. In 2000, Donahue and co-workers published the first images [108]. Four years later, using the same methodology, Schmainda et al. confirmed the previous results in a corroborating study that included 72 patients with gliomas. This study demonstrated larger relative vessel calibers and a wider range of calibers with increasing tumor grade [109]. These findings have been confirmed in small glioma studies by Lamalle et al. [110] and by Hsu et al. [111]. Larger vessel calibers and greater heterogeneity in vessel diameters were found in glioblastomas compared with LGG. In parallel, Kiselev, Breyer, Xu and their colleagues [112,113] also presented supporting data from patients with brain lesions across several publications between 2003 to 2013. Higher average MRI vessel calibers were reported in 20 intracerebral tumors (84 ± 73 μm) compared with adjacent WM (32 ± 10 μm) and GM (34 ± 8 μm) tissue [112]. These findings have also been confirmed in 31 patients at 3T, as opposed to 1.5T scanner by Breyer et al. [113]. More recently in 2015, Kellner et al. [114] provided a comparative study between Vsi and CBV in patients with glioma with data from histopathology. Using 25 gliomas within different grades, this study demonstrated a good correlation between Vsi and vessel size from histology. Also, similar results between CBV and Vsi using perfusion were found. Furthermore, in 2016 Kang et al. [115] compared the efficacy of distinguishing gliomas grades using CBV and Vsi parameters. In this study, participated 70

[11] Xenograft is a transplantation model, which involves actual human cancer cells or solid tumors, which are transplanted into a host mouse. The transplant may be orthotopic meaning that the tumor is placed in the site it would be expected to arise naturally in the host.

patients and microvessel parameters were compared with histology information. The conclusions of this study demonstrated that Vsi is more efficient than CBV (i.e. higher specificity and sensitivity) when distinguishing HGG and LGG.

Further studies were performed in order to investigate the feasibility of target therapies using Vsi information. Prior to administration of targeted therapies, abnormal and dilated vessel calibers were observed using MRI in a range of glioma grades [116], recurrent glioblastomas [103, 117] and newly diagnosed glioblastomas [119]. An almost threefold increase in average tumor vessel calibers compared with whole brain of normal-appearing tissue was observed in 30 patients with recurrent glioblastomas (21 ± 6 μm versus 8 ± 1 μm) [12] and in two separate cohorts comprising 40 and 14 patients with newly diagnosed, untreated glioblastomas (24 ± 15 μm versus 8 ± 2 μm and 33 ± 20 μm versus 11 ± 5 μm, respectively). However, in these studies the obtained CBV were lower than reported by Kiselev et al. [13].

3.3.2.1.3 Mean Vessel Diameter (mVD) and Mean Vessel Density (Q) Studies

In 1998, Dennie et al. introduced the first vessel caliber parameter, named mVD [20]. This parameter provides an indication of the average vessel size within a voxel but does not give information about the density of the vessels. Therefore, two years later Jensen and Chandra [21] introduced a dimensionless parameter Q, sensitive to the microvessel density. In this first study, relaxation rate changes were computed using a static technique (Steady-State Contrast-Enhanced (ssCE-MRI)). Although in 2006, the same author published a quantitative Q assessment in human brain tissue using an interleaved dynamic sequence (SE GE EPI) and a bolus injection of Gd-DTPA [22]. The conclusions of this study demonstrated that DSC EPI can be used to evaluate Q within the human brain. Also, the obtained Q values were in accordance with histology information. From this conclusions, Q is a potentially parameter for vessel density information assessment in human brain tumors. Further studies were also performed to provide more information about this parameter [8, 120, 121].

3.3.2.2 ^{18}F-FET -PET Studies

Several studies have been performed in order to access the feasibility of amino acid tracer ^{18}F-FET PET in brain tumor diagnosis. In 2006, Pöpperl et al. [8] evaluated the feasibility of ^{18}F-FET uptake kinetics in 45 patients with gliomas comparing with histopathologic findings from biopsies. This study demonstrated that ^{18}F-FET uptake was able to differentiate between LGG and HGG. One year later, the same author evaluated the potential of ^{18}F-FET for non-invasive tumor grading in 54 untreated patients. Significant differences were found between LGG and HGG. In 2015, Galldiks et al. [9] evaluated the diagnostic value of static and dynamic ^{18}F-FET PET parameters in patients with progressive and recurrent glioma. This study concluded that static and dynamic ^{18}F-FET parameters differentiate progressive or recurrent glioma from treatment-related non-neoplastic changes with higher accuracy than conventional MRI techniques. Furthermore, comparative PET tracer studies have also been performed in order to verify the feasibility of ^{18}F-FET PET in tumor diagnosis. In 2014, Pauleit et al. [96] investigated the diagnostic value of ^{18}F-FDG and ^{18}F-FET in 52 patients with cerebral gliomas concluding that ^{18}F –FET is superior for biopsy guidance and treatment planning. More recently, in 2016 Dunet et al. analysed the performance of ^{18}F-FET versus ^{18}F-FDG PET for diagnosis efficiency and grading of brain tumor [10]. It was concluded that for brain tumor diagnosis ^{18}F-FET performed much

better than ^{18}F- FDG (higher sensitivity and specificity). In conclusion, among amino acid tracers, ^{18}F-FET should be preferred for tumor brain grading and delineation.

3.3.2.2 3 MR/PET Studies

Ostergarrd et al. in 1998 [122] was the first author to combine information from perfusion MR data and amino acid PET data. In his study, the calculation of CBF using MRI bolus tracking data was compared with (^{15}O) water uptake using PET. This study yielded parametric CBF images with tissue contrast in good agreement with parametric CBF PET images. Nonetheless, several factors needed to be correct as, the duration the measurement, anatomic precision, image resolution and sensitivity to tracer arrival delays. Motivated from previous studies, in 2005 Pauleit et al. investigated whether the diagnostic accuracy of MRI could be improved by the additional use of amino acid ^{18}F-FET PET [95]. This study concluded that combined information from MRI and ^{18}F-FET -PET in patients with cerebral gliomas significantly improves the identification of cellular glioma tissue and exploits histological tumor diagnosis.

Furthermore, related to dynamic studies several ones suggested that PWI-MR imaging, particularly regional cerebral blood volume maps (rCBV)[12], may provide similar diagnostic information comparing to ^{18}F-FET data [12, 123]. Nevertheless, in 2014 Filss et al. performed a comparison between both techniques concluding that in patients with cerebral glioma, ^{18}F-FET and rCBV yields different information [12]. ^{18}F-FET PET shows considerably higher TBRs and larger tumor volumes than rCBV maps. Also, different local hot spots (i.e. maximum of tumor value) could be identified. In this manner and in contrast to previous studies [11, 123], amino acid PET information did not reflect rCBV PWI information and CBV showed a considerably lower diagnostic value in depicting metabolic active tumor tissue. Following this conclusion, in 2015 Henriksen et al. performed a similar study concluding that tumor volumes using PWI-MRI and ^{18}FET PET were quantitatively correlated but its spatial congruence was generally poor [13].
As both techniques give different information, one cannot replace the other, so its combination can be potentially improving tumor diagnosis and glioma grading.

[12] rCBV corresponds to the CBV calculated in the specific region of the brain.

4. Materials and Methods

The main focus of this dissertation is to compare ^{18}F-FET PET with Vsi, CBV, Q and VAI information and to evaluate the performance of Vsi, CBV, Q and VAI in providing vascular information. In this chapter, the reader is presented with the materials and methods used throughout this study in order to accomplish the dissertation's objective. A brief description of the data used, the equipment and acquisition schemes will be mentioned and the image processing methodology will be described.

4.1 Dataset and Acquisition

4.1.1 Patient

Twenty-five patients (eight female and seventeen males) with brain tumors diagnosed based in histological information (Twenty high-grade gliomas, two low-grade gliomas, one suspected of metastasis and 2 gliomas no further specified) were recruited for this study. Further information about patients can be found in table A.1, *Annexe 1*. Tumors were graded according to the guidelines suggested by the *World Health Organization* (WHO) [124]. Glioma grades I and II were defined as low-grade ones and grades III and IV as high-grade. Patients were also selected according to their ability to cooperate and remain still during the scan. Informed consent was obtained from each patient after the study was comprehensively explained. The study protocol was approved by the local Human experiments and ethics committee.

4.1.2 Contrast Agent

For each subject, Gadoteric acid (Dotarem Guerbet) was injected with a dose of 0.1 mmol/Kg of body weight and 100 MRI image volumes were acquired in order to track dynamic signal changes induced by the CA. Injection was performed automatically with a power injector (Injektron 82 MRT Medtron AG) at a flow rate of 5 mL/s.

4.1.3 Scanner

The measurements were performed in a Siemens 3T hybrid MR/PET scanner (MAGNETOM Trio a Tim Trio System). The head coil consists of two separate coils, a birdcage transmit-receive coil and an 8 channel receive coil.

4.1.4 MRI Acquisition

PW images were acquired using the combined 5-echo GESE EPIK sequence described previously. A 90º pulse was applied and two echoes (T_{E_1} / T_{E_2} =12/30ms for FE1 or and T_{E_1}/T_{E_2}=11/27ms for FE2) were acquired followed by a refocusing pulse and three additional echoes were then acquired (T_{E_3}/T_{E_4} /T_{E_5}=53/71/88ms for FE1 or T_{E_3}/T_{E_4} /T_{E_5}=50/66/80ms for FE2). The last echo is a SE created by the refocusing pulse. In this work, T_R was fixed to 1500 ms and 16 slices were acquired with a matrix size of 96x96, iPAT = 2, partial Fourier = 6/8, ramp sampling and a FOV of 24 cm. FE1 and FE2 correspond to two different acquisitions from different studies, however as the differences between the T_E do not influence our methodology and the protocol was the same, both data were included in this study.

4.1.5 PET Acquisition

Simultaneously with MR measurements, using BrainPET insert, a ^{18}F-FET PET scan was carried out in the hybrid instrument. The amino acid ^{18}F-FET was produced and applied as described previously [9]. Dynamic PET studies were acquired up to 50 min after intravenous injection of 3 MBq of ^{18}F-FET /kg of body weight on the same day as MR imaging. PET data was reconstructed using OP-OSEM3D software with 4 subsets and 32 iterations. The images were normalized and corrected for attenuation, scatter, dead time and random events. The reconstructed images have an isotropic voxel size of 1.25x1.23x1.25 mm^3 with a matrix size of 256x256x153. Note that, the BrainPET is a head only high-resolution PET insert with an isotropic image resolution at the center of the scanner of 3 mm [86].

4.2 Post-Processing Data

The data was analyzed using MATLAB v.2015a (The MathWorks, Inc, USA) and FSL toolbox v.1.4 (FMRIB, UK.).

4.2.1 Data Fitting

The first-bolus of the ΔR_{2GE}^* and ΔR_{2SE} signal time courses from GESE EPIK were fitted to a *Gamma Variation Function* (GVF). The fitting was applied to eliminate the contamination of the tracer recirculation from the second-bolus passage, figure 4.1. A simplified methodology proposed by Madsen et al. [125] was further applied.

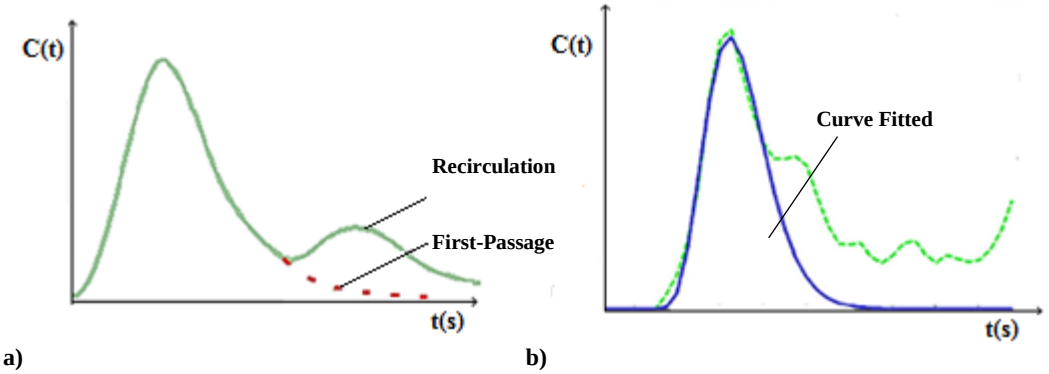

Figure 4.1: CTC. a) Conventional bolus curve. b) Bolus curve fitted using a GVF. In green it is represented the ΔR_{2SE} curve and in blue the ΔR_{2SE} curve fitted.

4.2.2 Gamma Fitting

The quantification of perfusion measurements using DSC-MRI depends on the estimation of the tracer bolus shape. Typically, the dispersion of a bolus, which passes through a series of compartments, can be described as a GVF, equation 4.1. GVF fits the bolus portion of tracer CTC [126].

$$y(t) = A(t - t_0)^{\alpha} e^{-(t-t_0)/\beta} \quad \text{, for } t>t_0 \qquad (4.1)$$

, where A is a scaling factor, α and β determine the bolus shape and t_0 is the bolus arrival time.

Using GVF it is possible to eliminate the contamination of tracer recirculation from the second-pass on the first-pass of DSC data, figure 4.1. Most authors assume that tracer recirculation has to be removed for an accurate estimation of perfusion parameters (e.g. CBV and CBF). The bolus fitting is therefore, an important step in perfusion studies [12, 16].

Thereby, both $\Delta R_{2GE}{}^{*}(t)$ and $\Delta R_{2SE}(t)$ curves can be rewritten as:

$$\Delta R_{2SE,GE}{}^{*}(t) = A(t - t_0)^{\alpha} e^{-(t-t_0)/\beta} \text{ , for } t>t_0 \qquad (4.2)$$

, where $\Delta R_{2SE,GE}{}^{*}$ represents the ideal first-pass curve from SE and GE sequence respectively.

4.2.2.1 Gamma Function Simplification

Madsen et al. [125] proposed a simplified formulation for GVF in order to provide an alternative to the non-linearity of the problem and reduce the number of estimated parameters. The simplification begins with the usual form described by equation 4.1. Because t_0 can be estimated easily, the origin of the graph can be shifted in such a way that it coincides with t_0. The function can be then expressed as:

$$y(t) = At^{\alpha} e^{-t/\beta} \text{ , for } t>t_0 \qquad (4.3)$$

This expression shows that β can be written in terms of α and t_{max} , where t_{max} is the time which $y(t)$ reaches its maximum. Taking the first derivative of equation 4.3 and setting it to zero will yield t_{max} in terms of α and β, or β in terms of t_{max} and α.

$$y'(t_{max}) = A{t_{max}}^{\alpha-1}e^{-t_{max}/\beta}\left(\alpha - \frac{t_{max}}{\beta}\right) \rightarrow t_{max} = \alpha.\beta \text{ or } \beta = \frac{t_{max}}{\alpha} \quad (4.4)$$

Substitution of β in equation 4.3 gives:

$$y_{max} = A{t_{max}}^{\alpha}e^{-\alpha t/t_{max}} \quad (4.5)$$

Subsequently letting $t=t_{max}$ will yield A in terms of y_{max}, t_{max} and α, equation 4.6:

$$y_{max} = y(t_{max}) = A{t_{max}}^{\alpha}e^{-\alpha t_{max}/t_{max}} \rightarrow A = y_{max}{t_{max}}^{\alpha}e^{\alpha} \quad (4.6)$$

Substituting these equations into equation 4.3 yields:

$$y(t) = y_{max}{t_{max}}^{-\alpha}e^{\alpha}t^{\alpha}e^{-\alpha t/t_{max}} \quad (4.7)$$

However, equation 4.7 can be further simplified by redefining the independent variable in terms of t_{max} with $t' = t/t_{max}$:

$$y(t') = y_{max}{t_{max}}^{-\alpha}e^{\alpha}{t_{max}}^{\alpha}t^{\alpha t'}e^{-\alpha t'} = y_{max}t'^{\alpha}e^{\alpha(1-t')} \quad (4.8)$$

From equation 4.8, y_{max} and α ca be found from the linear least-squares estimation. Taking into account that $\ln(t^{\alpha}) = \alpha.\ln(t)$, the following equation is obtained if the natural logarithm is taken:

$$\ln\big(y(t')\big) = \ln(y_{max}) + \alpha\,(1 + \ln(t') - t') \quad (4.9)$$

From this simplification, one less initial parameter has to be defined beforehand (β), the coupling between α and β has been eliminated and the computation time reduced. These results are important in brain studies due to increased number of pixels of the images.

4.2.2.2 Fitting Features

Data was fitted using MATLAB v.2015a using the *Levenberg-Marquardt* method implemented in *fmincon* function. The initial values for the fitting (α, A and t_{max}) were defined based on the whole brain CTC using a *Genetic Algorithm* (GA). GA allows to generate a population of points at each iteration and the best point in the population approaches an optimal solution. fitting . The methology applied using this method will be not described in this dissertation, for further information contact the author.

4.2.3 ADC Maps

The ADC maps were calculated on a pixel-by-pixel by fitting signal intensities to the Stejskal-Tanner equation using least – squares approach. The images were acquired with a matrix size of 192x192 with 75 slices. Three b-values of 0, 500 and 1000 s/mm^2 were acquired.

4.2.4 Masking

Brain masks were generated using FSL toolbox v.1.4 BET2 toolbox applied to PET and MR data [127].

4.2.5 Co-Registration

PET and MR images were co-registered using FSL toolbox v.1.4 FLIRT toolbox [128, 129].

4.2.6 Segmentation

The segmentation of the images was done from probability maps using FAST tissue-type segmentation toolbox from FSL toolbox v.1.4 [130]. The brain image was segmented in WM, GM and cerebrospinal fluid (CSF) using a T_1-weighted image.

4.2.7 Normalization of Cerebral Blood Volume (CBV)

Whole brain CBV was normalized to 3% as suggested in [131] for the estimation of the Vsi parameter.

4.3 Data Analysis

4.3.1 Region of Interest (ROI)

For a quantitative comparison, ROIs of WM and GM were selected on the healthy area contra-lateral to the tumor. Special attention was paid to not include large vessels (e.g. middle cerebral artery (MCA)) into the ROI.

4.3.2 Tumor Delineation

^{18}F-FET was used as a clinical reference to delineate the *Tumor Volume of Interest* (TVOI) using a TBR of >= 1.6 [73]. Based on the TVOI, region analysis was performed on PW metrics (Vsi, CBV, Q and VAI). Further corrections to the tumor delineation were performed based on T_1-weighted (*Fluid-Attenuated Inversion Recovery* (FLAIR) and *Magnetization-Prepared Rapid Gradient-Echo* (MP-RAGE)) with the help of one Neuroradiologist. Strongly enhancing structures such as the choroid plexus, venous and arterial vessels were carefully avoided, as were areas of tumor necrosis.

4.3.3 Parameters Quantification

PW metrics were calculated and imaged based on the methodology explained in *Chapter 3* at WM, GM and in tumor area based on ^{18}F-FET PET delineation for each patient. Vsi was calculated by equation 3.21, CBV was calculated as the area under the curve of $\Delta R_{2GE}{}^{*}$ using equation 3.9 and Q was calculated using the equation 3.14. Vessels with calibers equal to zero or greater than 300 μm, blood volume greater than 200 mL/100 g and vessel density greater than 100 were excluded from the averaging for each ROI. Also, T_1-weighted MR images were imaged for further comparison with PW and ^{18}F-FET results. This step was performed in order to investigate the vascular changes in tumor area comparing to normal tissue.

4.3.4 Local Hot spots

The hot spot (e.g. the voxel with the maximum value) for each parameter in the tumor region was localized. Therefore, the distance between the hot spots of ^{18}F-FET and Vsi, CBV and Q was calculated using the following equation:

$$\text{Distance} = \sqrt[2]{(x_{PET} - x_{PW})^2 + (y_{PET} - y_{PW})^2 + (z_{PET} - z_{PW})^2} \qquad (4.10)$$

, where $(x_{PET}, y_{PET}, z_{PET})$ corresponds to the coordinates of the voxel with the maximum intensity of ^{18}F-FET and (x_{PW}, y_{PW}, z_{PW}) corresponds to the coordinates of the voxel with the maximum of Vsi and CBV and the minimum of Q. This step was performed in order to compare PET and PW metrics information.

4.3.5 Heterogeneity Evaluation

From the steps 4.3.3 and 4.3.4, it was found that further information about the heterogeneity of the tumor should provide important complementary vascular information. Thereby, VAI was evaluated and imaged based on the methodology explained in *Chapter 3* (*Section 3.3.1.5.6*), in both normal and tumor area based on PET information.

5. Results

In this chapter, the results will be presented according to the methodology of this dissertation.

5.1 Comparisons between PW metrics

In figure 5.1, it is represented the mean vessel diameter in WM, GM and tumor area obtained from Vsi information. In figure 5.2, it is represented the normalized CBV values and in figure 5.3, the mean vessel density obtained from Q in the same regions. In *Annexe 2*, the correspondent values for each patient of Vsi, CBV and Q on the different regions can be found in the table A.2, A.3 and A.4.

In figure 5.1, figure 5.2, and figure 5.3, the mean vessel diameter, blood volume and vessel density reveal a heterogeneous variation for all the patients. Lower vessel caliber, blood volume and vessel density values were found in WM comparing to GM. From this result, the information in brain tissues of normal-appearance will be specified to WM, as this region is less vascularized.

From figure 5.1, in twenty-four patients out of twenty-five (nº 1-14, 16-25) the vessel caliber in tumor area increased and for one patient (nº 15) decreased comparing to WM. Patients 20 and 3 exhibited a higher increased percentage in tumor area comparing to WM of 60.36% (11.79 ± 5.15 μm to 29.74 ± 10.80 μm) and 40.97% (12.16 ± 4.94 μm to 20.60 ± 10.37 μm), respectively.

From figure 5.2, seventeen patients (nº 1, 3-7, 9, 12, 14, 16, 18-23, 25) shown an increased blood volume and eight (nº 2, 8, 10, 11, 13, 15, 17 and 24) a decreased in tumor area comparing to WM. Patients 12 and 5 showed a higher increase of volume fraction in tumor area comparing to WM, 65.93% (0.011 ± 0.0069 mL/100 g to 0.027 ± 0.017 mL/100 g) and 55.17% (0.013 ± 0.0056 mL/100g to 0.029 ± 0.030 mL/100 g), comparing to normal tissue, respectively.

Further, from figure 5.3, ten patients (nº 4, 8, 10, 11, 12, 15, 20, 21, 23 and 24) exhibited a lower and fifteen patients (nº 1-3, 5-7, 9, 13, 14, 16-19, 22 and 25) a higher vessel density in tumor area than WM. Patients 8 and 20, exhibited a higher decrease in tumor area comparing to WM, 36.11% (0.49 ± 0.098 $s^{-1/3}$ to 0.36 ± 0.042 $s^{-1/3}$) and 20.00% (0.50 ± 0.068 $s^{-1/3}$ to 0.40 ± 0.096 $s^{-1/3}$), respectively.

MR (FLAIR and MP-RAGE), PET (^{18}F-FET) and PW parametric (Vsi, CBV and Q) images for three patients are represented in figure 5.4, figure 5.5 and figure 5.6. In figure 5.4, patient 7, showed an increased vessel caliber and blood volume and a decreased vessel density in tumor area comparing to the brain tissues of normal-appearance. From figure 5.5, for patient 12, it is visible an increased vessel caliber and blood volume in the edge of the tumor. However, the region with higher vessel caliber did not correspond to the area with an increased blood volume. Also, a decreased vessel density was visible in tumor area comparing to brain tissues of normal-appearance. Finally, from figure 5.6, patient 14 showed a small increase of vessel caliber but a visible increase of blood volume and vessel density in tumor area.

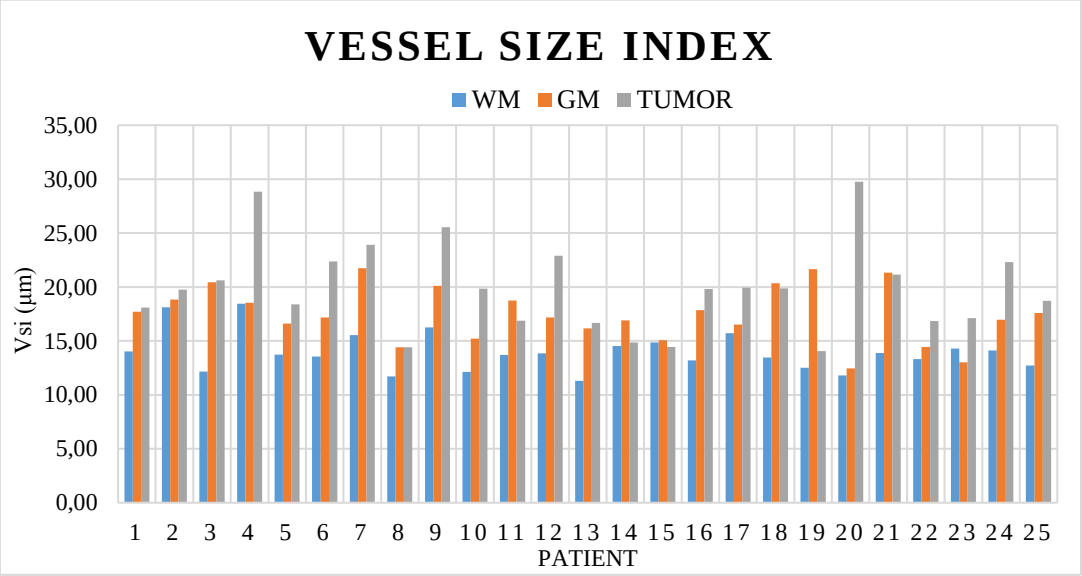

Figure 5.1: The estimated vessel size index (Vsi) in µm in different ROIs (WM, GM and tumor region) for each patient. In blue, it is represented the WM, in orange GM and in gray the tumor. Vsi was calculated for the whole brain by computing both ΔR_{2GE}^{*} and ΔR_{2SE} fitted curves using equation 3.21.

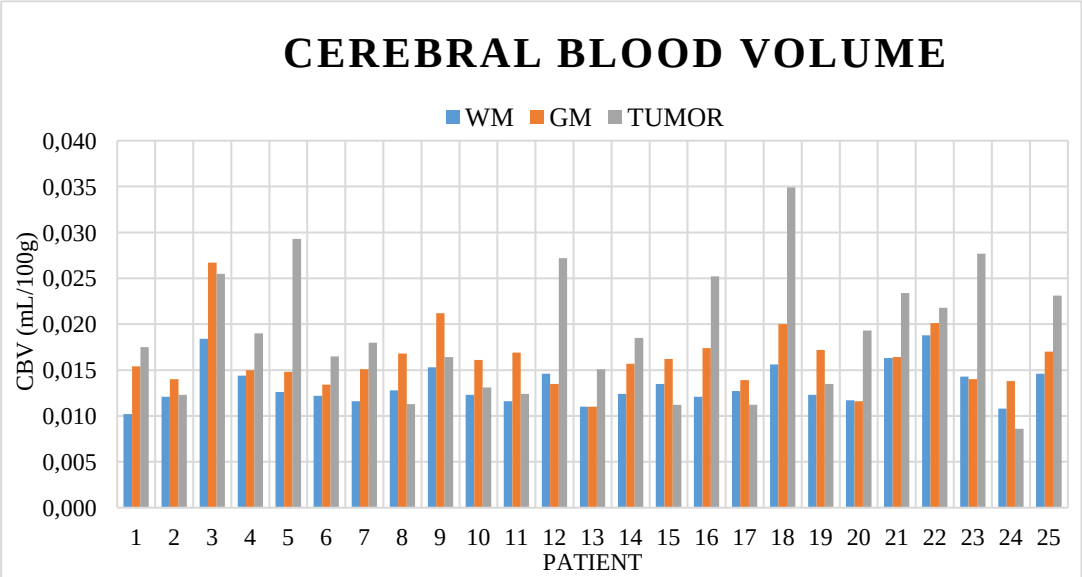

Figure 5.2: The estimated blood volume (CBV) in mL/100g in different ROIs (WM, GM and tumor region) for each patient. In blue it is represented the WM, in orange GM and in gray the tumor. CBV was calculated for the whole brain by computing ΔR_{2GE}^{*} fitted curve using equation 3.9.

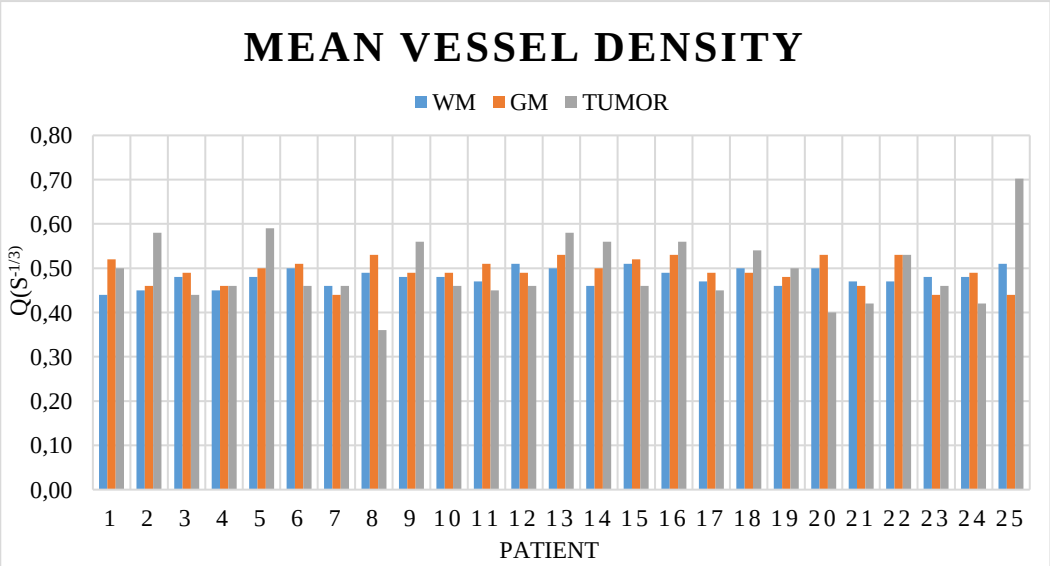

Figure 5.3: The estimated mean vessel density (Q) in $s^{-1/3}$ in different ROIs (WM, GM and tumor region) for each patient. In blue it is represented the WM, in orange GM and in gray the tumor. Q was calculated for the whole brain by computing both ΔR_{2GE}^{*} and ΔR_{2SE} fitted curves using equation 3.14.

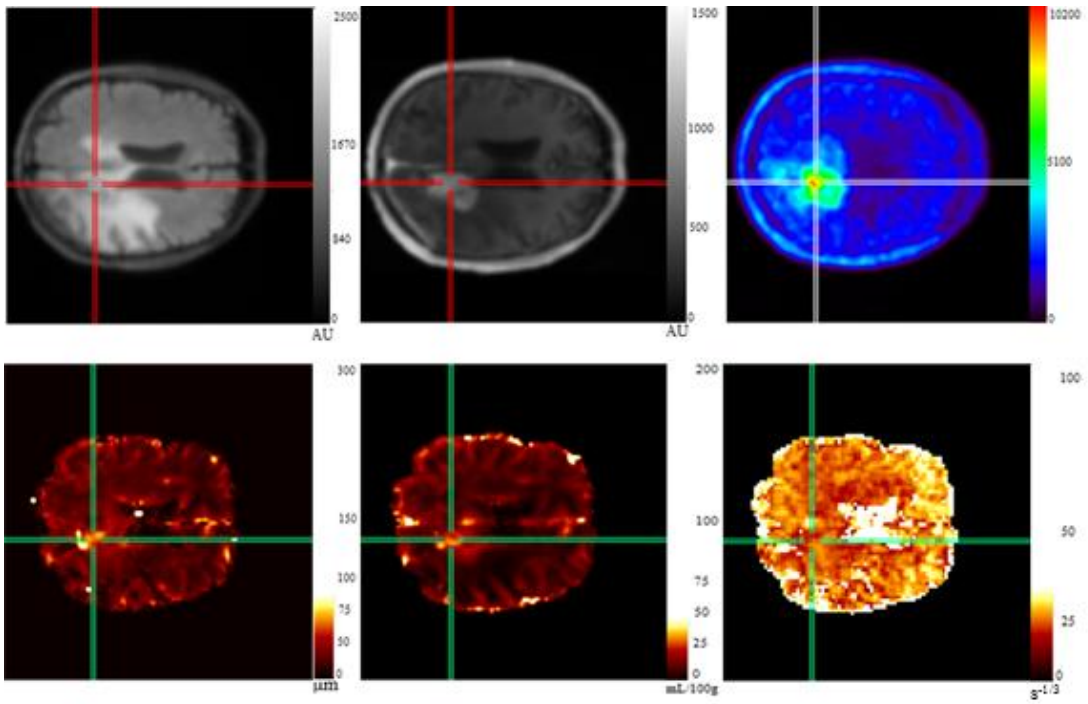

Figure 5.4: Brain tumor imaging for patient 7. In the first row, it is represented the MR (FLAIR and MP-RAGE) and PET (^{18}F-FET) images, respectively. In the second row, it is represented PW parametric images (Vsi, CBV and Q), respectively. The line indicates the area of higher activity based on ^{18}F-FET information.

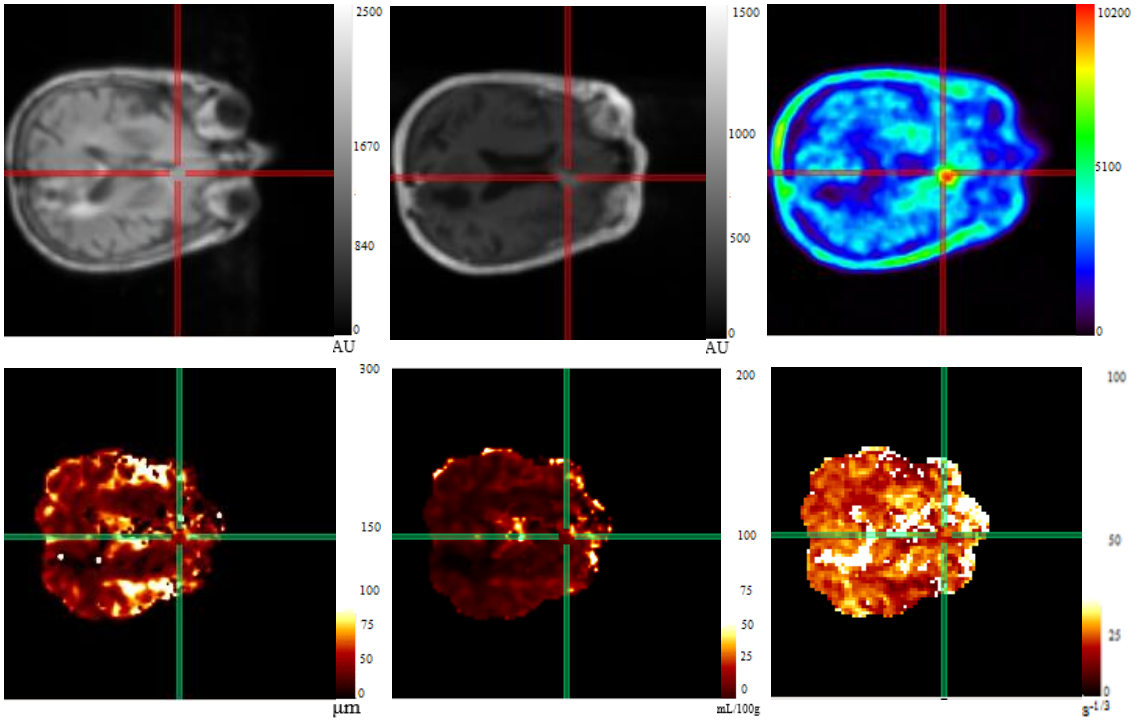

Figure 5.5: Brain tumor imaging for patient 12. In the first row, it is represented MR (FLAIR and MP-RAGE) and PET (^{18}F-FET) images, respectively. In the second row, it is represented PW parametric images (Vsi, CBV and Q), respectively. The line indicates the area of higher activity based on ^{18}F-FET information.

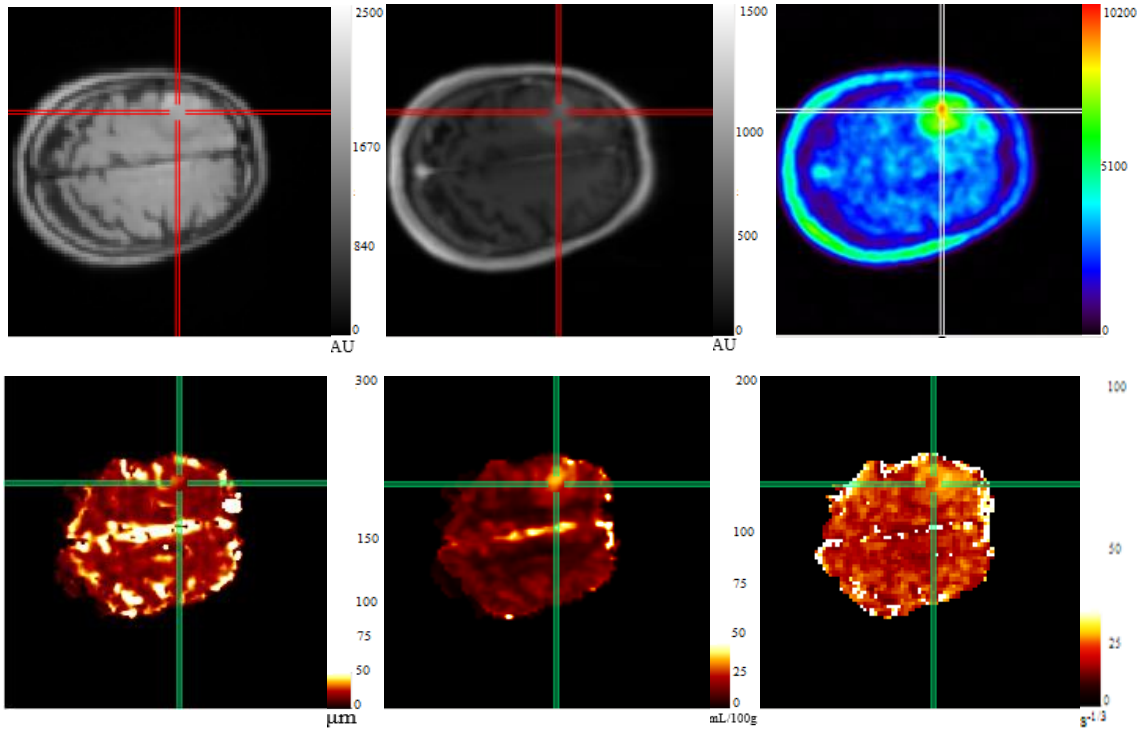

Figure 5.6: Brain tumor imaging for patient 14. In the first row, it is represented MR (FLAIR and MP-RAGE) and PET (^{18}F-FET) images, respectively. In the second row, it is represented PW parametric images (Vsi, CBV and Q), respectively. The line indicates the area of higher activity based on ^{18}F-FET information.

5.2 Distance between ^{18}F-FET and PW metrics

The localization of the hot spots, as well as the distance between the local hot spots, were accessed between PET and PW parameters in tumor area, figure 5.7. The distance was calculated in order to understand if the voxel with the maximum intensity of ^{18}F-FET corresponds to the maximum vessel caliber, blood volume and minimum vessel density. In *Annexe 2* table A.5, the distance values between ^{18}F-FET and PW metrics can be found.

From figure 5.7, all the patients exhibited a different hot spot between PET and PW metrics. The maximum uptake of ^{18}F-FET did not match the maximum vessel caliber, blood volume and lower vessel density. Thereby, ^{18}F-FET and PW parameters provide different information. Further, for the majority of the patients, the distance between Vsi, CBV and Q were different, except for patients number 1, 6, 12, 16 and 20 where the distance between Vsi and CBV was equal.

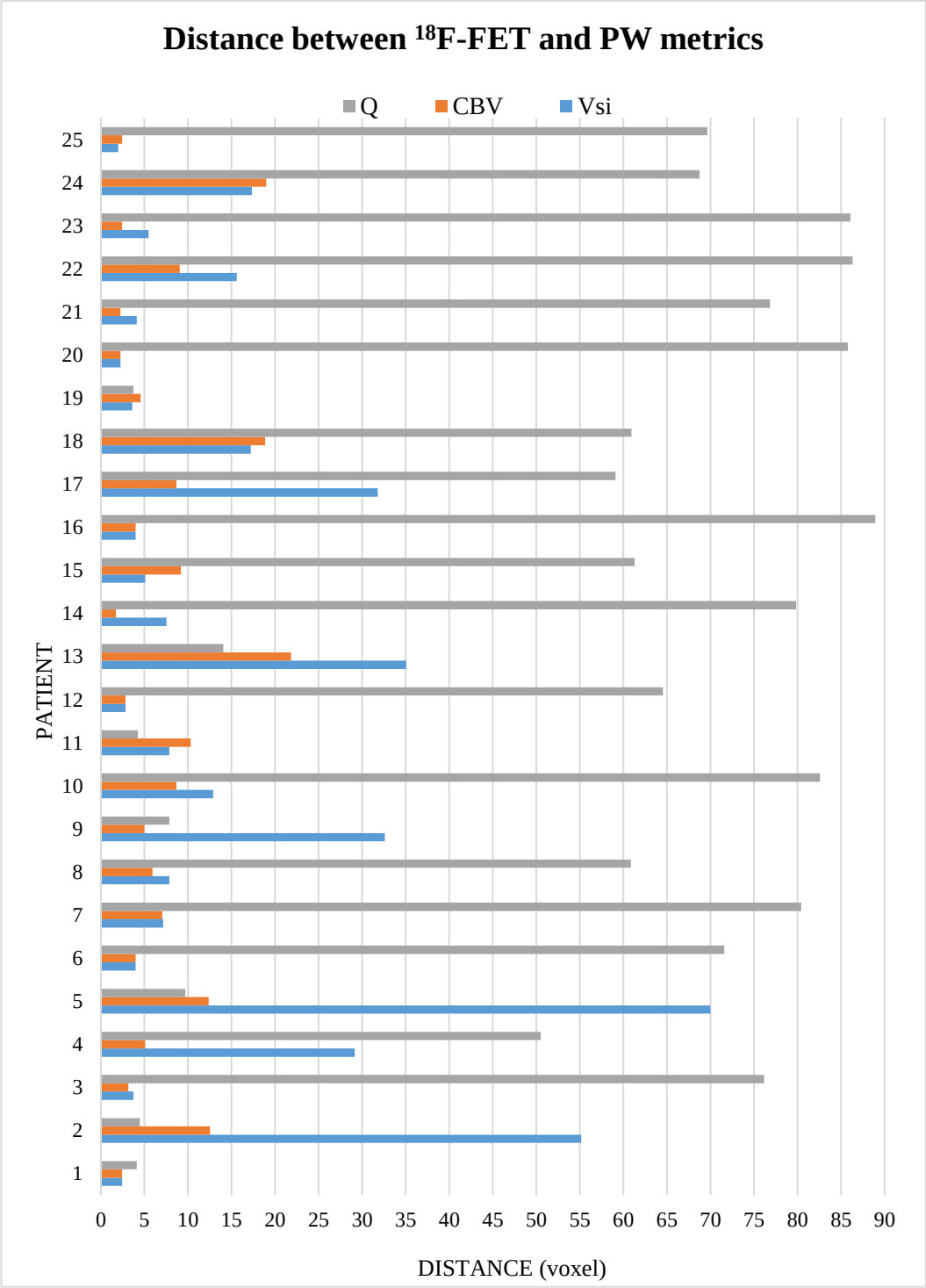

Figure 5.7: Distance between the hot spot of ^{18}F-FET data with Vsi, CBV and Q in voxels.

5.3 Combination of PW Metrics Information

From the previous results, for each patient different results were found for Vsi, CBV and Q. Also, each PW metrics revealed different hot spots localization, figure 5.7. Thereby, the combination of Vsi, CBV and Q information was evaluated, table 5.1. From table 5.1, some differences were found between PW metrics in the tumor as compared with the brain tissues of normal-appearance showing that, complementary vascular information was assessed for each patient. Furthermore, from the combination of PW metrics, a signal variation between WM and GM was obtained (figure 5.1, figure 5.2 and figure 5.3).

Table 5.1: Combination of PW metrics (Vsi, CBV and Q) information in tumor area comparing with the brain tissues of normal-appearing WM. If the vessel caliber, density and blood volume increased, the box is filled with an up arrow. Otherwise with a down arrow.

COMBINED INFORMATION			
PATIENT	**Vsi**	**CBV**	**Q**
1	↑	↑	↑
2	↑	↓	↑
3	↑	↑	↑
4	↑	↑	↓
5	↑	↑	↑
6	↑	↑	↑
7	↑	↑	↑
8	↑	↓	↓
9	↑	↑	↑
10	↑	↓	↓
11	↑	↓	↓
12	↑	↑	↓
13	↑	↓	↑
14	↑	↑	↑
15	↓	↓	↓
16	↑	↑	↑
17	↑	↓	↑
18	↑	↑	↑
19	↑	↑	↑
20	↑	↑	↓
21	↑	↑	↓
22	↑	↑	↑
23	↑	↑	↓
24	↑	↓	↓
25	↑	↑	↑

5.4 Vessel Architecture Imaging

For each patient, the vessel architecture was evaluated based on ^{18}F-FET tumor delineation. Therefore, information about the distribution of the different type of vessels in the tumor was accessed.

The pairwise $\Delta R_{2GE}{}^{*}$ and ΔR_{2SE} curves were computed in both normal and tumor areas and different results were obtained. First, from analyses of the vessel voxel curves, an increased vessel caliber and higher blood volume was observed in tumor area, in contrast to normal tissue. In figure 5.8b, it is illustrated the obtained vessel voxel curve for tumor and normal area. Second, based on this information and by evaluating the time shift between GE and SE curves, a parametric image was computed revealing information about the architecture of the tumor i.e. the distribution of the different vessels in the tumor area (arteries, capillaries, and veins). In figure 5.8c, it is represented the imaging of VAI in tumor area for patient 2.

Furthermore, for three patients (nº 2, 7 and 12) parametric images of VAI were evaluated and compared with MR (MP-RAGE) and PET (^{18}F-FET) information, figure 5.9, figure 5.10 and figure 5.11. From figure 5.9, for patient 2, an increased distribution of arteries (green) than capillaries (red) and veins (blue) was found in the tumor area. Also, a higher distribution of capillaries and veins is visible on the edge of the tumor comparing with the center. From figure 5.10, patient 7 exhibited an increased distribution of arteries in the center of the tumor and of capillaries in the edge with a reduced distribution of veins. Finally, from figure 5.11, for patient 12, a similar distribution of the different type of vessels was found.

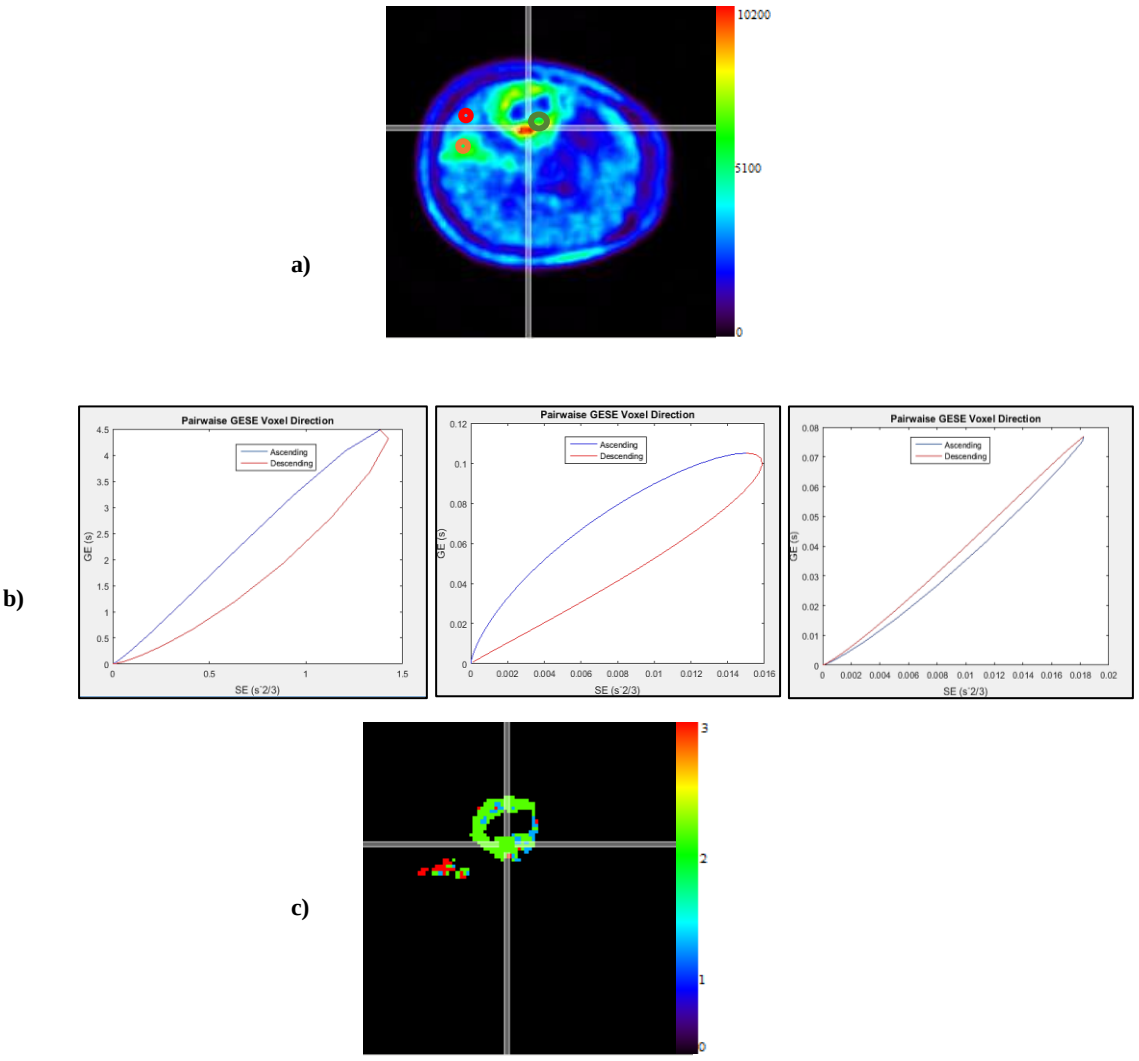

Figure 5.8: Representation of VAI methodology for patient 2. a) ^{18}F-FET imaging. b) Representation of the Voxel pairwise GE SE. For tumor area, dot in orange and green in (a) corresponds to the first and second graphs, respectively. For normal tissue, dot in red, corresponds to the third graph. c) Parametric image of VAI. The blue color match with larger venues and smaller calibers and arteries (venues + capillaries), the red color with both fast inflow small vessels and larger inflow larger vessels (capillaries) and the green color with small caliber vessels, arteries and capillaries (arteries + capillaries).

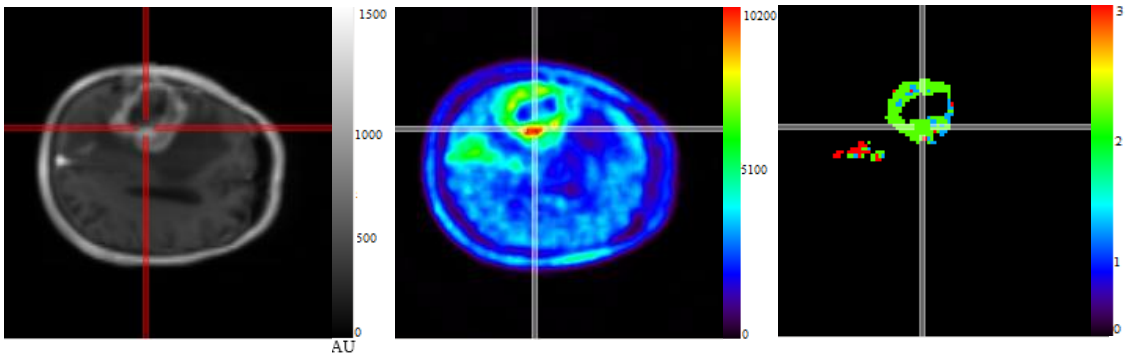

Figure 5.9: Brain tumor imaging for patient 2 for one slice. The left to the right, MR (MP-RAGE), PET (^{18}F-FET) and VAI images in tumor area based on ^{18}F-FET information. The line indicates the higher tumor activity based on ^{18}F-FET information.

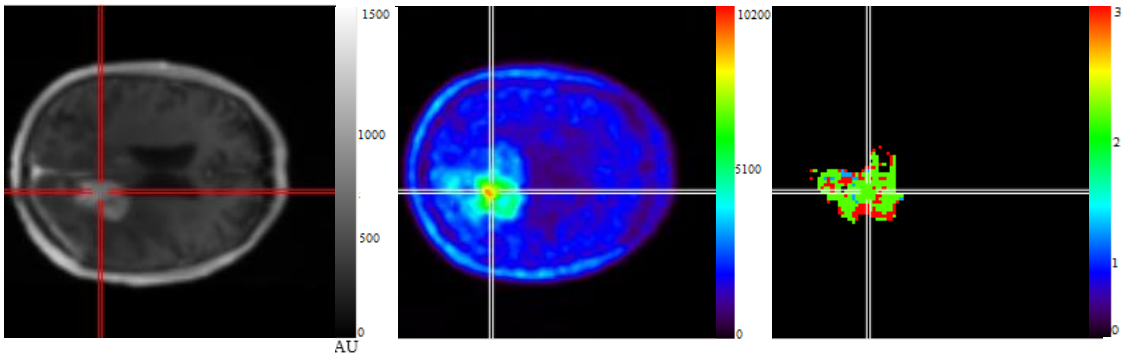

Figure 5.10: Brain tumor imaging for patient 7 for one slice. The left to the right, MR (MP-RAGE), PET (^{18}F-FET) and VAI images in tumor area based on ^{18}F-FET information. The line indicates the higher tumor activity based on ^{18}F-FET information.

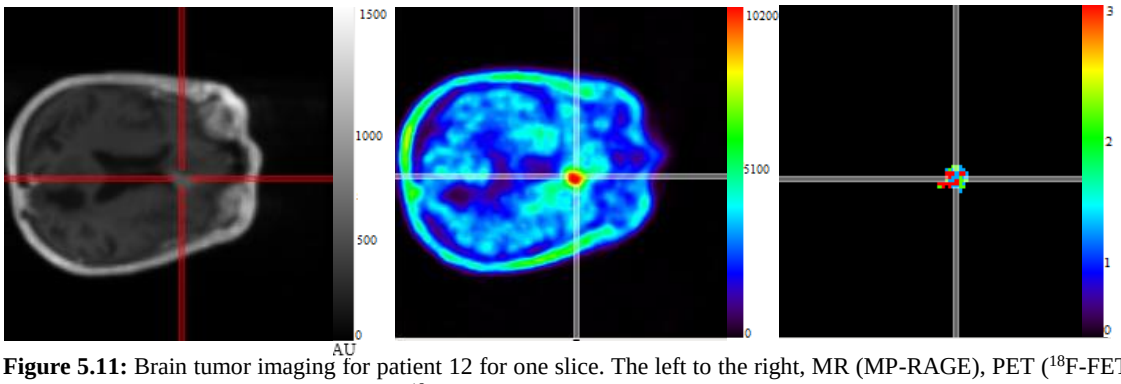

Figure 5.11: Brain tumor imaging for patient 12 for one slice. The left to the right, MR (MP-RAGE), PET (^{18}F-FET) and VAI images for tumor area based on ^{18}F-FET information. The line indicates the higher tumor activity based on ^{18}F-FET information.

6. Discussion and Conclusion

In this chapter, the discussion of the results obtained in this dissertation will be presented, along with final consideration on the overall dissertation and possible future endeavors.

PET using ^{18}F-FET provides important diagnostic information in addition to conventional MR imaging on tumor extent and activity of cerebral gliomas. Previous publications have shown a mismatch between the vascular information from PWI and metabolic information from ^{18}F-FET [12]. The main goal of this work was to explore the vascular information (Vsi, CBV, Q and VAI) of the tumor guided by the PET information. For that, a multi-echo EPIK sequence (GESE) was used. Thereby, based on ^{18}F-FET tumor delineation, topological and structural heterogeneity information of tumor microcirculation was accessed. This information is important particularly in the clinical practice for monitoring and treatment planning of brain tumors.

Unlike the ordered microcirculatory arrangement of blood vessels found in normal tissue, the heterogeneous tumor vascular bed comprises a chaotic network of mixed vessel types, from small-caliber, capillary-like vessels to oversized and permeable post-capillary venule-like vessels and vascular malformations. Hereupon, a heterogeneous vasculature characterized by larger vessel caliber, increased blood volume and decreased vessel density should be found in tumor area comparing to normal tissue (WM and GM) in gliomas [18-23].

In this work, the first step of our data analysis was to investigate the changes of vessel caliber, vessel density and blood volume in tumor region delineated with ^{18}F-FET. As ^{18}F-FET provides an accurate tumor delineated region, which corresponds to a higher metabolism by an increased amino acid uptake, an increased vessel caliber, blood volume and decreased vessel density is expected. From our results, for all the patients, vessel caliber, blood volume and vessel density revealed a heterogeneous variation in tumor region comparing to brain tissues of normal-appearing. Also, lower values were found in WM comparing to GM, which can be explained by the reduced vascularization of WM comparing to GM tissues. Twenty-four patients out of twenty-five exhibited an increased vessel caliber, seventeen patients an increased blood volume and ten patients a decreased vessel density as compared with the brain tissues in WM, (figure 5.1, figure 5.2, figure 5.3). Moreover, vascular caliber can not be assessed using FLAIR and MP-RAGE MR techniques, (figure 5.4, figure 5.5, and figure 5.6). FLAIR images allow the assessment of tumor-related infiltration information and no further specifications can be revealed about vascularity. In MP-RAGE, the disruption of BBB is visible by the entrance of the CA in the tumor area. However, by using this MR technique it is only possible to perform the delineation of the tumor area, and no other specific information about the heterogeneity and the caliber of the vessels can be obtained. Furthermore, from the analysis of the PW images (Vsi, CBV and Q) some differences were found comparing to the results obtained using ^{18}F-FET. This result can be explained from the fact of the tumor area obtained from ^{18}F-FET delineation did not correspond to the area with a higher vessel size.

The second step of this work was to compare ^{18}F-FET and Vsi, CBV and Q information by computing and comparing the local hot spots between both techniques. Based on a previous study [12], it is expected that the local hot spots of ^{18}F-FET and CBV may be different. Our results reported that the locations of the local hot spots differ considerably between ^{18}F-FET and Vsi, CBV and Q, figure 5.7. Thereby, higher metabolically activity in gliomas depicted by amino acid PET is not reflected by a larger vessel diameter, higher blood volume or lower vessel density from

PWI. A higher distance between PW metrics and ^{18}F-FET was observed for Q. This fact can be explained due to the lower sensitivity of Q. Furthermore, different hot spots were found between PW metrics, revealing that each one provides different vascular information about the tumor.

From the conclusions reported in the previous steps, in the third step of our data analyses, the combination of PW metrics information was investigated. From the analyses of table 5.1, some differences were found between PW metrics in the tumor as compared with the brain tissues of normal-appearance. Those differences can be explained accordingly to the literature [17, 18, 93, 108-112]. The literature reported that Vsi exhibits a higher vascular sensitivity comparing to CBV and Q, as it is influenced by ADC maps and CBV, equation 3.21. Otherwise, as Q evaluation is independent on CA concentration (equation 3.14), this parameter showed less sensitivity to vascular changes comparing to CBV and Vsi. In addition, differences between CBV and Vsi can also be explained by the different genetic pathways of both parameters, which reflect different molecular structures [132]. Further information can be found in [132]. Thereby, from the combination of PW metrics, complementary vascular information was assessed for each patient. Moreover, from the combination of PW metrics signal variations between WM and GM were found, whose were not possible to be obtained from the analysis of these metrics individually.

Motivated by the previous results on the last step of our work, a complementary assessment of the topological and structural heterogeneity of tumor microcirculation was performed by evaluating VAI parameter. In this step, VAI was evaluated in two steps. The first one comprised the analysis of the scatter plot and the second one the identification and comparison of TTP of GE and SE curves. From the evaluation of first step, it was observed that, in contrast with normal tissue, tumor area presented an increased vessel caliber and higher blood volumes (higher slopes and area, respectively), whose corresponds to fast and/or slow inflow and larger and/or smaller vessel , figure 5.8b. Both differences in vessel vortex curve direction and slope can be explained by the differences in radii and oxygen saturation levels between the different types of vessels caused by the abnormal vascularity [12]. Subsequently, by combining these results with the second step procedure, a parametric image was computed where the correspondent localization and distribution of arteries, venues and capillaries is described based on ^{18}F-FET tumor delineation, figure 5.8c.

Furthermore, as shown in figure 5.9, figure 5.10 and figure 5.11, from VAI methodology and in contrast with MP-RAGE, information about the tumor vasculature can be obtained. Thereby, the combination of VAI and ^{18}F-FET information may reliable useful in tumors, allowing the assessment of information about the architecture of the vessels in regions with a higher activity.

A general limitation of this study is the highly dependence of the good performance of $\Delta R_{2GE}{}^{*}$and ΔR_{2SE} curve fitting for the feasibility of PW metrics. The underestimation of Vsi values obtained can be explained by the median value used for normal-appearance of 3% [131]. This value was selected according to a collection of literature values measured with PET [132] and others recent studies [114, 121] however, some studies reported a value of 6% [18, 111]. Also, the computation of the ADC maps using the mono-exponential model instead of bi-exponencial model could also influenced the Vsi results.

Moreover, the small number of 25 included patients and the unsufficent information available to provide a comparison between groups (LGG and HGG) do not allow to draw conclusions regarding the grading of tumors. However, if it was possible to group the patients into two different groups, a threshold could be defined for each PW parameter (Vsi,CBV and Q) between each group of patients. This threshold could be obtained using the same

methodology (Statistical Analysis based) reported in Kang et al. [115], where a Kruskal-Wallis H test was used to evaluate differences between the parameters and the ANOVA to perform a comparison between the groups.

In conclusion, the metabolic guided analysis of VSI data provides further insights into the complex nature of the tumor vascularity and heterogeneity. Also, as different information could be found between the amino acid uptake from ^{18}F-FET and VSI, the combination of both informations can be reliable important for radiologists by opening the possibility of access to new information, previously only available to pathologists and mainly derived from biopsies.

Future Work

To try and mitigate the shortcomings of this dissertation, an improvement of this work would be to consider a larger cohort of patients with different malignancies (LGG and HGG) and to perform a comparison between our data and histology data. Furthermore, an investigation of the feasibility of the presented methodology pre and post treatment could bring new highlights in to the clinical practice. Moreover, an automatic segmentation with specific information for larger vessels could be applied in order to avoid including those in the analysis. Full-brain coverage would also be desired in order to obtain full brain vascular information.

References

[1] H. Hricak, B.A. Choi, A.M. Scott, K. Sugimura, A. Muellner, G. von Schulthess and S.M K. Larson, "Global trends in hybrid imaging 1," *Radiology*, vol. 257, no. 2, pp. 498–506, Nov. 2010.

[2] G.H. Jahng, K.L. Li, L. Ostergaard and F. Calamante, "Perfusion magnetic resonance imaging: A comprehensive update on principles and techniques," *Korean Journal of Radiology*, vol. 15, no. 5, pp.554–77, Sep. 2014.

[3] L. Willats and F. Calamante, "The 39 steps: Evading error and deciphering the secrets for accurate dynamic susceptibility contrast MRI," *NMR in Biomedicine*, vol. 26, no. 8, pp. 913–31, Jul. 2012.

[4] F. Calamante, "Arterial input function in perfusion MRI: A comprehensive review," *Progress in Nuclear Magnetic Resonance Spectroscopy*, vol 74, pp. 1–32, 2003.

[5] C.Z. Simonsen, D.F. Østergaard, P. Smith, V. Poulsen and C. Gyldensted, "Comparison of gradient-and spin-echo imaging: CBF, CBV and MTT measurements by bolus tracking," *Journal of Magnetic Resonance Imaging*, vol. 12, no. 3, pp. 411–16, 2000.

[6] J. Boxerman, K. Schmainda and R. Weisskoff, "Relative cerebral blood volume maps corrected for contrast agent extravasation significantly correlate with glioma tumor grade, whereas uncorrected maps do not," *American Journal of Neuroradiology*, vol. 27, no. 4, pp. 859–67, Apr. 2006.

[7] E. Miele, G.P. Spinelli, F. Tomao, A. Zullo, F. De Marinis, G. Pasciuti, L. Rossi, F. Zoratto and S. Tomao, "Positron emission tomography (PET) radiotracers in oncology – utility of 18F-Fluoro-deoxy-glucose (FDG)-PET in the management of patients with non-small-cell lung cancer (NSCLC)," *Journal of Experimental & Clinical Cancer Research*, vol. 27, no. 1, pp.52, Oct. 2008.

[8] G. Pöpperl, F.W. Kreth, J. Herms, W. Koch, J.H. Mehrkens, F.J. Gildehaus, H.A. Kretzschmar, J.C. Tonn and K Tatsch, "Analysis of ^{18}F-FET PET for grading of recurrent gliomas: Is evaluation of uptake kinetics superior to standard methods?," *Journal of Nuclear Medicine*, vol. 47, no. 3, pp. 393–403, Mar. 2006.

[9] N. Galldiks, G. Stoffels, C. Filss, M. Rapp, T. Blau, C. Tscherpel, G. Ceccon, V. Dunkl, M. Weinzierl, M. Stoffel, M. Sabel, G.R. Fink, N.J. Shah and K.J. Langen, "The use of dynamic O-(2-18F-fluoroethyl)-l-tyrosine PET in the diagnosis of patients with progressive and recurrent glioma," *Neuro Oncology*, pp. 88, May 2015.

[10] V. Dunet, A. Pomoni, A. Hottinger, M. Nicod-Lalonde and J. Prior, "Performance of ^{18}F-FET versus ^{18}F-FDG-PET for the diagnosis and grading of brain tumors: Systematic review and meta-analysis," *Neuro Oncology*, vol. 18, no. 3, pp. 426–34, Aug. 2015.

[11] V. Dandois, D. Rommel, L. Renard, J. Jamart and G. Cosnard, "Substitution of 11C-methionine PET by perfusion MRI during the follow-up of treated high-grade gliomas: Preliminary results in clinical practice," *Journal of Neuroradiology*, vol. 37, no. 2, pp. 89–97, Jul. 2009.

[12] C.P. Filss, N. Galldiks, G. Stoffels, M. Sabel, H.J. Wittsack, B. Turowski, G. Antoch, K. Zhang, G.R. Fink, H.H. Coenen, N.J. Shah, H. Herzog, K.J. Langen, "Comparison of ^{18}F-FET PET and perfusion-weighted MR imaging: A PET/MR imaging hybrid study in patients with brain tumors," *Journal of Nuclear Medicine*, vol. 55, no. 4, pp. 540–5, Mar. 2014.

[13] O.M. Henriksen, V.A. Larsen VA, A. Muhic A, A.E. Hansen AE, H.B. Larsson , H.S. Poulsen and I. Law, "Simultaneous evaluation of brain tumour metabolism, structure and blood volume using [(18)F]-fluoroethyltyrosine (FET) PET/MRI: Feasibility, agreement and initial experience," *European Journal of Nuclear Medicine and Molecular Iimaging*, vol. 43, no. 1, pp. 103–12, Sep. 2015.

[14] M. Zaitsev, K. Zilles and N. J. Shah, "Shared k-space Echo-planar imaging with keyhole," *Magnetic Resonance in Medicine*, vol. 45, no. 1, pp. 109–117, Jan. 2001.

[15] C.R. Fisel, J.L. Ackerman, R.B. Buxton, L. Garrido, J.W. Belliveau, B.R. Rosen and T.J. Brady, "Numerical modeling of susceptibility-related MR signal dephasing with vessel size measurement: Phantom validation at 3T," *Magnetic Resonance in Medicine*, vol. 72, no. 3, pp. 646–58, Oct. 2013.

[16] C. Xu, V. Kiselev, H. Möller and J. Fiebach, "Dynamic hysteresis between gradient echo and spin echo attenuations in dynamic susceptibility contrast imaging," *Magnetic Resonance in Medicine*, vol. 69, no. 4, pp. 981–91, May 2012.

[17] K.E Emblem, K. Mouridsen, A. Bjornerud, C.T, Farrar, D. Jennings, R.J.H. Borra, P.Y. Wen, P. Ivy, T.Tracy, T. Batchelor, B.R. Rosen, R.J. Jain and G. Sorensen, "Vessel architectural imaging identifies cancer patient responders to anti-angiogenic therapy," *Nature Medicine*, vol. 19, no. 9, pp. 1178–83, Aug. 2013.

[18] V. Kiselev, R. Strecker, S. Ziyeh, O. Speck and J. Hennig, "Vessel size imaging in humans," *Magnetic Resonance in Medicine*, vol. 53, no. 3, pp. 553–63, Feb. 2005.

[19] J. Jensen and R. Chandra, "MR imaging of microvasculature," *Magnetic Resonance in Medicine*, vol. 44, no. 2, pp. 224–30, Aug. 2000.

[20] J. Dennie, J. B. Mandeville, J. L. Boxerman, S.D. Packard, B. R. Rosen and R. M. Weisskoff, "NMR imaging of changes in vascular morphology due to tumor angiogenesis," *Magnetic Resonance in Medicine*, vol. 40, no. 6, pp. 793–99, Dec. 1998.

[21] I. Tropres S. Grimault, A. Vaeth, E. Grillon, C. Julien, J.F. Payen, L. Lamalle, M. Decorps. "Vessel size imaging," *Magnetic Resonance in Medicine*," vol. 45, pp.397–40, 2001.

[22] J. Jensen, H. Lu and M. Inglese, "Microvessel density estimation in the human brain by means of dynamic contrast-enhanced echo-planar imaging," *Magnetic Resonance in Medicine*, vol. 56, no. 5, pp. 1145–50, Oct. 2006.

[23] C.T. Farrar, W.S. Kamon, C.D. Ley, Y.R. Kim, S.J. Kwon, G. Dai, B.R. Rosen, E. di. Tomaso, R.K. Jain and A.G. Sorensen, " In *vivo* validation of MRI vessel caliber index measurement methods with intravital optical microscopy in a U87 mouse bain tumor model," *Neuro Oncology*, vol. 12, pp. 341–50, 2010.

[24] J. Nagy, S. Chang, S. Shih, A. Dvorak and H. Dvorak, "Heterogeneity of the tumor vasculature," *Seminars in thrombosis and Haemostasis*, vol. 36, no. 3, pp. 321–31, May 2010.

[25] T. Beyer, L.S. Freudenberg, D.W. Townsend and J. Czernin, "The future of hybrid imaging—part 1: Hybrid imaging technologies and SPECT/CT," *Insights Imaging*. vol. 2, no. 2, Jan. 2011.

[26] I.I. Rabi, S. Millman, P. Kusch and J.R Zacharias, "The molecular beam resonance method for measuring nuclear magnetic moments. The magnetic moments of $^{3}Li_{6}$, $^{3}Li_{7}$ and $^{9}F_{19}$," *Physical Review*, vol. 55, no. 6, pp.526, Mar. 1939.

[27] F. Bloch, W. Stanford, W. Hansen and M. Packard, "The nuclear induction experiment," *Physical Review*, vol. 70, no. 7-8, pp. 474, Oct. 1946.

[28] E.M. Purcell, H. Torrey and R. Pound, "Resonance absorption by nuclear magnetic moments in a solid," *Physical Review*, vol.69, no.1-2, pp. 37, 1946.

[29] P. Lauterbur, "Image formation by induced local interactions. Examples employing nuclear magnetic resonance. 1973," *Clinical Orthopaedics and Related Research*, pp. 3–6, Jul. 1989.

[30] D.B. Plewes and W. Kucharczyk, "Physics of MRI: A primer," *Journal of Magnetic Resonance Imaging*, vol. 35, no. 5, pp. 1038–54, Apr. 2012.

[31] W.S. Hinshaw and A.H. Lent, "An Introduction to NMR Imaging: From the Bloch Equation to the Imaging Equation," *Proceedings of the IEEE*, vol. 71, no.3, pp.338-50, 1983.

[32] I. Neuner, J. Mauler, J. Arrubla, E. Kops, L. Tellmann, L. Scheins and N. J. Shah, "Simultaneous tri-modal MR-PET-EEG imaging for the investigation of resting state networks in humans," *SpringerNature*, vol. 2, no. Suppl1, May 2015.

[33] D.W. McRobbie, E. A. Moore, M. J. Graves and M. R. Prince, "MRI from picture to proton," *Cambridge University Press*, 2007.

[34] V. Keereman, *MRI-Based Attenuation Correction for Emission Tomography*, Ph.D dissertation, Dept. Electronics and Information, Ghent University, Gent, 2012.

[35] S. Ljunggren, "A simple graphical representation of fourier-based imaging methods," *Journal of Magnetic Resonance*, vol. 54, no. 2, pp. 338–343, Sep. 1983.

[36] D. Twieg, "The k-trajectory formulation of the NMR imaging process with applications in analysis and synthesis of imaging methods," *Medical Physics*, vol. 10, no. 5, pp. 610–21, Sep. 1983.

[37] M. Poustchi-Amin, S.A. Mirowitz, J.J. Brown, R.C. McKinstry and T. Li, "Principles and applications of echo-planar imaging: A review for the general Radiologist1," *RadioGraphics*, vol. 21, no. 3, pp. 767–779, May 2001.

[**38**] R.L. DeLaPaz,"Echo-planar imaging," *RadioGraphics*, vol. 14, no. 5, pp. 1045–1058, Sep. 1994.

[39] A.W. Toga, "Brain mapping-An Encyclopedic Reference," vol. 1, pp. 53-59, Feb. 2015.

[40] A. Jesmanowicz, P. Bandettini and J. Hyde, "Single-shot half k-space high-resolution gradient-recalled EPI for fMRI at 3 Tesla," *Magnetic Resonance in Medicine*, vol. 40, no. 5, pp. 754–62, Oct. 1998.

[41] J. D. Swisher, J. A. Sexton, J. C. Gatenby, J. C. Gore and F. Tong, "Multishot versus single-shot pulse sequences in very high field fMRI: A comparison using Retinotopic mapping," *PLosONE*, vol. 7, no. 4, p. e34626, Apr. 2012.

[42] F. Hennel, "Multiple-shot echo-planar imaging," *Concepts in Magnetic Resonance*, vol. 9, no. 1, pp. 43–58, 1997.

[43] N.J. Shah, K. Zilles and F. J, "Patent US6781372 - imaging process in the spatial frequency space and useful for examining the properties of object," 2000.

[44] S. Yun, M. Reske, K. Vahedipour, T. Warbrick and N.J. Shah, "Parallel imaging acceleration of EPIK for reduced image distortions in fMRI," *NeuroImage*, vol. 73, pp. 135–43, Feb. 2013.

[45] W.K. Fishbein, J.C. McGowan and R. G. Spencer, "Hardware for Magnetic Resonance Imaging," *Springer-Verlag* Berlin Heidelberg. 2005

[46] J.T Vaughan, C.J. Snyder , L.J DelaBarre , P.J. Bolan , J. Tian , L. Bolinger , G. Adriany , P. Andersen , J.Strupp, K. Ugurbil, "Whole-body imaging at 7T: Preliminary results," *Magnetic Resonance in Medicine*, vol. 61, no. 1, pp. 244–8, Dec. 2008.

[47] J.T Vaughan, L.J DelaBarre , C.J. Snyder , J. Tian , C. Akgun , D. Shrivastava , W. Liu , C .Olson , G. Adriany, J. Strupp , P. Andersen , A. Gopinath , P.F. van de Moortele , M. Garwood , K. Ugurbil , "9.4T human MRI: Preliminary results," *Magnetic Resonance in Medicine*, vol. 56, no. 6, pp. 1274–82, Nov. 2006.

[48] M. Alecci, C. M. Collins, M. B. Smith and P. Jezzard, "Radio frequency magnetic field mapping of a 3 Tesla birdcage coil: Experimental and theoretical dependence on sample properties," *Magnetic Resonance in Medicine*, vol. 46, no. 2, pp. 379–85, 2001.

[49] H Anger, "A new instrument for mapping gamma-ray emitters," *Biology and Medicine Quarterly Report. Review of Scientific Instruments*, vol. 29, pp. 27, 1958.

[50] H. Anger and D. Rosenthal, "Scintillation camera and positron camera in Medical radioisotope scanning," *International Atomic Energy Agency*, 1959.

[51] H. Anger and D. Vandyke, "Human bone marrow distribution shown in vivo by iron-52 and the positron scintillation camera" *ScienceDirect*, vol.144, pp. 1587-9, July 1964

[52] J.S. Robertson and S. Bozzo, "Positron scanner for brain tumors," *6th IBM Medical Symposium*, pp.631–45, 1964.

[53] D.W. McRobbie, E.A. Moore, M.J. Graves and M.R. Prince, "MRI from picture to proton," *Cambridge University Press*, 2nd edition, Fev. 2007.

[54] C. Weirich and H. Herzog, "Molecular Imaging in the Clinical Neurosciences, chapter Instrumentation and Physical Principles, *Neuromethods*, vol.71, no.3, pp.1–22, 2012.

[55] P.E Valk, D.L. Bailey, D.W. Townsen, M.N. Maisey, "Positron Emission Tomography: Basic Science a Clinical Pratice," *Springer-Verlag, American Journal of Neuroradiology*, vol. 37, no. 9, pp.69-90, London 2003.

[56] B. Bendriem and D. W. Townsend, "The Theory and Practice of 3D PET*," Springer*, pp. 167, 1998.

[57] "Time-of-flight Positron emission tomography (TOF-PET)," Delft University of Technology, 2016. [Online]. Available: http://www.tnw.tudelft.nl/en/about faculty/departments/radiation-science-technology/research/researc]h-groups/radiation-and-isotopes-for-health/research/time-of-flight-positron-emission-tomography-tof-pet/. Accessed: Sep. 25, 2016.

[58] H. Hudson and R. Larkin, "Accelerated image reconstruction using ordered subsets of projection data," *IEEE Transactions on Medical Imaging,* vol. 13, no. 4, pp. 601–9, Jan. 1994.

[59] L. Shepp and Y. Vardi, "Maximum likelihood reconstruction for emission tomography," *IEEE Transactions on Medical Imaging,* vol. 1, no. 2, pp. 113–22, Jan. 1982.

[60] F. Fahey, "Data acquisition in PET imaging," *Journal of Nuclear Medicine Technology,* vol. 30, no. 2, pp. 39–49, Jun. 2002.

[61] A.C. Kak and M. Slaney, "Principles of computerized Tomographic imaging," *IEEE Press*, 1988.

[62] J. Ollinger, "Model-based scatter correction for fully 3D PET," *Physics in Medicine and Biology*, vol. 41, no. 1, pp. 153–76, Jan. 1996.

[63] C.C. Watson, "New faster image-based scatter correction for 3d pet," *IEEE Transactions on Nuclear Science*, vol.47, no. 4, pp. 1587–94, 2000.

[64] D. Brasse, P. E. Kinahan, C. Lartizien, C. Comtat, M. Casey and C. Michel, "Correction methods for random coincidences in fully 3D whole-body PET: impact on data and image quality. *Journal of Nuclear Medicine*, vol.46, no. 5, pp. 859–67, 2005.

[65] V. Keereman, P. Mollet, Y. Berker, V. Schulz and S. Vandenberghe, "Challenges and current methods for attenuation correction in PET/MR," *Magnetic Resonance Materials in Physics, Biology and Medicine,* vol. 26, no. 1, pp. 81–98, Aug. 2012.

[66] T. Oakes, V. Sossi and T. Ruth, "Normalization for 3D PET with a low-scatter planar source and measured geometric factors," *Physics in Medicine and Biology,* vol. 43, no. 4, pp. 961–72, May 1998.

[67] K. Herholz, U. Pietrzyk and J. Voges, "Correlation of glucose consumption and tumor cell density in astrocytomas. A stereotactic PET study," *Journal of Neurosurgery*, vol. 79, no. 6, pp. 853–58, 1993.

[68] M. Bergstrom, H. Lundqvist and K. Ericson, "Comparison of the accumulation kinetics of L-(methyl-C)-methionine and D-(methyl-C)-methionine in brain tumors studied with positron emission tomography," *Acta Radiologica*, vol. 28, no. 3, pp. 225–29, May 1987.

[69] Y. Okita, M. Kinoshita and T. Goto, N. Kagawa, H. Kishima, E. Shimosegawa, J. Hatazawa, N. Hashimoto and T. Yoshimine, "C-methionine uptake correlates with tumor cell density rather than with microvessel density in glioma: a stereotactic image-histology comparison," *NeuroImage*, vol. 49, no. 4, pp. 2977–2982, 2010

[70] M. Sasaki, Y. Kuwabara, T. Yoshida M.Nakagawa, T. Fukumura, F. Mihara, T. Morioka , M. Fukui and K. Masuda, "A comparative study of thallium-201 SPET, carbon-11 methionine PET and fluorine-18 fluorodeoxyglucose PET for the differentiation of astrocytic tumors," *European Journal of Nuclear Medicine*, vol. 25, no. 9, pp. 1261–69, 1998.

[71] D. Pauleit, G. Stoffels, A. Bachofner, F.W. Floeth , M. Sabel, H. Herzog, L. Tellmann, P. Jansen, G. Reifenberger G, K.Hamacher, H.H.Coenen and K.J. Langen, "Comparison of ^{18}F-FET and F-FDG PET in brain tumors," *Nuclear Medicine and Biology*, vol. 36, no. 7, pp. 779–87, 2009.

[72] W.A. Weber, H.J. Wester, A.L. Grosu M. Herz, B. Dzewas, H.J. Feldmann , M. Molls, G. Stöcklin and M. Schwaiger M, "O-(2-[F]fluoroethyl)-L-tyrosine and L-[methyl-C]methionine uptake in brain tumors: initial results of a comparative study," *European Journal of Nuclear Medicine*, vol. 27, no. 5, pp. 542–49, 2000.

[73] D. Pauleit, F. Floeth, K. Hamacher, M.J. Riemenschneider, G. Reifenberger, H.W. Müller, K. Zilles, H.H. Coenen and K.J.Langen,"O-(2-[F]fluoroethyl)-L-tyrosine PET combined with MRI improves the diagnostic assessment of cerebral gliomas," *Brain,* vol. 128, no. 3, pp. 678–87, Mars. 2005.

[74] K.J. Langen, K. Hamacher, M.Weckesser, F. Floeth, G. Stoffels, D. Bauer,H. H. Coenen and D. Pauleit, "O-(2-[18F]fluoroethyl)-L-tyrosine: uptake mechanisms and clinical applications," *Nuclear Medicine and Biology*, vol. 33, pp. 287–94, Apr. 2006.

[75] G. Pöpperl, F.W. Kreth, J.H. Mehrkens, J. Herms, K. Seelos, W. Koch, F.J. Gildehaus, H. A. Kretzschmar, J. C. Tonn and K. Tatsch, "FET-PET for the evaluation of untreated gliomas: correlation of FET uptake and uptake kinetics with tumor grading," *European Journal of Nuclear Medicine and Molecular Imaging*, vol. 34, pp. 1933–42, Dec. 2007.

[76] G.B. Saha, "Basics of PET imaging," *Springer-Verlag* New York, 2016.

[77] R. Lecomte, "Novel detector technology for clinical PET," *Europe Journal Nuclear Medical Molecular Imaging*, vol. 36, pp. 69–85, 2009.

[78] R. Grazioso, R. Ladebeck, M. Schmand and R. Krieg. APD-based PET for combined MR-PET imaging Detector. *In Proceedings of the ISMRM 13th Scientific Meeting*, 2005.

[79] H. Herzog and V. Den, "Combined PET/MR systems: An overview and comparison of currently available options," *The Quarterly Journal of Nuclear Medicine and Molecular Imaging*, vol. 56, no. 3, pp. 247–67, Jun. 2012.

[80] N.E. Bolus, R. George, J. Washington and B.R. Newcomer, "PET/MRI: The blended-modality choice of the future?, " *Journal of Nuclear Medicine Technology*, vol. 37, no. 2, pp. 63–71, Jun. 2009.

[81] W. Heiss, "The potential of PET/MR for brain imaging," *European Journal of Nuclear Medicine and Molecular Imaging*, vol. 36, Dec. 2008.

[82] B. Hammer, N. Christensen and B. Heil, "Use of a magnetic field to increase the spatial resolution of positron emission tomography," *Medical Physics*, vol. 21, no. 12, pp. 1917–20, Dec. 1994.

[83] Y. Shao, S. Cherry and K Farahani, "Simultaneous PET and MR imaging," *Physic Medicine Biology*, vol. 42, pp.1965–70, 1997.

[84] R. Slates, S. Cherry, A. Boutefnouchet, Y. Shao, M. Dahlbom and K. Farahani, "Design of a small animal MR compatible PET scanner," *IEEE Transations on Nuclear Sciences*, vol. 46, no. 3, pp. 565 - 70, Feb. 1998.

[85] T. Beyer, L.S. Freudenberg, J. Czernin and D.W. Townsend, "The future of hybrid imaging—part 3: PET/MR, small-animal imaging and beyond," *Insights Imaging.* vol. 2, no. 3, pp. 235–46, Mar. 2011.

[86] Y Shao, Cherry S and Farahani K, "Simultaneous PET and MR imaging," *Physic Medicine and Biology*, vol.42, pp. 1965–70, 1997.

[87] "Forschungszentrum Jülich - medical imaging physics (INM-4)," [Online]. Available: http://www.fz-juelich.de/inm/inm-4/EN/Home/home_node.html. Accessed: Sep. 25, 2016.

[88] da Silva. N, "On the Use of Image Derived Input Function for Quantitative PET Imaging with a Simultaneous Measuring MR-BrainPET," M.S.thesis, Physics Department, University of Lisbon, Lisbon, 2012.

[89] A. S. Modrek, S. N. Bayin and D. G. Placantonakis, "Brain stem cells as the cell of origin in glioma," *World Journal of Stem Cells*, vol. 6, no. 1, pp.43-52, Jan. 2014.

[90] D.N Louis, H. Ohgaki, O.D. Wiestler, W.K. Cavenee, P.C. Burger and A. Jouvet, "The 2007 WHO classification of tumors of the central nervous system," *Acta Neuropathologica*, vol. 114, no. 2, pp. 97–109, Jul. 2007.

[91] A. Omuro and L. DeAngelis, "Glioblastoma and other malignant gliomas: A clinical review," *JAMA*, vol. 310, no. 17, pp. 1842–50, Nov. 2013.

[92] R. Jain, di Tomaso, D. Duda and J. Loeffler, A. Sorensen and T. Batchelor, "Angiogenesis in brain tumors," *Nature reviews. Neuroscience*, vol. 8, no. 8, pp. 610–22, Jul. 2007.

[93] S. Goel, D.G. Duda and L. Xu, "Normalization of the Vasculature for treatment of cancer and other diseases," *Physiological Reviews*, vol. 91, no. 3, pp. 1071–1121, Jul. 2011.

[94] J. Folkman, "Tumor angiogenesis: Therapeutic implications," *The New England Journal of Medicine*, vol. 285, no. 21, pp. 1182–6, Nov. 1971.

[95] T. Würdinger and B. A. Tannous, "Glioma angiogenesis," *Cell Adhesion & Migration*, vol. 3, no. 2, pp.230-35, Jun. 2009.

[96] N. Pannetier, M. Sohlin, T. Christen, L. Schad and N. Schuff, D Revel, R.C. Brasch, H. Paajanen, W. Rosenau, W. Grodd, B. Engelstad, P. Fox and J. Winkelhake,"Gd-DTPA contrast enhancement and tissue differentiation in MR imaging of experimental breast carcinoma," *Radiology*, vol. 158, no. 2, pp. 319–23, Feb. 1986.

[97] D. Revel, R.C. Brasch, H. Paajanen, W. Rosenau, W. Grodd, B Engelstad, P. Fox and J. Winkelhake, "Gd-DTPA contrast enhancement and tissue differentiation in MR imaging of experimental breast carcinoma," *Radiology*, vol. 158, no. 2, pp. 319–23, Feb. 1986.

[98] V.M. Runge, J.A. Clanton, A.C. Price, C.J Wehr, W.A. Herzer, C.L Partain and A.E. Jr. James, "The use of Gd DTPA as a perfusion agent and marker of blood-brain barrier disruption," *Magnetic Resonance Imaging*, vol. 3, no. 1, pp. 43–55, Jan. 1985.

[99] A. Jackson, D.L Buckley and G.J.M. Parker, "Dynamic contrast-enhanced magnetic resonance imaging in oncology," *Springer-Verlag Berlin Heidelberg*, pp.53-67, 2005.

[100] V.Y.U. Kuperman, G.S. Karczmar, M.J. K. Blomley, M. Z. Lewis, L.M. Lubich and M.J. Lipton, "Differentiating between T1 and T2* changes caused by gadopentetate dimeglumine in the kidney by using a double-echo dynamic MR imaging sequence," *Journal of Magnetic Resonance Imaging*, vol. 6, no. 5, pp. 764–768, Sep. 1996.

[101] H. Uematsu, H. Yamada and T. Matsuda, "Measurement of cerebral perfusion with dual-echo multi-slice quantitative dynamic susceptibility contrast MR," *Journal of Magnetic Resonance Imaging*, vol. 10, no. 2, pp. 109–117, Aug. 1999.

[102] H. Schmiedeskamp, M. Straka, R.D Newbould, G. Zaharchuk, J.B. Andre, J.M. Olivot, M.E. Moseley, G.W. Albers and R. Bammer, "Combined spin-and gradient-echo perfusion-weighted imaging," *Magnetic Resonance in Medicine*, vol. 68, no. 1, pp.30-40 Nov. 2011.

[103] J. T. Skinner, R. K. Robison, C. P. Elder, A. T. Newton, B. M. Damon and C. C. Quarles, "Evaluation of a multiple spin- and gradient-echo (SAGE) EPI acquisition with SENSE acceleration: Applications for perfusion imaging in and outside the brain," *Magnetic Resonance in Medicine*, vol. 32, no. 10, pp.1171-80, Aug. 2014.

[104] M. Rempfler, M. Schneider, G.D. Ielacqua, X. Xiao, S.R. Stock, J. Klohs, G. Székely, B.Andres and B.H. Menze, "Reconstructing cerebrovascular networks under local physiological constraints by integer programming," *Medical Image Analysis*, vol. 25, no. 1, pp. 86–94, May 2015.

[105] BBC, "Arteries," in *BBC*, 2016. [Online]. Available: http://www.bbc.co.uk/education/guides/zhnk7ty/revision/3. Accessed: Sep. 26, 2016.

[106] M. A. Jacobs, R. Ouwerkerk, K. Petrowski and K. J. Macura, "Diffusion weighted imaging with ADC mapping and spectroscopy in prostate cancer," *Journal of Magnetic Resonance Imaging*, vol. 19, no. 6, pp. 261–72. Oct. 2010.

[107] S. Valable S, B.L emasson, R. Farion, M. Beaumont, C. Segebarth, C. Remy and E.L. Barbier. "Assessment of blood volume, vessel size and the expression of angiogenic factors in two rat glioma models: a longitudinal in vivo and ex vivo study," *NMR Biomedicine*, vol. 21, no.10, pp. 1043-56, Nov.2008.

[108] K.M. Donahue, H.G. Krouwer, S.D. Rand, A.P. Pathak, C.S. Marszalkowski, S.C. Censky and R.W. Prost,, "Utility of simultaneously acquired gradient-echo and spin-echo cerebral blood volume and morphology maps in brain tumor patients," *Magnetic Resonance in Medicine*, vol. 43, no. 6, pp. 845–53, Jun. 2000.

[109] K.M. Schmainda, S.D Rand, A.M. Joseph, R. Lund, B.D. Ward, A.P. Pathak, J.L. Ulmer, M.A. Badruddoj and H.G. Krouwer, "Characterization of a first-pass gradient-echo spin-echo method to predict brain tumor grade and angiogenesis," *American Journal of Neuroradiology*, vol. 25, no. 9, pp. 1524–32, Oct. 2004.

[110] L. Lamalle, S. Kremer, I. Tropres, S.Grand, C. Rémy, C .Segebarth and J. Le Bas, "VSI and BV MRI of human brain tumours," In *Proceedings of 11 th Annual. Meeting International Society. Magnetic Resonance in Medicine, a1271*, 2003.

[111] Y. Hsu, W. Yang, K. Lim and H. Liu, "Vessel size imaging using dual contrast agent injections," *Journal of Magnetic Resonance in Medicine*, vol. 30, no. 5, pp. 1078–84, Oct. 2009.

[112] V.G Kiselev, R. Strecker, Q. Speck, S. Zyeh, J. Klisch and J. Henning, "Quantitative vessel vize imaging in humans [abstract]" *Proceedings of the 11th Annual. Meeting International Society. Magnetic Resonance in Medicine*, 2003.

[113] T. Breyer, P. Gall, M. Trippel, K. Müller, O. Speck, V. Kiselev and I. Mader, "Clinical evaluation of vessel size imaging in 31 cases of human glial brain tumor [abstract]," *Proceedings of 15th Annual. Meeting International Society. Magnetic Resonance in Medicine*, a836, 2007.

[114] E. Kellner , T. Breyer , P. Gall , K. Müller , M.Trippel , O. Staszewski , F. Stein , O. Saborowski , O. Dyakova ,H. Urbach, V.G. Kiselev, and I.Mader, "MR evaluation of vessel size imaging of human gliomas: Validation by histopathology," *Magnetic Resonance in Medicine*, vol. 42, no. 4, pp. 1117–25, Feb. 2015.

[115] H.Y. Kang , H.L. Xiao, J.H. Chen, Y.Tan ,X.Chen T.Xie, J.Q Fang, S.Wang, Y.Yang and W.G. Zhang "Comparison of the effect of vessel size imaging and cerebral blood volume derived from perfusion MR imaging on Glioma grading," *American Journal of Neuroradiology*. vol. 37, no. 1, pp. 51–7, Sep. 2015.

[116] M. Pectasides, T. Benner, C. J. Wiggins1, C. J. Lopez, H. Ay, F. H. Hochberg, B. R. Rosen and A. G. Sorensen, "Evaluation of vessel size heterogeneity in brain tumors with dynamic contrast-enhanced dual echo perfusion weighted imaging [abstract]. *Proceedings of 16th Annual. Meeting International Society Magnetic Resonance in Medicine*, a152, 2004.

[117] T.T Batchelor, A.G. Sorensen, E.di. Tomaso, W.T .Zhang, D.G. Duda, K.S. Cohen, K.R. Kozak, D.P.Cahill, PJ Chen, M Zhu, M Ancukiewicz, M.M. Mrugala, S. Plotkin, J. Drappatz, D.N. Louis, P. Ivy, D.T. Scadden, T Benner, J.S. Loeffler, P.Y. Wen and R.K. Jain, "AZD2171, a pan-vEGF receptor tyrosine kinase inhibitor, normalizes tumor vasculature and alleviates edema in glioblastoma patients," *Cancer cell*, vol. 11, no. 1, pp. 83–95, Jan. 2007.

[118] A.G. Sorensen, T.T. Batchelor, W.T. Zhang, P.J. Chen, P. Yeo, M.Wang, D. Jennings, P.Y. Wen, J. Lahdenranta, M. Ancukiewicz, E.di. Tomaso, D.G. Duda, and R.K. Jain. "A 'vascular normalization index' as potential mechanistic biomarker to predict survival after a single dose of cediranib in recurrent glioblastoma patients," *Cancer Research*, vol. 69, no. 13, pp. 5296–300, Jun. 2009.

[119] T.T. Batchelor, E.R. Gerstner, K.E. Emblem, D.G. Duda, J Kalpathy-Cramer, M. Snuderl, M.Ancukiewicz, P Polaskova, M.C. Pinho, D. Jennings, S.R. Plotkin, A.S. Chi, A.F. Eichler, J. Dietrich, F.H. Hochberg, C. Lu-Emerson, A.J. Iafrate, S.P. Ivy, B.R. Rosen, J.S. Loeffler, P.Y. Wen, A.G. Sorensen and R.K. Jain, "Improved tumor oxygenation and survival in glioblastoma patients who show increased blood perfusion after cediranib and chemoradiation," *Proceedings of the National Academy of Sciences of the United States of America*, vol. 110, no. 47, pp. 19059–64, Nov. 2013.

[120] S.E. Ungersma, G. Pacheco, C. Ho, S.F. Yee, J. Ross, N. van Bruggen, Jr. FV. Peale, S. Ross and R.A. Carano, "Vessel imaging with viable tumor analysis for quantification of tumor angiogenesis," *Magnetic Resonance in Medicine*, vol. 63, no. 6, pp. 1637–47, Jun. 2010.

[121] S. Valable, B. Lemasson, R. Farion, M. Beaumont, C. Segebarth, C. Remy, E.L. Barbier, "Assessment of blood volume, vessel size and the expression of angiogenic factors in two rat glioma models: A longitudinal in vivo and ex vivo study," *NMR in Biomedicine*, vol. 21, no. 10, pp. 1043–56, Jul. 2008.

[122] L. Ostergaard, P Johannsen, P Høst-Poulsen, P. Vestergaard-Poulsen, H.Asboe, A.D. Gee, S.B. Hansen, G.E. Cold, A Gjedde and C. Gyldensted, "Cerebral blood flow measurements by magnetic resonance imaging bolus tracking: Comparison with [(15)O]H2O positron emission tomography in humans," *Journal of Cerebral Blood Flow and Metabolism*, vol. 18, no. 9, pp. 935–40, Sep. 1998.

[123] N.Sadeghi, I.Salmon, C.Decaestecker, M.Levivier, T.Metens, D.Wikler, V.Denolin, Rorive S, Massager N, Baleriaux D and Goldman S, "Stereotactic comparison among cerebral blood volume, methionine uptake and histopathology in brain glioma," *American Journal of Neuroradiology*, vol. 28, no. 3, pp. 455–61, Mar. 2007.

[124] D.N. Louis, A. Perry, G. Reifenberger, A von Deimling, D. Figarella-Branger W.K.Cavenee, H. Ohgaki. O.D. Wiestler, P. Kleihues and D.W. Ellison, "The 2016 world health organization classification of tumors of the central nervous system: A summary," *Acta neuropathologica*, vol. 131, no. 6, pp. 803–20, May 2016.

[125] M.T. Madsen, "A simplified formulation of the gamma variate function," Physics in Medicine and Biology, vol. 37, no.7, pp. 1597-600, 1992.

[126] V. Patil and G. Johnson, "An improved model for describing the contrast bolus in perfusion MRI," *Medical Physics*, vol. 38, no. 12, pp. 6380–3, Dec. 2011.

[127] S. Smith, "Fast robust automated brain extraction," *Human Brain Mapping*, vol. 17, no. 3, pp. 143–55, Oct. 2002.

[128] M. Jenkinson and S. Smith, "A global optimisation method for robust affine registration of brain images," *Medical Image Analysis*, vol. 5, no. 2, pp. 143–56, Aug. 2001.

[129] M. Jenkinson, P. Bannister, M. Brady and S. Smith, "Improved optimization for the robust and accurate linear registration and motion correction of brain images," *NeuroImage*, vol. 17, no. 2, pp. 825–41, Oct. 2002.

[130] Y. Zhang, M. Brady and S. Smith, "Segmentation of brain MR images through a hidden Markov random field model and the expectation-maximization algorithm," *IEEE Transactions on Medical Imaging*, vol.20, no.1, pp.45-57, 2001.

[131] X. Chao , W.U. H.Schmidt, K.Villringer, P.Brunecker, V. Kiselev, P.Gall and J.B Fiebach,"Vessel size imaging reveals pathological changes of microvessel density and size in acute ischemia," *Journal of Cerebral Blood Flow and Metabolism*, vol. 31, no. 8, pp. 1687–95, Apr. 2011.

[132] D.H. Heiland, T. Demerath, E. Kellner, V.G. Kiselev, D. Pfeifer, O. Schnell, O. Staszewski, H. Urbach, A. Weyerbrock and I. Mader, "Molecular differences between cerebral blood volume and vessel size in glioblastoma multiforme," *Oncotarget*, Sep. 2016.

Annexes

Annexe 1

Table A.1: Patients information. Patient number, sex and histologic information. Regarding the histologic information, all the patients had a positive ^{18}F-FET tumor exame. HGG: High Grade Glioma, LGG: Low Grade Glioma, A: Astrocytoma, OA: Oligoastrocytoma and GBM: Gliobastoma.

PATIENT	SEX	HISTOLOGY
1	M	OA III
2	M	GBM
3	M	OA III
4	M	GBM
5	M	GBM
6	M	GBM
7	M	Glioma (not further specified)
8	F	LGG
9	M	A III
10	M	Glioma (not further specified)
11	F	GBM
12	F	A II (LGG)
13	M	HGG (Suspected)
14	M	OA III
15	M	HGG (Suspected)
16	M	HGG (Suspected)
17	F	Residual HGG
18	M	OA III
19	F	GBM
20	M	HGG
21	M	HGG
22	F	HGG
23	F	Suspected of Metastasis
24	M	HGG (Suspected)
25	F	GBM

Annexe 2

Table A.2: The estimated Vsi in different ROIs (WM, GM and tumor) for each patient. Mean, standard deviation and the respective difference in normal (WM and GM) and tumor tissue in percentage. The mean and the standard deviation was calculated for all the pixels between the 16 slices. The percentage was calculated using the formula $\mathrm{WM,GM}\ (\%) = \left(1 - \frac{\mathrm{WM.GM}}{\mathrm{Tumor}}\right)$ x 100 .

Vsi					
PATIENT	**WM (µm)**	**GM (µm)**	**Tumor (µm)**	**WM (%)**	**GM (%)**
1	14.03 ± 4.60	17.72 ± 11.75	18.08 ± 7.09	22.40	1.99
2	18.12 ± 9.37	18.82 ± 11.51	19.75 ± 12.78	2.44	-3.90
3	12.16 ± 4.94	20.45 ± 15.02	20.60 ± 10.37	40.97	0.73
4	18.44 ± 12.33	18.53 ± 12.80	28.84 ± 12.32	36.06	35.75
5	13.73 ± 5.93	16.60 ± 7.88	18.40 ± 12.33	25.38	9.78
6	13.55 ± 4.36	17.16 ± 11.73	22.36 ± 9.47	39.40	23.26
7	15.53 ± 5.90	21.74 ± 8.12	23.91 ± 10.46	35.05	9.08
8	11.71 ± 6.63	14.42 ± 11.02	14.41 ± 4.23	18.74	-0.07
9	16.24 ± 13.90	20.11 ± 11.38	25.53 ± 19.21	36.39	21.23
10	12.13 ± 4.41	15.21 ± 7.60	19.84 ± 9.23	38.86	23.34
11	13.71 ± 5.94	18.75 ± 9.46	16.87 ± 9.74	18.73	-11.14
12	13.84 ± 4.80	17.16 ± 6.10	22.90 ± 11.39	39.56	25.07
13	11.30 ± 3.08	16.16 ± 12.10	16.66 ±1 1.86	32.17	3.00
14	14.53 ± 6.57	16.90 ± 5.87	14.86 ± 7.09	2.22	-13.73
15	14.85 ± 6.13	15.06 ± 6.40	14.43 ± 4.68	-2.91	-4.37
16	13.21 ± 3.81	17.86 ± 9.51	19.81 ± 10.95	33.32	9.84
17	15.72 ± 7.64	16.52 ± 8.06	19.93 ± 7.91	21.12	17.11
18	13.45 ± 7.33	20.35 ± 12.97	19.86 ± 8.92	32.28	-2.47
19	12.50 ± 6.57	21.64 ± 20.95	14.05 ± 4.76	11.03	-54.02
20	11.79 ± 5.15	12.44 ± 4.62	29.74 ± 10.80	60.36	58.17
21	13.89 ± 5.46	21.32 ± 10.35	21.16 ± 10.21	34.36	-0.76
22	13.31 ± 7.61	14.45 ± 10.44	16.84 ± 9.92	20.96	14.19
23	14.28 ± 8.20	13.02 ± 6.74	17.10 ± 7.07	16.49	23.86
24	14.12 ± 6.38	16.97 ± 9.41	22.32 ± 13.94	36.74	23.97
25	12.73 ± 6.34	17.60 ± 8.62	18.71 ± 9.98	31.96	5.93

Table A.3: The estimated CBV in different ROIS (WM, GM and tumor) for each patient. Mean, standard deviation and the respective difference in normal (WM and GM) and tumor tissue in percentage. The mean and the standard deviation was calculated for all the pixels between the 16 slices. The percentage was calculated using the formula $\mathrm{WM, GM}\ (\%) = \left(1 - \frac{\mathrm{WM.GM}}{\mathrm{Tumor}}\right) \mathrm{x}\ 100$).

CBV					
PATIENT	**WM (mL/100g)**	**GM (mL/100g)**	**Tumor (mL/100g)**	**WM (%)**	**GM (%)**
1	0.010 ± 0.003	0.015 ± 0.005	0.018 ± 0.014	44.44	16.67
2	0.012 ± 0.005	0.014 ± 0.004	0.012 ± 0.009	1.63	-13.82
3	0.018 ± 0.007	0.027 ± 0.011	0.026 ± 0.008	30.77	-3.85
4	0.013 ± 0.007	0.015 ± 0.007	0.019 ± 0.010	31.58	21.05
5	0.013 ± 0.006	0.017 ± 0.008	0.029 ± 0.030	55.17	41.38
6	0.012 ± 0.003	0.014 ± 0.005	0.017 ± 0.007	29.41	17.65
7	0.012 ± 0.005	0.015 ± 0.007	0.018 ± 0.012	33.33	16.67
8	0.013 ± 0.003	0.017 ± 0.004	0.011 ± 0.004	-18.18	-54.55
9	0.016 ± 0.006	0.020 ± 0.006	0.016 ± 0.013	0.00	-25.00
10	0.015 ± 0.067	0.020 ± 0.010	0.013 ± 0.005	-15.38	-53.85
11	0.013 ± 0.005	0.021 ± 0.008	0.012 ± 0.009	-8.33	-75.00
12	0.011 ± 0.004	0.015 ±0.010	0.027 ± 0.017	65.93	44.44
13	0.009 ± 0.002	0.010 ± 0.002	0.015 ± 0.010	42.00	33.33
14	0.009 ±0.004	0.012 ± 0.002	0.019 ± 0.007	53.68	36.84
15	0.016 ± 0.007	0.018 ± 0.006	0.011 ± 0.006	-45.45	-63.64
16	0.012 ± 0.004	0.017 ± 0.004	0.025 ± 0.025	52.00	32.00
17	0.010 ± 0.004	0.014 ± 0.003	0.011 ± 0.004	16.67	-16.67
18	0.016 ± 0.010	0.020 ± 0.010	0.035 ± 0.021	54.29	42.86
19	0.012 ± 0.004	0.017 ± 0.005	0.014 ± 0.004	14.29	-21.43
20	0.010 ± 0.003	0.013 ± 0.001	0.019 ± 0.007	47.89	31.58
21	0.017 ± 0.005	0.022 ± 0.050	0.023 ±0.007	26.09	4.35
22	0.015 ± 0.006	0.017 ± 0.005	0.022 ± 0.011	31.82	22.73
23	0.019 ± 0.006	0.021 ± 0.005	0.028 ± 0.026	32.14	25.00
24	0.011 ± 0.004	0.014 ± 0.004	0.009 ± 0.007	-22.22	-55.56
25	0.014 ± 0.007	0.016 ± 0.006	0.023 ± 0.014	39.13	30.43

Table A.4: The estimated Q in different ROIs (WM, GM and tumor) for each patient. Mean, standard deviation and the respective difference in normal (WM and GM) and tumor tissue in percentage. The mean and the standard deviation was calculated for all the pixels between the 16 slices. The percentage was calculated using the formula $\mathrm{WM,GM}\ (\%) = -\left(\left(1 - \frac{\mathrm{WM.GM}}{\mathrm{Tumor}}\right) \mathrm{x}\ 100\right)$.

Q					
PATIENT	**WM ($s^{-1/3}$)**	**GM ($s^{-1/3}$)**	**Tumor ($s^{-1/3}$)**	**WM (%)**	**(GM (%)**
1	0.44 ± 0.07	0.52 ± 0.18	0.50 ± 0.11	12.00	-4.00
2	0.45 ± 0.06	0.46 ± 0.06	0.58 ± 0.29	22.41	20.69
3	0.46 ± 0.07	0.47 ± 0.11	0.44 ± 0.09	-9.09	-11.36
4	0.45 ± 0.08	0.46 ± 0.08	0.46 ± 0.14	2.17	0.00
5	0.48 ± 0.07	0.50 ± 0.09	0.59 ± 0.24	18.64	15.25
6	0.42 ± 0.06	0.50 ± 0.09	0.46 ± 0.07	-8.70	-10.87
7	0.45 ± 0.06	0.44 ± 0.07	0.45 ± 0.10	0.00	4.35
8	0.49 ± 0.10	0.53 ± 0.10	0.36 ± 0.04	-36.11	-47.22
9	0.48 ± 0.08	0.49 ± 0.09	0.56 ± 0.26	14.29	12.50
10	0.48 ± 0.08	0.49 ± 0.09	0.46 ± 0.08	-4.35	-6.52
11	0.47 ± 0.09	0.51 ± 0.07	0.45 ± 0.08	-4.44	-13.33
12	0.51 ± 0.05	0.49 ± 0.08	0.46 ± 0.08	-10.87	-6.52
13	0.50 ± 0.07	0.53 ± 0.10	0.58 ± 0.23	13.79	8.62
14	0.46 ± 0.09	0.50 ± 0.07	0.56 ± 0.11	17.86	10.71
15	0.51 ± 0.10	0.52 ± 0.09	0.46 ± 0.08	-10.87	-13.04
16	0.49 ± 0.08	0.53 ± 0.07	0.56 ± 0.05	12.50	5.36
17	0.44 ± 0.06	0.47 ± 0.07	0.45 ± 0.10	-4.44	-8.89
18	0.50 ± 0.13	0.49 ± 0.13	0.54 ± 0.17	7.41	9.26
19	0.46 ± 0.09	0.48 ± 0.10	0.50 ± 0.05	8.00	4.00
20	0.50 ± 0.07	0.53 ± 0.06	0.40 ± 0.09	-25.00	-32.50
21	0.47 ± 0.05	0.46 ± 0.08	0.42 ± 0.06	-11.90	-9.52
22	0.47 ± 0.09	0.53 ± 0.10	0.53 ± 0.11	11.32	0.00
23	0.47 ± 0.07	0.44 ± 0.07	0.46 ± 0.09	-4.35	4.35
24	0.48 ± 0.06	0.49 ± 0.07	0.42 ± 0.19	-14.29	-16.67
25	0.51 ± 0.12	0.44 ± 0.08	0.70 ± 0.64	27.35	37.32

Table A.5: Distance values between the hot spots of ^{18}F-FET data with Vsi, CBV and Q. The distance was calculated based on equation 4.10.

DISTANCE (Voxel)			
PATIENT	**Vsi**	**CBV**	**Q**
1	2.45	2.45	4.12
2	55.16	12.53	4.47
3	3.74	3.16	76.16
4	29.15	5.10	50.52
5	70.00	12.37	9.70
6	4.00	4.00	71.60
7	7.14	7.07	80.42
8	7.87	5.92	60.88
9	32.62	5.00	7.8740
10	12.88	8.66	82.60
11	7.87	10.30	4.24
12	2.83	2.83	64.54
13	35.07	21.84	14.07
14	7.55	1.73	79.86
15	5.10	9.17	61.28
16	4.00	4.00	88.96
17	31.80	8.66	59.10
18	17.23	18.87	60.94
19	3.61	4.58	3.74
20	2.24	2.24	85.77
21	4.12	2.24	76.84
22	15.59	9.055	86.32
23	5.48	2.45	86.09
24	17.35	19.00	68.74
25	2.00	2.45	69.66